The Dissertation Committee for Camila A. Saez Cabezas certifies that this is the approved version of the following Dissertation:

Design and Assembly of Metal Oxide Nanocrystal Gels via Depletion Attractions

Committee:

Delia J. Milliron, Supervisor

Thomas M. Truskett, Co-Supervisor

Nathaniel A. Lynd

Simon M. Humphrey

Design and Assembly of Metal Oxide Nanocrystal Gels via Depletion Attractions

by

Camila A. Saez Cabezas

Dissertation

Presented to the Faculty of the Graduate School of

The University of Texas at Austin

in Partial Fulfillment

of the Requirements

for the Degree of

Doctor of Philosophy

The University of Texas at Austin

May 2020

Acknowledgements

I must admit that I have always loved reading the acknowledgements section of a Dissertation. Sometimes I am so eager to read it that I even skip the abstract. As I contemplated what I would write in my acknowledgements, I felt that mine would not be complete unless I explained why I find them so special, so please bear with me briefly. The acknowledgements section is the only space where the Ph.D. student can narrate, reflect on, and pay homage to the journey. My journey has involved so many incremental moments of resilience, navigating uncertainty, creativity, patience, adaptability, mistakes, embracing fear, redefining success, and derisking failure, to name a few. These moments have shaped me deeply, guided me towards a version of myself that I am proud of, and helped make sense of the puzzle pieces that would become the findings in this dissertation. I cannot image how any of it would have been possible without the encouragement, support, and friendship of the people I have encountered on this path. In truth, acknowledgements are the pages I read to remind myself of one of the reasons why I love research: it is fueled by, fueled alongside, and fueled for human beings. These are the people who have propelled me towards this milestone.

First, I would like to thank my two advisors Delia and Tom. Delia, infinite thanks for everything you invested in me, your mentorship, your encouraging words during challenging times, your rigorous and constructive feedback, and the research and leadership opportunities. I have been exposed to even more incredible science, grown so much more, and become a much better scientist than I could have ever imagined while working with you. Thank you for believing in my potential even when I was filled with self-doubt, imposter syndrome, and risk aversion. I will always admire of your ability to spot an innovative opportunity (whether it's about a person, a team, a start-up, an area of research, etc), your scientific curiosity, your tenacity for excellence, your passion for your research, and your collaborative and interdisciplinary talents. In addition, thank you for recruiting the most incredible people to the group. Because of this, I have had the privilege

to learn from insanely talented individuals and I have forged very meaningful friendships. Likewise, thank you for hosting Christmas parties and other gatherings at your house and inviting significant others to come along too, so we could share meals and moments that helped forge the culture of the group and a sentiment of extended family. Finally, thank you so much for challenging me beyond my comfort zone, pushing me to achieve more and to reach a higher quality than I thought I would be capable of, trusting me as I carved my path towards the finish line, and for providing a space to make mistakes, fail, get back up, embrace the fear, and try again. These lessons have been invaluable, and I will carry them with me for the rest of my career. Tom, thank you for coming on board as my co-advisor. My number one regret is that I didn't ask you sooner. Thank you for being so enthusiastic about my work and our collaboration, keeping my best interest at heart, listening attentively and looking to help whether I was doing well, I was navigating uncertainty, or I was confused about my data, helping me find blind spots in my experiments and analysis, and the encouraging words when I was overwhelmed. One of my favorite memories of my Ph.D. is about the day that you asked me (again) patiently if I had examined the structure factor of my assemblies because after our meeting I performed the analysis and I was finally able to interpret my data and strengthen the wobbly parts of my ITO gel story. In addition, I am extremely grateful for the postdocs you have recruited and for your guidance and support as we figured out the magic ingredients of our collaboration. Lastly, thank you for the culture and environment you have shaped as Department Chair. As a graduate student of the McKetta Department of Chemical Engineering, I have felt welcomed and respected, which I view as a reflection of your leadership.

To the postdocs I had the pleasure to work with, thank you for the hands-on training and the advice. Gabriel, thank you for taking me under your wing my first year. You were so instrumental in helping me get started in the lab and learn how to design my first experiments. Yang, thank you for sharing your tips and tricks from deciphering Anna's POM-ITO functionalization methods and for helping me perform my first ligand stripping procedure; I will never forget it. Also, thank you for helping create a fun work environment

from the basketball pickup game with the Korgelites, making us mapo tofu, the lunch time conversations, and the encouraging words after my group meeting presentations (it meant a lot). Amita and Ajay, thank you for teaching me how to use and maintain a Schlenk line as well as general nanocrystal synthesis tips and tricks; I couldn't have asked for better first fumehood neighbors. Byung Hyo, thank you for being such a kind desk neighbor and for always being interested and willing to talk about my science; I remember our conversations fondly. Jongwook, thank you for showing me how to setup my first SEC experiment, teaching me how to template nanocrystals and helping find an interesting direction for the electrodeposition project, and reminiscing about French culture with me. Omid, thank you for helping me with electrochemistry and for elevating the soccer talent in the group. Molly, thank you for sharing your personal and professional journey, for listening to me, for the considerate advice, and for trusting me to return the favor; I can't wait for our new adventure in Midland, MI. Beth and Ryan, thank you for collaborating with me, introducing me to depletion attractions and stat mech, helping me decipher your theory lingo, the proposal support, attending my practice talks, and the feedback. Your guidance and input were so valuable throughout my Ph.D. and I truly appreciated it. Mike, I am so incredibly grateful that you joined the Truskett during a pivotal transition time. Thank you for being an ally during meetings, listening to me, giving me advice, letting me vent although you had enough on your plate, empathizing with the experimental setbacks, brainstorming with me and helping me find a direction towards the end of my Ph.D., and the good laughs. Zach, I sincerely hope you've enjoyed our collaboration because I truly have. Thank you for always being willing to listen to my problems, for understanding what I was going through trying to figure out the logistics of graduation because not long ago you were in the same position, for contributing to my nanocrystal gel work (and helping me stay sane as I chased my vision), for the brainstorming sessions, and for the constructive edits on my paper when my brain was too tired. Anthony, mon cher ami et collaborateur transatlantique, who would have thought when you first arrived at UT that we would end writing a paper and traveling the world together and sharing tellement de bon moments? Thank you for your unconditional support, cheering me on and up when I needed it the most, powering

through my edits and rewrites, and your refreshing enthusiasm for science. J'apprécie énormément ton amitié et j'ai hâte de partager des nouvelles aventures.

To my fellow Ph.D. students, thank you for your friendship, the laughs, the advice, the support, and sharing your knowledge with me. Evan, thank you for believing in my potential, for recruiting me to the Milliron group, for your kind and thoughtful mentorship, for encouraging me during the daunting early months in lab, for everything you taught me (plasmonics, ITO synthesis, colloid preparation tricks, good lab practices, and more), and for introducing me to good food. Amy, thank you for including me in the fun and memorable group outings you organized, for being Tim's midwestern ally (otherwise he would have never felt comfortable hanging out with us), for being a good role model, and for inspiring me to find balance in graduate school. Clay, thank you for your all-around bright and joyful spirit (it was so contagious and I miss it every day), your thought-provoking questions, your helpful feedback, for eating my culinary experiments, and for being an excellent companion for our Austin adventures. Rob, thank you for teaching me spectroscopy and the art of troubleshooting and for challenging me to critically evaluate my scientific work. Gary, words cannot express how grateful I am for everything you contributed to my Ph.D.: from the scientific and laboratory training to teaching me valuable life lessons and catalyzing my personal growth. Working with you has been one of the highlights of this journey. Thank you for listening, the delicious and memorable meals, the tea times, and your friendship. Ankit, thank you for sharing your wisdom with me, the jokes when I was stressed out, the Indian food, and helping me make sense of gel optical properties. Corey, thank you for sharing tips and tricks throughout our early and messy syntheses, your honesty, exchanging ideas and constructive feedback, and helping me navigate my path towards the finish line. Sungyeon, thank you for being our glovebox hero, undertaking so many lab responsibilities, your kind words of encouragement, and all the effort you devoted towards helping me complete and troubleshoot the electrochemical deposition project (I couldn't have done it without you and it meant a lot). Lauren, my kindred spirit, I am so incredibly fortunate to have shared my Ph.D. journey with such a smart, hardworking, kind, reliable, resilient, and impressive lady. Thank you for your

friendship, the meaningful and introspective conversations, the tea times, the unconditional support, encouraging me to advocate for myself, helping me keep the guys in line, sharing lab management responsibilities with me and stepping up to take over when I was overextended, providing key and valuable feedback on my presentations and papers, for the fun dates, and so much more. I hope we'll stay in each other's lives for a long long time. Shin, thank you for being the best fumehood partner (and desk neighbor over the last year), the late-night company, the FITO cubes, and the heartfelt karaoke performances. Stephen, thank you for hanging out with me in the office in the early AM (I especially enjoyed our Monday morning check-ins), helping me train for the Longhorn Runs (I would have given up without your coaching and enthusiasm), becoming a considerate, valuable, and wise leader and mentor in the group, collaborating on the ITO-Shew project and co-mentoring Yongdan with me (it's been a blast), the dance parties, the concerts, and your friendship. It's been a pleasure watching you mature into a role model and accomplished scientist and I'm sure you will succeed regardless of the career path you choose. Manny, thank you for contributing your chemistry talents to the assembly team (we really needed it), the baked goods, coming on board the niobium oxide characterization train, the slow-grown ITO, and the support as we navigated MRSEC duties. Bharat (when we first met, you were a fellow Ph.D. student, so you belong in this category), thank you for your beaming personality, the enthusiastic high fives, the crazy lunch time stories, and caring about my sanity and well-being. You've been an explosive (in a good way) and valuable addition to the group. Allison, thank you for coming on board and being excited about continuing the depletion gel work, helping me finish experiments during my last year, your work ethic, joining the ballet class and driving me there, the movie nights, and your company (it has made this transition process more joyful and less lonely).

To my undergraduate researchers Kristen, Kendall, and Yongdan, thank you for investing considerable effort, interest, and time during your college career to help me with my projects.

Finally, to the close friends and family who played an essential supportive role throughout my journey, thank you from the bottom of my heart. Jen, thank you for being

my unconditional domestic partner and friend. Moving to Texas with you made the transition process smoother, less lonely, and less scary. Despite the challenges and dark times of our parallel graduate school journeys, I remember our adventures, dates, celebrations, and even grocery store trips fondly. Mat, thank you for welcoming me as the third roommate, providing comforting advice and perspective, checking up on me when Tim was out of town, celebrating my birthdays with me, being my personal bartender, and bolstering my mental sanity. To my siblings Vicente and Daniela, gracias por visitarme durante sus vacaciones de Navidad, apoyarme a la distancia, las llamadas por FaceTime, darme ánimo, recordarme que los momentos difíciles saben menos amargo gracias al cariño de ustedes, y por decirme lo orgullosos que están de mi porque siempre me ha dado fuerzas. Los quiero mucho. To my parents Sebastián and Mabel, gracias por todo lo que han invertido y sacrificado para que yo pudiese acceder a las oportunidades que me han abierto camino, enseñarme a soñar en grande y a valerme por misma, recordarme que aunque la vida te de fuertes palizas puedo llegar lejos enfrentándola con mi sonrisa, creatividad, y resiliencia, el apoyo incondicional, venir a verme cuando más lo necesitaba, aconsejarme y consolarme por FaceTime, el regaloneo, y los abrazos. Los adoro. To Tim, thank you for being a loving and supportive partner and for believing that our relationship was worth balancing and nurturing along with both our Ph.Ds. Falling in love with you so early in the process was a beautiful gift that felt so natural, despite not being part of the plan, and brought me so much happiness. Thank you for loving me exactly as I am, telling me that everything was going to be ok even though I didn't think so at the time and it was the last thing I wanted to hear, eating your way through Austin with me, expanding your food palate so we could go on dreamy culinary adventures, joining me for a day of ACL every year, visiting Chile with me, taking me to the beach multiple times, the "real" yoga classes at a "professional" studio that eventually got me into Singer's VIP yogi list, trusting me with your car keys, cheering me on and celebrating my successes even when you were struggling and frustrated with your own research, the warmest of hugs, and so much more. I can't wait for the next chapter of our lives together.

Abstract

Design and Assembly of Metal Oxide Nanocrystal Gels via Depletion Attractions

Camila A. Saez Cabezas, Ph.D.

The University of Texas at Austin, 2020

Supervisors: Delia J. Milliron and Thomas M. Truskett

Achieving and implementing macroscopic materials capable of displaying the unique properties inherent to inorganic nanocrystals requires bridging the nanoscale and the length scales of larger orders of magnitude in a systematic, controllable, and scalable way. Over the last 15 years, nanocrystal gels have been developed and investigated as potential materials to tackle this need. However, available gelation methods rely on chemical reactions and interactions specific to the stabilizing molecules on the nanocrystal surface, and are therefore not readily adaptable across broad types of materials. Specifically, most studies have focused on gelation methods for metal chalcogenides and noble metals, whereas progress on metal oxide nanocrystal gels has lagged behind.

This dissertation investigates and demonstrates an alternative gelation method based on entropic depletion attractions that are not dependent on specific surface chemistries and have not been explored in nanoscale colloidal gels. In the first study, a proof of concept system is developed, where depletion attractions induce the gelation of tin-doped indium oxide nanocrystals in the presence of a polymer depletant and achieve a macroscopic material with optical properties reflective of both the microstructure and the

nanostructured building blocks. The mechanism of gelation is assessed by comparing the observed phase behavior to theoretical predictions and the microstructure is characterized by small-angle X-ray scattering (SAXS). Next, the universal applicability of depletion attractions is demonstrated by varying the composition and shape of the building blocks while fixing size and nanocrystal volume fraction. The gelation of spherical nanocrystals occurs at the same depletant concentration and this phase transition threshold does not depend on the specific composition of the metal oxide nanocrystal. Consistent with theoretical phase boundary calculations, cubic nanocrystals form gels at a lower depletant concentration than spherical nanocrystals due to the ability to pack face-to-face and therefore increase the overlap excluded volume during assembly. Finally, a method to polymer-wrap tin-doped indium oxide nanocrystals in a controllable way while maintaining colloidal stability is investigated in an effort to tune the physicochemical properties of the metal oxide building blocks available for gelation.

Table of Contents

List of Tables xv

List of Figures xvi

Chapter 1: Introduction 1

Technological Motivation 1

Self-Assembly 2

Colloidal Stability 3

Depletion Attractions 6

Colloidal Gels 8

Dissertation Overview 11

Chapter 2: Gelation of Plasmonic Metal Oxide Nanocrystals by Polymer-Induced Depletion-Attractions 15

Introduction 15

Experimental methods 19

ITO Nanocrystal Synthesis and Ligand Stripping 19

ITO-PEG Assemblies 20

Electron Microscopy 20

Small-angle X-ray Scattering Measurements and Analysis 21

X-ray Diffraction 21

Spectroscopy 22

Results and Discussion 23

Conclusions and Outlook 38

Chapter 3: Universal Gelation of Metal Oxide Nanocrystals via Depletion Attractions 41

Introduction 41

Experimental Methods 44
Synthesis of Iron Oxide (FeO_x) Nanocrystals 44
Synthesis of Tin-Doped Indium Oxide ($Sn:In_2O_3$) Nanocrystals 44
Synthesis of Fluorine, Tin-Codoped Indium Oxide ($F,Sn:In_2O_3$) Nanocrystals 45
Ligand Stripping of FeO_x Nanocrystals 45
Ligand Stripping of $Sn:In_2O_3$ Nanocrystals 46
Ligand Stripping of $F,Sn:In_2O_3$ Nanocrystals 47
Nanocrystal Gel Assembly 47
Small-angle X-ray Scattering 48
Electron Microscopy 49
Fourier Transform Infrared Spectroscopy 49
Zeta Potential 49
Results and Discussion 50
Conclusions and Outlook 59
Chapter 4: Aqueous Processing and Spray Deposition of Polymer-Wrapped Tin-Doped Indium Oxide Nanocrystals as Electrochromic Thin Films 61
Introduction 61
Experimental Methods 64
ITO Nanocrystal Synthesis and Ligand Stripping 64
Polymer Wrapping Procedure 65
Spray Coating 66
Electron Microscopy 66
Fourier-transform Infrared Spectroscopy 66

Dynamic Light Scattering and Zeta Potential 67
Thermogravimetric Analysis 67
Electrochemical Modulation 67
Results and Discussion 68
Conclusions and Outlook 80
Chapter 5: Future Directions for Depletion-Induced Nanocrystal Gelation 82
Appendices 86
Appendix 1: Supporting Information for Chapter 2 86
Experimental Supporting Figures 86
Theoretical Model for Bridging and Depletion Gelation 92
LSPR Simulation and COMSOL Methods 95
Appendix 2: Supporting Information for Chapter 3 98
Experimental Supporting Figures 98
Theoretical Methods 103
Appendix 3: Supporting Information for Chapter 4 105
Experimental Supporting Figures 105
References 110

List of Tables

Table 2.1: Summary of SAXS unified fit results. 29

Table 2.2: Summary of Scherrer analysis results for the four most intense In_2O_3 diffraction peaks. 32

Table 3.1. Summary of different quantities used to prepare nanocrystal-PEG mixtures 48

Table 4.1: Influence of PAA-$mPEO_4$ wrapping conditions on colloidal stability of ITO dispersions and electrochromic modulation of composite films. ... 79

Table A1.1: Extracted unified fit parameters from PEG sizing by small-angle X-ray scattering. 88

Table A1.2: Summary of nanocrystal volume fractions measured by inductively coupled plasma-atomic emission spectroscopy. 89

Table A1.3: Dielectric parameter for ITO. 96

Table A3.1: Summary of roughness measurements by profilometry and atomic force microscopy. 108

List of Figures

Figure 1.1: Representative plots of pair interaction potentials. 4

Figure 1.2: Effect of solvent environment and particle surface chemistry on electrostatic repulsion potential. 6

Figure 1.3: Schematic of two spherical colloids experiencing depletion attractions. 8

Figure 1.4: Schematic phase diagram for colloids dispersed in solution interacting by short-range attractions. 9

Figure 2.1: Surface chemistry of as-synthesized and ligand-stripped ITO. 23

Figure 2.2: SAXS scattering intensity and form factor fitting. 25

Figure 2.3: SAXS characterization of the ITO-PEG flowing dispersions and gels. .. 26

Figure 2.4: Identification of Porod regimes by derivative analysis. 28

Figure 2.5: Unified fitting of ITO-PEG gels S(q). 29

Figure 2.6: Transmission electron microscopy images of freeze-dried and diluted ITO-PEG gel ([PEG]= 534 mM). 31

Figure 2.7: X-ray diffraction patterns of nanocrystals and gel. 32

Figure 2.8: Comparison of theoretical model to experimental observations. 35

Figure 2.9: Experimental and simulated optical properties of ITO-PEG gels. 36

Figure 3.1: Morphology, size, and colloidal stability of nanocrystals. 51

Figure 3.2: FTIR of nanocrystal before and after ligand-stripping. 52

Figure 3.3: Zeta potential of ligand-stripped nanocrystal dispersions. 52

Figure 3.4: Structure factor of depletion gels. 53

Figure 3.5: Identification of Porod regions by derivative analysis. 55

Figure 3.6: Power law fits of Porod region. 55

Figure 3.7: Comparison of predicted phase behavior and experiments. 57

Figure 3.8: Theoretical spinodal boundary (line) and experimental observations (points) for FeO_x nanocrystal spheres. 58

Figure 3.9: Evolution of structure factor S(q) of $Sn:In_2O_3$ nanocrystal-PEG mixtures over 4 weeks. 59

Figure 4.1: TEM of ITO aqueous dispersions after PAA-$mPEO_4$ wrapping. 69

Figure 4.2: TEM images comparing the morphology of ITO nanocrystals before and after ligand removal. 69

Figure 4.3: Colloidal stability of ITO aqueous dispersions after PAA-mPEO4 wrapping in exchange solutions of different pH. 71

Figure 4.4: PAA-$mPEO_4$ adsorption on ITO is influenced by the pH of the exchange solution. 73

Figure 4.5: PAA-$mPEO_4$ adsorption on the ITO surface is inhibited by raising the pH of a potassium hydroxide exchange solution. 74

Figure 4.6: SEM of ITO films spray coated onto silicon substrates from aqueous dispersion after PAA-$mPEO_4$ wrapping. 75

Figure 4.7: Electrochromic modulation of ITO films spray coated onto FTO glass from ITO aqueous dispersion after PAA-$mPEO_4$ wrapping. 77

Figure 4.8: Electrochromic modulation of ITO films spray coated onto FTO glass from ITO aqueous dispersion after PAA-$mPEO_4$wrapping in potassium hydroxide exchange solution. 78

Figure 4.9: Coloration efficiency curves. 79

Figure 5.1: Evolution of the elastic and loss modulus of a tin-doped indium oxide nanocrystal depletion gel over time at a fixed frequency (5 rad/s). 84

Figure 5.2: Evolution of the elastic and loss modulus of a tin-doped indium oxide nanocrystal bridging gel over time at a fixed frequency (5 rad/s). 85

Figure A1.1: Sizing of as-synthesized tin-doped indium oxide (ITO) nanocrystals. 86
Figure A1.2: Colloidal stability of ligand-stripped nanocrystals in polar solvents. 87
Figure A1.3: Comparison of the solubility of polyethylene glycol (PEG, M_n= 1100 g/mol) in acetonitrile (left vial) and dimethylformamide (right vial) at a concentration of 664 mg/mL. 87
Figure A1.4: PEG (M_n= 1100 g/mol) in acetonitrile sizing by small angle X-ray scattering. 88
Figure A1.5: Small-angle X-ray scattering analysis of ITO-PEG dispersion with [PEG]= 271 mg/mL. 90
Figure A1.6: Full range of the structure factor S(q) of the ITO-PEG dispersion with [PEG]= 8.00 mM. 90
Figure A1.7: Isoelectric point measurement of ligand-stripped ITO nanocrystals. 91
Figure A1.8: Zeta Potential of ITO-PEG dispersions. 92
Figure A1.9: Simulated Structure Geometry. 96
Figure A1.10: Meshing. 97
Figure A2.1: Photograph of PEG solution in acetonitrile. 98
Figure A2.2: Structure factor S(q) deconvolution. 98
Figure A2.3: Theoretical spinodal boundaries for spherical Sn:In_2O_3 and cubic F,Sn:In_2O_3 nanocrystals. 99
Figure A2.4: Evolution of structure factor S(q) of FeOx nanocrystal-PEG mixtures over 4 weeks. 100
Figure A2.5: Evolution of structure factor S(q) of FeO_x nanocrystal-PEG and Sn:In_2O_3 nanocrystal-PEG mixtures between 4 and 8 weeks. 101

Figure A2.6: Evolution of structure factor S(q) of F,Sn:In_2O_3 nanocrystal-PEG mixtures over 3 weeks. 102
Figure A3.1: Comparison of ligand-capped (LC) and ligand-stripped (LS) ITO dispersions. 105
Figure A3.2: FTIR reference for PAA-mPEO_4 and sodium tetrafluoroborate. 106
Figure A3.3: ITO dispersion after exposure to ligand exchange at pH= 9.1 containing borate only (no PAA-mPEO_4). 107
Figure A3.4: Evolution of differential optical density (ΔOD) and inserted charge density (ΔQ) as a function of time for PAA-mPEO_4-wrapped ITO films. 108
Figure A3.5: Cyclic voltammetry for PAA-mPEO_4-wrapped ITO films. 109

Chapter 1: Introduction

TECHNOLOGICAL MOTIVATION

Over the last few decades, advances in colloidal synthesis methods and ligand chemistries have produced a diverse library of complex inorganic nanoparticle dispersions with tunable emergent properties.[1-4] Yet, without structure, the ability to create new functional materials and engineer their performance using nanoscale building blocks is significantly restricted. Fundamentally, integrating nanotechnology into bulk materials, devices, and application components requires compatibility with scalable manufacturing and the development of assembly methods to bridge the different relevant length scales.[5-7] Strategies to fabricate multiscale structures rely on combining assembly techniques of complementary length scales: top-down patterning spanning the μm-cm length scale (e.g., lithography, surface patterning, layer-by-layer, and 3D printing) and solution-based bottom-up assemblies spanning the nm-μm length scale (e.g., self-assembly and microfluidics).[8,9] In particular, precise control over the material microstructure at the individual nanoparticle level is key to design and tune functionality because nanoscale properties are responsive to the spatial arrangement, orientation, and surface chemistry of neighboring nanoparticles. In fact, the dependence of collective properties on the local structure of nanoparticles has been demonstrated for different optoelectronic applications such as localized surface plasmon resonance,[10-12] photoluminescence,[13-15] photocatalysis, and charge transport[16-19] to name a few.

Although the development and characterization of assembly methods have progressed significantly and have been positioned at the forefront of nanomaterials research,[6,20] the fabrication of macroscopic materials using nanoparticles remains challenging. Specifically, achieving free standing, uniform (e.g., defect-free, crack-free, no signs of delamination), optical quality, and mechanically robust bulk materials is difficult.[7,9] The direct assembly of nanoparticles into self-supported gels has circumvented some of these limitations since this approach can produce open and low-density

macroscopic objects, from a colloidal dispersion in a single self-assembly step, able to retain the nanostructure of the individual building blocks, and therefore preserve properties unique to the nanoscale.[21-23] Notably, these characteristics have motivated the design of different gelation methods applicable to broad classes of inorganic nanomaterials (noble metals, metal chalcogenides, and metal oxides). Because these inorganic materials emerged relatively recently, compared to other self-assembly approaches[6] and colloidal gels of soft materials,[24,25] gelation principles for inorganic nanoparticles and their influence on structure and thereby properties remain to be established and explored. In particular, accessing control over the microstructure and long-range order of the assembly relies on tuning interparticle interactions, which are in turn encoded by the thermodynamics and kinetics of the system.[5,23] Likewise, these parameters are intrinsically linked to the physicochemical interactions between nanoparticles and are therefore also dependent on specific surface chemistries.

Ultimately, the significance and impact of self-assembly research efforts, especially for emerging assemblies such as nanocrystal gelation, are centered around harnessing the power to discover and implement new technologies and material solutions. To this end, Glotzer, Solomon, and Kotov discussed in a perspective article that the following questions need to be answered: "How can we organize nanoparticles and colloids into more complex structures? What kind of structures do we need, and why? What new properties characterize these structures?"[5] Considering the depth and breadth of these endeavors, nanocrystal gels offer a particularly interesting framework for experimental and theoretical collaborations.

SELF-ASSEMBLY

Self-assembly is a multidisciplinary and ubiquitous nanoscale process that reflects physical and chemical interactions between colloids in solution. It is an elegant, yet conceptually simple, mechanism responsible for connecting, shaping, and elevating nanomaterials. Although the term "self" implies a lack of external human intervention,

fundamental studies and mastery of self-assembly, especially in experiments, unlocks an exceptional tool to engineer and innovate in the field of nanotechnology.

Broadly, self-assembly is the process by which building blocks (nanoparticles or nanocrystals) spontaneously and autonomously adopt a designated spatial arrangement to form a structure.[5,6,26] More detailed and nuanced definitions have been proposed to capture the role of directed or encoded assemblies (via chemical linkers, hydrogen bonding, hydrophobicity, patchiness, etc)[6,27] and the promise of programmability triggered by responses to specific stimuli (heat, light, pH, humidity, mechanical shear, etc).[28] In any case, the random and spontaneous diffusion of nanoscale building blocks in a fluid is driven by Brownian (thermal) motion and their assembly is primarily controlled by manipulating the interaction forces acting between them.[5] For self-assembly specifically, these interaction forces are typically non-covalent in nature and relatively weak including van der Waals attractions, depletion attractions, steric repulsions, electrostatic repulsions, among others. They can lead to static assemblies that adopt the thermodynamic equilibrium state or dynamic assemblies trapped by a kinetic process in a metastable state sensitive to perturbations.[29]

COLLOIDAL STABILITY

The predictive and controlled assembly of structures, irrespective of length scale, begins with colloidally stable building blocks. The theory developed by Derjaguin, Landau, Verwey, and Overbeek (DLVO) describes colloidal stability as the balance between the attractive (van der Waals) and repulsive (electrostatics and/or sterics provided by an adsorbed molecule) forces acting on the particles. The total interaction pair potential, which is the sum of the relevant attraction and repulsion potentials, predicts whether an energetic barrier that prevents the irreversible aggregation of particles as they approach each other exists (Figure 1.1).[23,25,30]

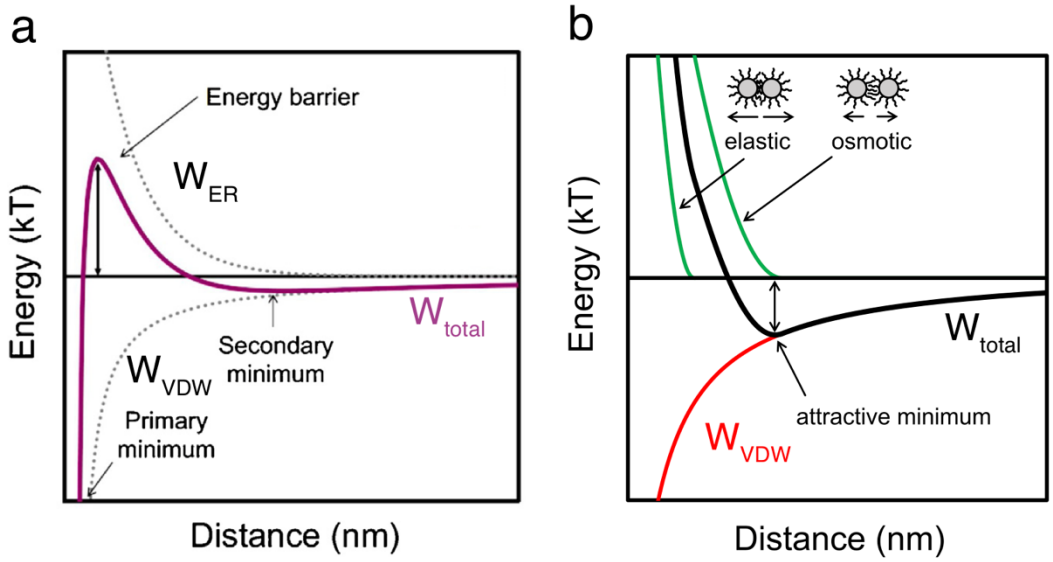

Figure 1.1: Representative plots of pair interaction potentials.

a) Influence of van der Waals attractions and electrostatic repulsions and b) influence of van der Waals attractions and steric repulsions. Adapted from reference 23.

Applying the Derjaguin approximation for curved surfaces, the van der Waals attraction (W_{vdw}), electrostatic repulsion (W_{ER}), and steric repulsion (W_{SR}) potentials between two spherical particles are written as:

$$W_{vdw}(h) = -\frac{A}{6}\left[\frac{2R^2}{h^2+4Rh} + \frac{2R^2}{h^2+4Rh+R^2} + \ln\left(\frac{h^2+4Rh}{h^2+4Rh+R^2}\right)\right] \quad (1)$$

Where, A is the Hamacker constant, R is the radius of the sphere, and h is the separation distance between the surface of the spheres (not the center-to-center distance).[25] The Hamacker constant depends on the composition of the particles and dielectric constant and refractive index of the solvent.

$$W_{ER}(h) = \frac{64\pi kTRn_s\gamma^2}{\lambda_D^2} e^{-\lambda_d \cdot h} \quad (2)$$

$$\gamma = \tanh\left(\frac{Ze\Psi_0}{4kT}\right) \quad (3)$$

$$\lambda_d = (\frac{2Z^2 n_s e^2}{\varepsilon\varepsilon_0 kT})^{\frac{1}{2}} \quad (4)$$

Where, k is Boltzmann's constant, T is temperature, R is the radius of the sphere, h is the separation distance between the surface of the spheres, Z is the charge of the ions, e is the elementary charge, Ψ_0 is the surface charge, n_s is the bulk ionic concentration, ε is the dielectric constant of the solvent, and ε_0 is the vacuum permittivity. γ is derived from the Gouy-Chapman theory and λ_d^{-1} is the Debye screening length.[25]

$$W_{SR}(h) = \begin{cases} W_{osm}(h) & l < h < 2l \\ W_{osm}(h) + W_{elas}(h) & 0 < h < l \end{cases} \quad (5)$$

$$W_{osm}(h) = \frac{4\pi RkT\phi^2}{\upsilon}(\frac{1}{2} - \chi)\begin{cases} \left(l - \frac{h}{2}\right)^2 & l < h < 2l \\ \left[l^2\left(\frac{h}{2l} - \frac{1}{4} - \ln\left(\frac{h}{l}\right)\right)\right] & 0 < h < l \end{cases} \quad (6)$$

$$W_{elas}(h) = \frac{2\pi RkTl^2\rho\phi}{MW}\left[\frac{h}{l}\ln\left(\frac{h}{l}\left(\frac{3-\frac{h}{l}}{2}\right)^2\right) - 6\ln\left(\frac{3-\frac{h}{l}}{2}\right) + 3\left(1 - \frac{h}{l}\right)\right] \quad (7)$$

Where, R is the radius of the sphere, l is the length of the stabilizing layer, h is separation distance between the surface of the spheres, k is Boltzmann's constant, ϕ is the volume fraction of the adsorbed molecule (short hydrocarbon chain, polymer, DNA, etc) assuming a uniform profile, υ is the molar volume of the solvent, χ is the Flory-Huggins parameter, ρ is the density of the adsorbed molecule, and MW is the molecular weight of the adsorbed molecule.[31] W_{osm} is the potential energy associated to the increase in osmotic pressure as two surfaces coated with soft and swollen molecules approach each other while W_{elas} captures the energy of elastic compression/deformation when the stabilizing molecule chains collide and overlap according to the theories developed by Napper[32] and de Gennes.[33]

According to these equations, the conditions that determine the strength of repulsions and therefore colloidal stability can be classified in two categories: i) the solvent

environment (temperature, ionic strength, and dielectric constant for electrostatics as shown in Figure 1.2a-c and molar volume for sterics) and ii) surface chemistry (surface charge for electrostatics as shown in Figure 1.2d and the coverage, length, density, molecular weight, and solvent compatibility of the adsorbed molecules for sterics). At the nanoparticle level, sought-after surface chemistry characteristics can be targeted directly during synthesis, while additional features or more complex functionalizations can be achieved post-synthetically using ligand exchange methods. Finally, the dependence on the solvent environment allows to tune these interactions in a reversible way and using external stimuli, irrespective of the nature of the nanoparticles, thus offering an additional level of control and versatility.

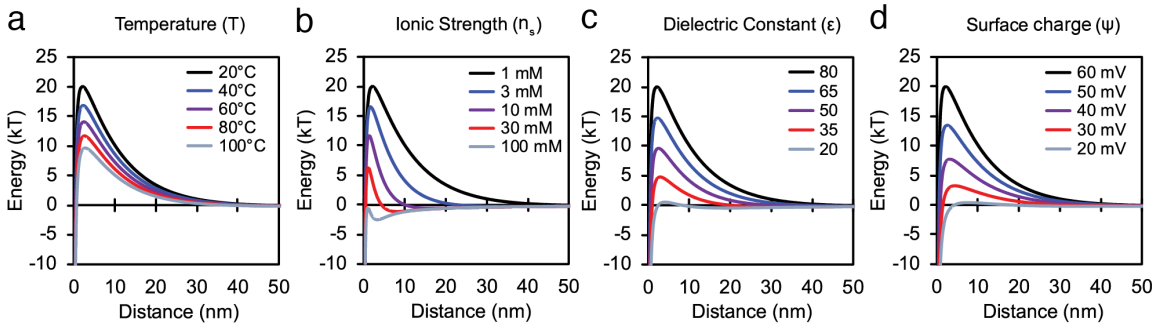

Figure 1.2: Effect of solvent environment and particle surface chemistry on electrostatic repulsion potential.

a) Temperature, b) ionic strength, c) dielectric constant of the solution, and d) surface charge. Adapted from reference 23.

DEPLETION ATTRACTIONS

In this work, the primary interparticle interaction that is studied and tuned is depletion attractions between nanocrystals. Consider a binary mixture of a primary colloid stabilized by electrostatic and/or steric repulsions and a smaller non-adsorbing co-solute (depletant). Above a critical depletant concentration, an imbalance in the osmotic pressure in solution triggers short-range physical attractions between the primary colloids in an effort to increase the configurational entropy of the depletants. Pushing the primary

colloids closer together leads to the overlap of the excluded volumes, which are not accessible to the depletants, and therefore an effective increase in the volume occupied by the depletants (Figure 1.3). A unique characteristic of depletion attractions is the ability to simply and independently tune the strength and range of attraction by changing the relative sizes of the primary colloid and the smaller cosolute (depletant) and the depletant concentration (equations 8 and 9).[25,34]

Experimental observations of depletion attractions (aggregation of latex particles, emulsion droplets, red blood cells, and viruses to name a few) can be traced back to as early as the 1930s, but it would take 2 more decades to rationalize this interparticle interaction and formulate a theory. The Asakura-Oosawa depletion potential is written as:

$$W_{dep}(h) = \begin{cases} \infty & h < 0 \\ -\Pi_{osm} V_{ov}(h) & 0 \leq h \leq \sigma \\ 0 & h > \sigma \end{cases} \quad (8)$$

Where $\Pi_{osm} = n_b kT$ is the osmotic pressure, n_b is the depletant number density (concentration), k is Boltzmann's constant, T is temperature, V_{ov} is the overlap excluded volume, h is the separation distance between the surface of the spheres, and $\sigma/2$ is the thickness of the depletion layer, which is typically equal to the size of the depletant (e.g. the radius of gyration). For spheres,

$$V_{ov}(h) = \frac{\pi}{6}(\sigma - h)^2 \left(3R + \sigma + \frac{h}{2}\right) \quad (9)$$

Because the excluded volume depends on the geometry of the particles, the strength of depletion attractions will vary as a function of shape and will be greater for particle shapes that maximize the overlap of the excluded volume (i.e., faceted particles).

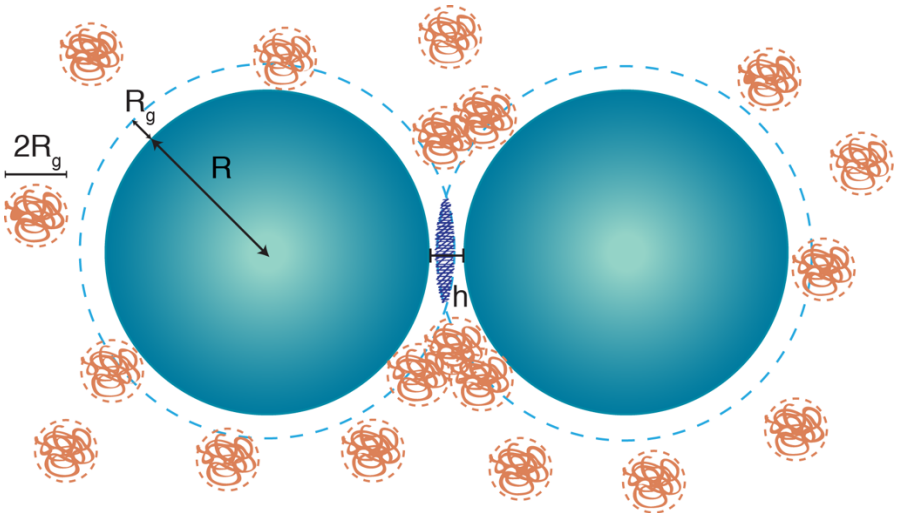

Figure 1.3: Schematic of two spherical colloids experiencing depletion attractions. The excluded volume is represented by the dashed blue circles with a depletion layer of thickness equal to R_g ($\sigma/2$ using the equation notation) and the overlap excluded volume is represented by the hatched region. Depletants are penetrable hard spheres that cannot access the interparticle gap of with h. Adapted from reference 35.

For specific depletant-to-colloid size ratio and colloid volume fraction ranges, exceeding a depletant concentration may induce phase transitions (e.g., fluid-fluid or fluid-solid). To predict the phase behavior, we use analytical expressions of the free energy derived from free volume theory and scaled particle theory. Details of these calculations are found in Appendix 1 and 2.[35,36]

COLLOIDAL GELS

Broadly, a colloidal gel is a disordered network composed of particles in a continuous liquid phase that exhibits solid-like elastic properties due to its non-flowing and arrested state. In this case, gelation involves creating irreversible covalent bonds or reversible and long-lived physical bonds between colloidally stable particles in solution. These attractive interactions drive a fluid to solid phase transition through a thermodynamic unstable region, where colloid-rich and colloid-poor phases coexist.[37,38] Unlike in crosslinked polymer gels, where a network of entangled chains traps the solvent,

formation of a gel phase occurs when the growth of aggregates is kinetically arrested, therefore suppressing complete phase separation into a dense solid or glass (Figure 1.4).[37,38]

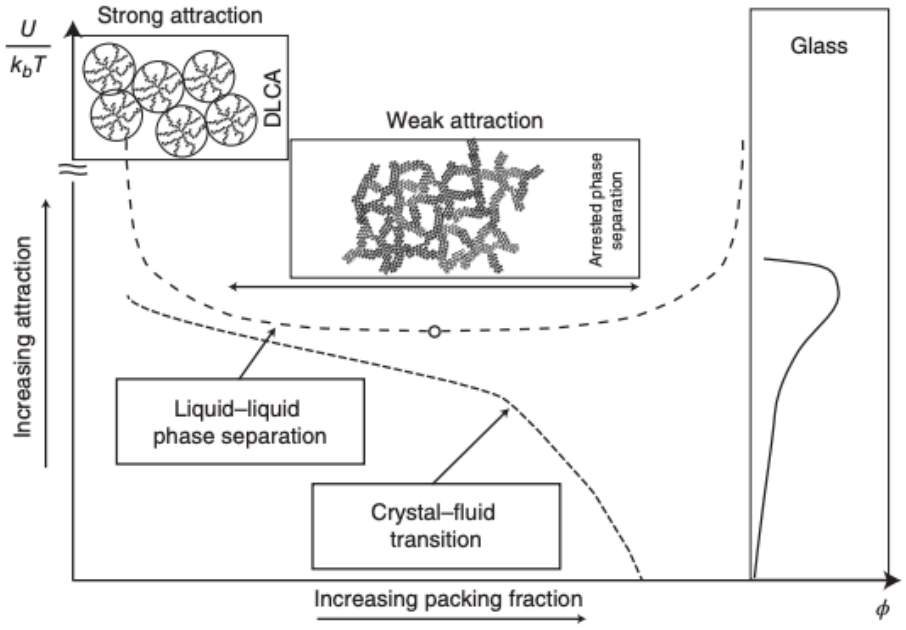

Figure 1.4: Schematic phase diagram for colloids dispersed in solution interacting by short-range attractions.

Reproduced from reference 38.

This transition is detected by tracking changes in the rheological, scattering, and morphological signatures of the material.[20,39-41] Regarding structure specifically, colloidal gels typically yield mass fractals, which means that the assembled object exhibits self-similarity since its mass scales as a power law irrespective of the characteristic length scale of the aggregate as shown in equation 10:

$$M \propto \left(\frac{R_g}{R}\right)^{D_f} \tag{10}$$

Where M is the mass, R_g is the radius of gyration of the aggregate, R is the radius of the primary particle, and D_f is the fractal dimension with values ranging from 1 to 3 (1 corresponding to a linear aggregate and 3 to a fully space filling three-dimensional aggregate, respectively). Theoretical and experimental studies have shown that the D_f

characteristic of the topology of the gel network is determined by the total pair interaction potential, which is in turn dependent on the physicochemical properties of the colloids. Two primary aggregation regimes have been established: Diffusion-Limited Cluster Aggregation (DLCA) and Reaction-Limited Cluster Aggregation (RLCA).[42-44] DLCA arises when repulsions are negligible, leading to chain-like open structures with low D_f (1.7-1.8) due to fast aggregation kinetics, whereas RLCA assembles denser and globular-like structures with higher D_f (2.0-2.2) because repulsions strongly compete with attractions and slow down the kinetics of aggregations. Furthermore, fractality has been shown to emerge universally across different classes of colloidal assemblies and gels,[45] thus providing an already established framework of underlying physics to study the interplay between interparticle interactions and structure in emergent semiconductor metal oxide nanocrystal gels.

The inception of inorganic nanoparticle gels, which can be traced back to the early and mid 2000s, drew inspiration from molecular sol-gel chemistries to covalently attach nanoparticles through the oxidative removal of the stabilizing ligands on the surface using hydrogen peroxide.[46-48] Compared to molecular sol-gel, where nanoparticles are formed from molecular precursors or salts in solution and subsequently crosslinked, the main advantages of crosslinking preformed nanoparticles are improved control over the size, shape, and uniformity of the building blocks, direct assembly of nanocrystals (molecular sol-gels yield amorphous networks that need an annealing step to crystallize the material), higher porosity and surface area-to-volume ratios, and compatibility with multicomponent assemblies.[21,23] This gelation method has been successfully applied to broad classes of inorganic materials such as metal chalcogenides, noble metals, and metal oxides.[21-23] Remarkably, this approach has achieved macroscopic materials with strong photoluminescence reflective of the unique optical properties of metal chalcogenide quantum dots or enhanced catalytic activity in the case of noble metal nanoparticle gels.[21,22] However, preserving the inherent nanoscale optical properties has required protecting quantum dots with a sacrificial metal chalcogenide shell or has not been possible for plasmonic noble metals because the nanoparticles are prone to sintering,[47,49,50] therefore

losing their distinctive nanostructure. Moreover, precise micro and macrostructural control of the gel network is impeded by controlled ligand stabilization since fast aggregation kinetics typically lead to compact, sedimented, opaque, and cracked materials.

To circumvent these challenges, an alternative gelation method based on forming chemical bridges between surface-bound ligands to aggregate nanoparticles was developed.[50-52] In this case, the extent and kinetics of aggregation and even the phase behavior can be gradually tuned depending on the amount of bonds formed by chemical bridges.[53,54] When charged inorganic species mediate the assembly via ionic coordination, all-inorganic networks that facilitate charge transport pathways between neighboring semiconductor nanocrystals are achieved. Moreover, chemical bridges can also be designed to be reversible, specific, and responsive, which offers the potential for dynamic and programmable nanocrystal gelation.[28,55] However, chemical gelation, whether covalent or ionic in nature, is limited to specific surface chemistries that are not easily adaptable across noble metals, metal chalcogenides, and metal oxides unless suitable ligand exchanges[56] are developed or new coordination chemistries are designed.

Recently, efforts to assemble versatile and multicomponent nanocrystal gels have shifted towards employing non-specific physical interactions, mostly by leveraging electrostatics.[57,58] In spite of the significant and fast-paced progress on various aspects of nanocrystal gelation including assembly, processing, characterization, and applications over the last decade, rich opportunities to fundamentally engineer interparticle interactions towards the rational design of structures, properties, and novel functionality in these materials remain to be investigated and merit to be uncovered. This dissertation aimed to contribute to these possibilities by introducing depletion attractions, a physical and entropic interaction extensively studied in soft matter colloidal gels, to the realm of inorganic nanocrystal gels.

DISSERTATION OVERVIEW

This dissertation sought to demonstrate, characterize, and engineer the assembly of metal oxide nanocrystal gels via polymer-mediated depletion attractions. Since these

interactions have been traditionally and extensively studied with polymer microparticles rather than inorganic nanoparticles, gelation principles at the nanoscale needed to be established by experimentally discovering appropriate self-assembly conditions (building blocks, solvents, colloidal stability, surface chemistry, and volume fractions) and theoretically validating the observed phase behavior and proposed self-assembly mechanism. Given the significance of integrating nanoscale properties into bulk materials and their sensitivity to the spatial arrangement of nanocrystals, conditions leading to optically active assemblies were identified and their morphology and structure were characterized in an effort to understand the collective emergent properties.

The study in Chapter 2, describes how polyethylene glycol depletants mediate depletion attractions between charge-stabilized tin-doped indium oxide nanocrystals to form gels. This system serves as a proof of concept to investigate phase transitions as a function of depletant concentration, probe the structure of depletion gels with electron microscopy and X-ray scattering and diffraction techniques, compare experimental observations to theoretical predictions, and achieve an optically active gel with a strong infrared absorption reflective of both the discrete nanocrystals and the microstructure of the network. Because polyethylene glycol adsorbs on the surface of tin-doped indium oxide, a bridging gel and reentrancy into a fluid regime were observed at intermediate depletant concentration below the depletion gel threshold.

Chapter 3 builds on the aforementioned progress and expands on the assembly capabilities of depletion attractions, notably the physical and non-specific origin of the interactions and the dependence of attraction strength on the shape of the primary colloid. The universality of the gelation approach is demonstrated by applying depletion attractions to three types of metal oxide nanocrystals: iron oxide spheres, tin-doped indium oxide spheres, and fluorine, tin-codoped indium oxide cubes. Because the nanocrystals are of similar and uniform size, the same depletant can be used to induce attractions with an approximately equal range relative to the size of the nanocrystal, which allow us to compare quantitatively the gelation thresholds of each system by fixing the nanocrystal volume fraction. Specifically, spherical nanocrystals form gels at the same depletant

concentration, irrespective of their composition, and cubic nanocrystals form gels at a lower depletant concentration relative to spherical nanocrystals due to face-to-face packing during assembly. Once more, the experimental phase behavior is validated with theoretical predictions to assess our proposed assembly mechanism and rationalize the influence of nanocrystal shape. X-ray scattering characterization of the dispersions and gels reveals that excellent initial colloidal stability results in gels that scatter as mass fractals with a single characteristic length scale, unlike in the system reported in Chapter 2. In addition, the nanocrystals are not as susceptible to bridging attractions since only minimal clustering is observed and bridging gelation is not detected in the timescale of depletion gelation.

In an effort to simultaneously improve colloidal stability, diversify the solvent compatibility, grant additional properties to the nanocrystals, and protect the surface from bridging attractions during self-assembly, a method to functionalize tin-doped indium oxide nanocrystals with a polymer is developed in Chapter 4. A hydrophilic and biocompatible copolymer of polyacrylic acid grafted with polyethylene oxide appendages is adsorbed on the nanocrystal surface to produce aqueous dispersions. The solvent conditions (pH and chemical species present in solution) conducive to appropriate polymer wrapping and thus good colloidal stability were explored using a combination of electron microscopy, dynamic light scattering, infrared spectroscopy, and thermogravimetric analysis. The influence of the extent of polymer wrapping on the spectroelectrochemical properties inherent to tin-doped indium oxide nanocrystals was investigated in thin film composites. Although the gelation of polymer-wrapped nanocrystals was not demonstrated, this study establishes guidelines to achieve colloidally stable dispersions of tunable steric repulsions and emergent properties in the composite as a function of polymer coverage, thus motivating the applicability of these dispersions as potential building blocks for nanocrystal gels.

Finally, Chapter 5 motivates and discusses potential future extensions of this dissertation work with an outlook towards accessing the full potential of depletion attraction in nanocrystal systems, understanding the influence of the nano- and

microstructure of the network on the properties of macroscopic gels, and ways to engineering complex, stimuli-responsive, and self-healing functional nanocrystal gels.

Chapter 2: Gelation of Plasmonic Metal Oxide Nanocrystals by Polymer-Induced Depletion-Attractions*

Gelation of colloidal nanocrystals emerged as a strategy to preserve inherent nanoscale properties in multiscale architectures. However, available gelation methods to directly form self-supported nanocrystal networks struggle to reliably control nanoscale optical phenomena such as photoluminescence and localized surface plasmon resonance (LSPR) across nanocrystal systems due to processing variabilities. Here, we report on an alternative gelation method based on physical internanocrystal interactions: short-range depletion attractions balanced by long-range electrostatic repulsions. The latter are established by removing the native organic ligands that passivate tin-doped indium oxide (ITO) nanocrystals while the former are introduced by mixing with small polyethylene glycol (PEG) chains. As we incorporate increasing concentrations of PEG, we observe a reentrant phase behavior featuring two favorable gelation windows; the first arises from bridging effects while the second is attributed to depletion attractions according to phase behavior predicted by our unified theoretical model. Our assembled nanocrystals remain discrete within the gel network, based on X-ray scattering and high-resolution transmission electron microscopy. The infrared optical response of the gels is reflective of both the nanocrystal building blocks and the network architecture, being characteristic of ITO nanocrystals' LSPR with coupling interactions between neighboring nanocrystals.

INTRODUCTION

Nanocrystals, owing to their unique and highly tunable optical properties,[1,59-62] hold promise as key constituents in next-generation optoelectronic materials and devices.[11,14,59,63-65] Rich opportunities to enhance and diversify materials functionality

* This chapter has been adapted with permission from reference 143, copyright © 2018, Proceedings of the National Academy of Sciences of the United States of America. Written in collaboration with Gary K. Ong, Ryan B. Jadrich, Beth A. Lindquist, Ankit Agrawal, Thomas M. Truskett, and Delia J. Milliron. C.A.S.C. wrote the manuscript, conceived experiments, prepared ITO dispersions and gels, conducted electron microscopy, DLS, zeta potential, FTIR, ICP, SAXS, and spectroscopy characterization, and analyzed the data.

motivate the development of multiscale nanocrystal architectures via bottom-up approaches[6] because the collective properties of nanocrystals in assemblies depend on their organization. Nanoscale optical phenomena such as photoluminescence and localized surface plasmon resonance (LSPR) are especially responsive to electronic and electromagnetic coupling arising between nanocrystals in close proximity. This effect is reflected in the optical properties of extended and dense nanocrystal assemblies with a high degree of internanocrystal connectivity (e.g., superlattices[66,67] and films[68]), which deviate from those of their isolated components. Nanocrystal gels, where nanocrystal building blocks are directly assembled into solid-like networks (i.e., a scaffold is not needed to form a stable gel), provide a unique framework to explore such structure-property relationships by allowing control over nanocrystal volume fraction, nanocrystal valence,[53,69,70] and network topology (shape,[71] size,[71,72] and density[73] of aggregates) in ways not typical of higher density and ordered assemblies. Nanocrystal gels' potential to exhibit properties both dependent on their self-assembled architecture and reflective of their nano-sized building blocks has been realized for semiconductor quantum dot gels and aerogels,[21] which exhibit excitonic photoluminescence red-shifted from the luminescence of isolated quantum dots due to energy migration through the gel network. However, plasmonic metal nanoparticles such as gold or silver fuse into wire-like networks when assembled into self-supported nanoparticle gels, obliterating the LSPR optical response characteristic of the isolated nanoparticles.[50,74] We sought a new strategy for gelation using physical bonding interactions, which we hypothesized could maintain the discrete morphology of LSPR-active metal oxides intact, to target LSPR-active nanocrystal gels. Our approach is not specific to the chemistry of the nanocrystals employed and could potentially enable a broad class of gels assembled from diverse nanoscale components capable of reflecting their individual properties.

Gelation of colloidally stable nanocrystal dispersions is achieved by balancing attractions and repulsions. In previously published examples, these interactions are simultaneously tuned by progressive oxidative ligand removal or controlled chemical

bridging between surface bound species and linking agents (e.g., ions or molecules). The former has been adapted across noble metal,[49,74-77] metal chalcogenide,[46,47,73,78,79] and metal oxide[80-84] systems, but this method is prone to fuse nanocrystals (i.e., eliminate interparticle spacing) as their exposed surfaces come in contact due to a lack of stabilization, which consequently limits the realization of size- and shape-dependent optical properties (i.e., photoluminescence and LSPR) within nanocrystal gels. While gelation via chemical bridging is a viable strategy to mitigate nanocrystal fusing, translating this approach across nanocrystal materials requires customizing surface functional groups for specific nanocrystal compositions, so far limited to metal chalcogenide nanocrystals[52,56] and gold nanoparticles.[50] However, even this approach did not prevent fusing of gold nanoparticles into nanowires with a concomitant loss of LSPR response. Among the sparse reports on metal oxide nanocrystal gels, gelation has been most often achieved by fusion upon ligand removal[82-84] or by triggering the entanglement of concentrated anisotropic nanoparticles: titania chains generated by oriented attachment of destabilized nanocrystals[81,85-87] form gels upon heating, while tungsten oxide nanowires[88] and yttria nanosheets[89] form gels upon centrifugation. Once more, this approach offers limited control over gel structure and thereby the associated properties, and it cannot be easily generalized to assemble discrete isotropic metal oxide nanocrystals.

In light of these limitations, we were motivated to develop an alternative route for nanocrystal gelation based upon nonspecific physical interactions by combining depletion attractions and electrostatic repulsions. Previous studies have demonstrated that this combination can help drive the gelation of polymer colloids[40,90,91] and the assembly of proteins (into gels,[92] clusters,[93] and crystals[94,95]), and hence it holds potential for tunable gelation of nanocrystals. Conceptual understanding of the strength and the range of depletion attractions requires consideration of only a few parameters: the concentrations of the primary colloid and the depletant (smaller, weakly interacting cosolute) and their relative dimensions. The addition of long-range repulsions to depletion interactions can favor “open” gel structures as opposed to dense colloidal phases.[69,71,96] Therefore, a method

to controllably introduce repulsive forces, here electrostatics, is needed to realize nanocrystal gelation via physical depletion attractions.

In this study, we demonstrate PEG-mediated gelation of ITO nanocrystals stripped of their native ligand shell. The ligand removal procedure employed here prevents ITO fusion into wire-like morphologies, in part by promoting electrostatic stabilization of nanocrystals as a colloid. Accordingly, bare ITO nanocrystal surfaces enable long-range repulsions, while introducing short-chain PEG triggers depletion attractions. We investigate the influence of PEG concentration ([PEG]) on competing internanocrystal interactions for a fixed nanocrystal volume fraction, and we observe two gelation thresholds at distinct [PEG], each preceded by a fluid regime (i.e., flowing dispersion) of discrete nanocrystal clusters. Since PEG is known to adsorb onto acidic metal oxide surfaces, we attribute the emergence of a first gelation window at low [PEG] to bridging of neighboring ITO nanocrystals by PEG chains, while the higher [PEG] gelation window is attributed to depletion attractions. To support our assertion and assess the gelation mechanism, we compare our experimental results to thermodynamic phase behavior predictions from a unified theory formulated to capture polymer-mediated bridging and depletion-attractions. Our gelation approach effectively achieves optically active and transparent gels with LSPR similar to that of discrete ITO nanocrystals, but shifted and broadened by internanocrystal coupling. To explore the influence of network topology on optical properties, we perform far-field and near-field electromagnetic simulations based on structural information extracted from small-angle X-ray scattering (SAXS). Our simulation results predict near-field enhancement manifested as “hot spots” within the gel network that may be leveraged in future studies for energetic coupling between LSPR and molecular vibrational modes,[10] or other optical transitions.[97]

EXPERIMENTAL METHODS

ITO Nanocrystal Synthesis and Ligand Stripping

ITO nanocrystals were synthesized in an air-free environment using a standard Schlenk line technique following a procedure adapted from previous literature reports.[98,99] Briefly, 2.5 g (8.6 mmol) of indium acetate and 0.225 g (0.95 mmol) of tin acetate were mixed with 10 mL of oleylamine, degassed under vacuum for 1 hour at 120 °C, and then heated to 230 °C under inert nitrogen atmosphere for 1 hour to nucleate and grow the nanocrystals. After the reaction, the mixture was diluted with 5 mL of hexane and 1 mL of oleic acid and transferred to a centrifuge tube. The resulting nanocrystals were recovered and purified by performing five cycles of precipitation with reagent alcohol, centrifugation, and re-dispersion in hexane.

To remove the hydrophobic ligands bound to the nanocrystal surface, 60 mg of nitrosonium tetrafluoroborate were added to a two-phase mixture containing equal volumes of dimethylformamide (2 mL) and nanocrystal dispersion in hexane (50 mg/ml, 2 mL) following a procedure reported previously.[100] The mixture was sonicated for 1 hour to promote the transfer of bare nanocrystals to the polar aprotic dimethylformamide layer, a process visible to the naked eye since the hexane layer turns clear and the dimethylformamide layer adopts a blue/green color. After discarding the hexane layer, the ligand-stripped nanocrystals were purified by performing seven cycles of precipitation with toluene, centrifugation, and redispersion in dimethylformamide. Chemically removing the native oleate/oleylamine ligands on the metal oxide surface results in charge-stabilized nanocrystals with strongly positive zeta potentials in both acetonitrile and dimethylformamide.

Nanocrystal hydrodynamic diameter and zeta potential before and after ligand stripping were measured with a Malvern Zetasizer Nano ZS. Samples were prepared by diluting the nanocrystal dispersions to ~1 mg/ml and filtering them through a polytetrafluoroethylene membrane. Dynamic light scattering samples were placed in a disposable plastic micro cuvette (ZEN0040, Malvern) while zeta potential samples were

placed in a glass cuvette and measured with a dip cell (ZEN1002, Malvern). The isoelectric point of ligand-stripped nanocrystals was determined by measuring zeta potential as a function of pH using Malvern's MPT-2 autotitrator. Ligand-stripped ITO nanocrystals were dispersed in 1 mM hydrochloric acid aqueous solution and titrated with a 0.1 M sodium hydroxide solution followed by a titration with a 0.1 M hydrochloric acid solution in a folded capillary zeta cell (DTS1070, Malvern). Fourier-transform infrared spectra of nanocrystals before and after ligands stripping were recorded with a Burker-Vertex 70/70v spectrometer. The films were dropcasted from dilute dispersions (~ 1 mg/ml) on calcium fluoride infrared-transparent windows.

ITO-PEG Assemblies

Purified ligand-stripped ITO nanocrystals were dispersed in 8.00 mM (based on M_n=1100 g/mol) PEG in acetonitrile solution (final concentration 4.00 vol. % by inductively coupled plasma-atomic emission spectroscopy). The dispersion was stirred at 600 rpm for 48 hours to ensure colloidal stability and homogeneity. This mixture was used as a stock dispersion to obtain the higher [PEG] assemblies. Varying amounts of PEG were added to 300 µL aliquots of the ITO-PEG stock dispersion to form flowing dispersions or gels: 12.48 mg (final [PEG]= 46.0 mM), 25.62 mg (final [PEG]= 85.8 mM), 86.69 mg (final [PEG]= 271 mM), 173.43 mg (final [PEG]= 534 mM). After the final amount of PEG was added, each mixture was sonicated for one minute to dissolve the PEG. The dispersions were kept in sealed vials and remained unperturbed during the self-assembly process.

Electron Microscopy

Samples were prepared by dropcasting 5 µL of dilute nanocrystals dispersed in hexane and acetonitrile for ligand-capped and ligand-stripped ITO nanocrystals, respectively, onto a copper grid (Pelco® ultrathin carbon-A 400 mesh, Ted Pella). The ITO-PEG gel ([PEG]= 534 mM) was freeze-dried (immersion in liquid nitrogen for 1 min

followed by vacuum drying for 15 min) and diluted with ethanol before dropcasting onto a copper grid. Transmission electron microscopy images were captured on a JEOL 2010F instrument with a Schottky Field Emission source operated at 200 kV.

Small-angle X-ray Scattering Measurements and Analysis

SAXS measurements were performed at the Lawrence Berkeley National Laboratory Advance Light Source beamline 7.3.3 at 3.8 m sample-detector distance. A silver behenate standard[101] was used to calibrate the scattering spectra. All ITO-PEG samples were enclosed in flame sealed glass capillaries (Charles-Supper Company, Boron Rich, 1.5 mm diameter, 0.01 mm wall thickness) and measured in transmission configuration. Capillaries containing neat acetonitrile were used for background subtraction. The Igor Pro-based Nika software[102] for two-dimensional (2D) data reduction was used for instrument calibration and to convert 2D detector data into 1D data by circular averaging. Before fitting, each pattern was background subtracted following a procedure described in a previous publication[51] using the Irena tool suite for modeling and analysis in Igor Pro.[103] The high-q nanocrystal scattering contribution in each ITO-PEG pattern was individually fitted to a spheroid form factor using the Modelling II tool in Irena. The scattering contrast $(\Delta\rho)^2$ for 9.65 at. % tin-doped ITO nanocrystals in acetonitrile was calculated and set to $2119 \cdot 10^{20}$ cm^{-4}. The structure factor S(q) was approximated as I(q)/P(q), where I(q) is the total scattering intensity and P(q) is the form factor, assuming a decoupling approximation (nanocrystal size and shape are not correlated with position) and a local monodisperse approximation.[20]

X-ray Diffraction

Diffraction patterns were collected on a Rigaku R-Axis Spider using Cu K_α radiation. The ligand-stripped nanocrystals and ITO-PEG gel ([PEG]= 534 mM, identical sample measured by SAXS) were enclosed in glass capillaries and were measured in transmission configuration. Crystallite sizes were determined by Scherrer analysis and a

lanthanum hexaboride (LaB_6) reference provided by the National Institute of Standards and Technology was used to correct for instrumental broadening.

Spectroscopy

Absorption spectra were collected on an Agilent-Cary 5000 UV-Vis-NIR spectrophotometer and a Burker-Vertex 70/70v Fourier-transform infrared spectrometer. Nanocrystal dispersions in acetonitrile and the ITO-PEG gels were measured in an infrared-transparent liquid cell with calcium fluoride windows of 0.5 and 0.02 mm path length, respectively. Extinction cross sections were calculated using the Beer-Lamberts law and volume fractions determined from inductively coupled plasma-atomic emission spectroscopy measurements (ICP-AES). Details on ICP-AES analysis and COMSOL simulations are described in Appendix 1.

RESULTS AND DISCUSSION

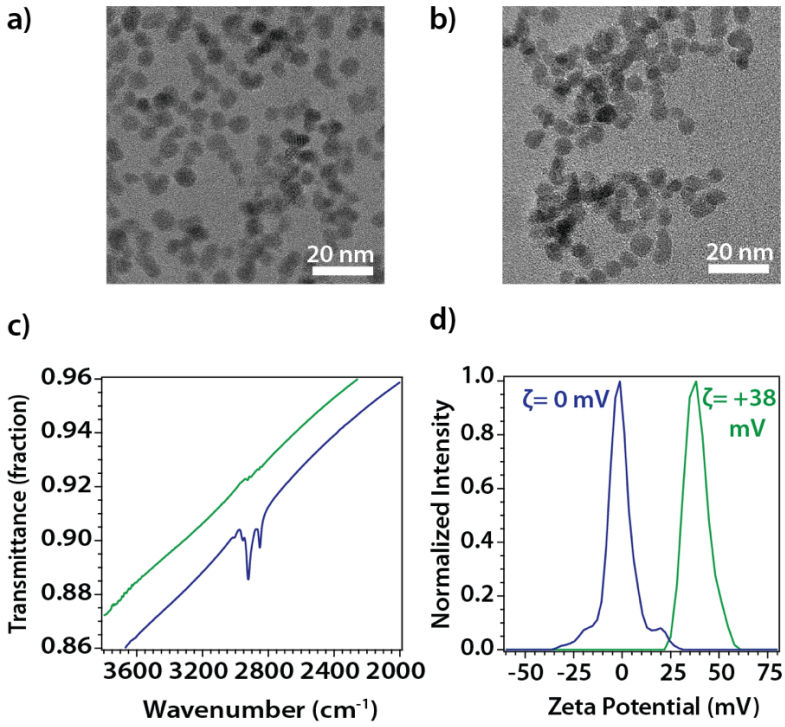

Figure 2.1: Surface chemistry of as-synthesized and ligand-stripped ITO.

a) Transmission electron microscopy image of as-synthesized nanocrystals, b) transmission electron microscopy image of ligand-stripped nanocrystals. No signs of etching or morphology change are observed after ligand removal, c) Fourier-transform infrared spectroscopy comparison of as-synthesized (blue) and ligand-stripped (green) nanocrystals. Effective ligand removal from the metal oxide surface is confirmed by the absence of characteristic oleic acid and oleylamine bands corresponding to -CH_2 (2922 and 2851 cm^{-1}) and =CH (3005 cm^{-1}) vibrational modes[104] in the spectrum of ligand-stripped nanocrystals. The sloping profile in the spectra corresponds to absorption due to LSPR, and d) zeta potential comparison of as-synthesized nanocrystals dispersed in hexane (blue) and ligand-stripped nanocrystals dispersed in acetonitrile (green). Unlike ligand-capped nanocrystals dispersed in non-polar solvents, the ligand-stripped nanocrystals exhibit strongly positive zeta potentials in both acetonitrile and dimethylformamide while retaining colloidal stability. This change in nanocrystal surface charge has been previously attributed to uncoordinated metal cations exposed upon removal of anionic ligands.[100,105]

Our nanocrystal gelation strategy leverages physical bonds formed by balancing long-range electrostatic repulsions due to surface charge and short-range attractions

induced by depletants, aiming to create stable open, arrested, and percolated networks. Charge-stabilized nanocrystals in acetonitrile with an average radius R_{ITO} of 2.83 ± 0.36 nm were selected as the primary colloid and the source of electrostatic repulsions (Figure 2.1). Short PEG polymer chains (M_n= 1100 g/mol) were selected as depletants based on the following criteria: the need for a co-solute with a radius of gyration, $R_{g\ PEG}$, smaller than R_{ITO}, PEG's ability to raise the osmotic pressure in solutions,[64] and PEG's compatibility with polar aprotic solvents. We estimated $R_{g\ PEG}$ of these PEG chains in acetonitrile to be 0.98 nm from SAXS sizing analysis (Appendix 1), which is in good agreement with the expected $R_{g\ PEG}$ from literature,[106] to ensure that the depletant size criterion would be fulfilled. More details on the characterization of ITO dispersions are included in Appendix 1. Previous studies on polymer-induced depletion-attractions have shown that the strength of the attraction is tunably increased as a function of depletant concentration, which in turn dictates the extent of the network's connectivity,[40,71] affecting gel structure and any properties dependent on the local environment and valence of nanocrystals in the network. Since colloidal nanocrystal depletion gels have not been previously reported, the conditions to induce gelation were discovered by varying the amount of PEG in a charge-stabilized nanocrystal dispersions of fixed volume fraction. Experimentally, as we progressively increase the PEG concentration at a fixed nanocrystal volume fraction (4.00 vol. %), we observe a fluid (i.e., flowing dispersion) up to a first threshold for gelation at [PEG]= 46.0 mM, then reentrant behavior back to a flowing dispersion, followed by a second occurrence of a gel at [PEG]= 534 mM (Figure 2.3, insets).

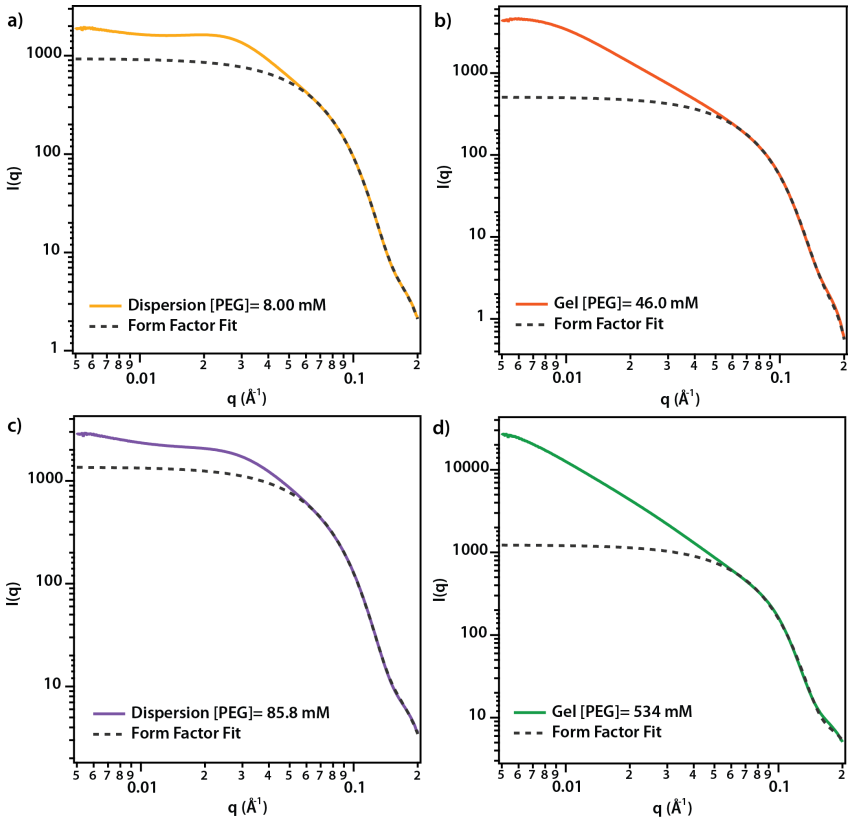

Figure 2.2: SAXS scattering intensity and form factor fitting.

a) ITO-PEG dispersion with [PEG]= 8.00 mM, b) ITO-PEG bridging gel with [PEG]= 46.0 mM, c) ITO-PEG dispersion with [PEG]= 85.8 mM, and d) ITO-PEG depletion gel with [PEG]= 534 mM. Experimental data is shown as a solid line while fits using the spheroid form factor model are shown as black dashed lines.

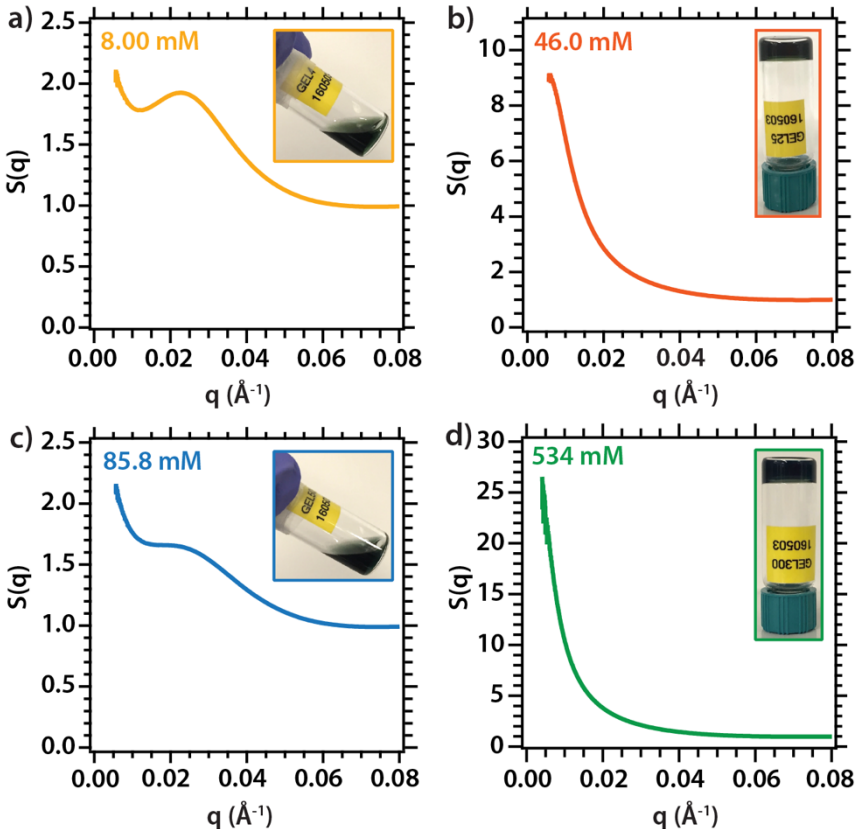

Figure 2.3: SAXS characterization of the ITO-PEG flowing dispersions and gels.

a) Structure factor S(q) of flowing dispersion with [PEG]= 8.00 mM, b) S(q) of gel with [PEG]= 46.0 mM, c) S(q) of flowing dispersion with [PEG]= 85.8 mM, and d) S(q) of gel with [PEG]= 534 mM. S(q) plots are accompanied with photograph insets of the corresponding ITO-PEG mixture.

To investigate the conditions that enabled gelation and to characterize the fluid regime, the ITO-PEG mixtures formed at different [PEG] were probed with SAXS. Specifically, we examine the structure factor S(q) as a function of [PEG] by removing the form factor contribution to the SAXS data (Figure 2.2) to gain insight into the physical origins of the self-assembly. As a result, we identify two distinct interaction regimes (Figure 2.3). First, we note a prominent S(q) peak (q~0.023 $Å^{-1}$) for the ITO-PEG flowing dispersion of lowest [PEG] emerging at a lower q than that indicative of correlations between directly adjacent nanocrystals, thus characteristic of intermediate range order in colloidal assemblies.[96,107,108] Considering the intermediate range order behavior of this

ITO-PEG mixture ([PEG]= 8.00 mM), we establish that competing short-range attractions and long-range repulsions frustrate large scale aggregation and lead to the formation of discrete nanocrystal clusters (~270 Å length scale). In addition, we observe similar intermediate range order behavior for the flowing dispersions in the reentrant regime (Figure 2.3c). Although the S(q) peaks near q~0.02 $Å^{-1}$ are less pronounced and broadened, likely due to an increase in attraction strength and cluster polydispersity, the presence of dispersed discrete clusters is still apparent in the reentrant regime. Second, in all cases, we observe that S(q) diverges as q approaches zero suggesting systems dominated by attractions and thermodynamic compressibility.[96,107] In particular, the S(q) intensity at the lowest resolvable q is approximately an order of magnitude higher when gelation occurs compared to the S(q) intensity of all flowing cluster dispersions (Figure 2.3b and d). Prior colloidal assembly studies[69,109-111] have reported a comparable S(q) intensity increase (of an order of magnitude or larger) when a colloidal system transitions from a fluid state to a gel through spinodal decomposition.

Further inspection of S(q) for both low and high [PEG] gels by employing Beaucage's unified function[112-114] approach for complex structures provides insight into the structural hierarchy of the gels and their respective fractal dimension (D_f). First, the number of apparent structural length scales along with their respective limits are determined from a derivative analysis (Figure 2.4). Following this method, we identify two distinct structural length scales in the S(q) of the high [PEG] gel whereas the S(q) of the low [PEG] gel only exhibits one. Thereafter, our derivative analysis results guide the S(q) unified fitting of both gels (Figure 2.5 and Table 2.1). While the S(q) of the [PEG] = 46.0 mM gel scatters as a mass fractal of D_f = 2.2, the S(q) of the [PEG]= 534 mM gel is composed of a mid-q (0.04 $Å^{-1}$ < q < 0.058 $Å^{-1}$) scattering contribution from nanocrystal clusters plus a low-q (0.01 $Å^{-1}$ < q < 0.02 $Å^{-1}$) scattering contribution attributed to the presence of a percolated fractal gel network (D_f = 2.09). For both low and high [PEG], we associate gelation with slow bonding kinetics since the fitted D_f values fall within the expected range (2.0-2.2) for reaction-limited cluster aggregation systems.[43,115,116]

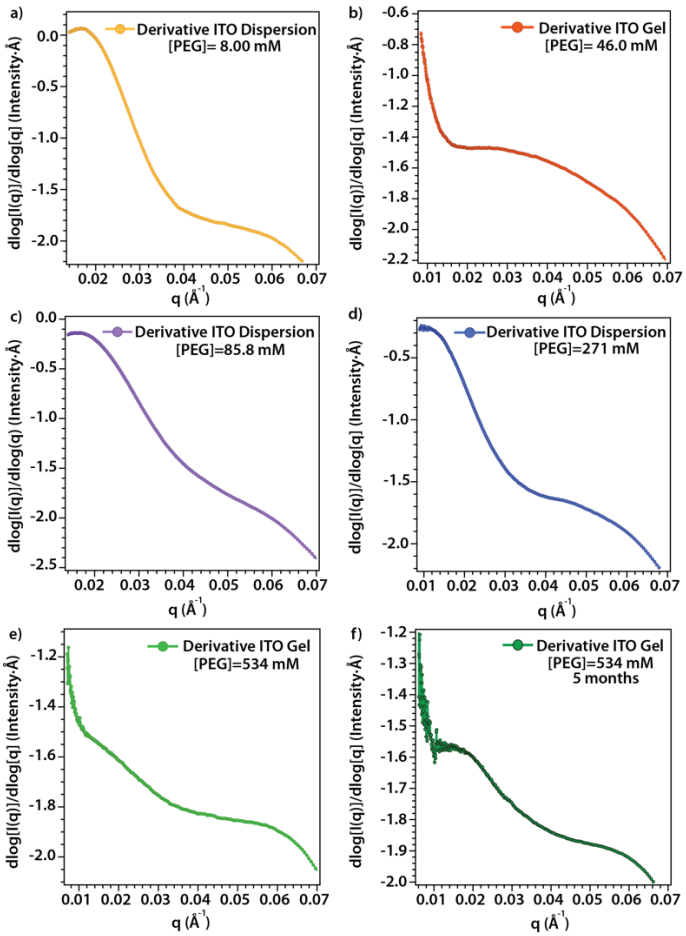

Figure 2.4: Identification of Porod regimes by derivative analysis.

Plots were obtained by taking the derivative of the scattering data presented in Figure 2.2. For scattering length scales larger than the nanocrystal form factor, a structural level is defined by a size, manifested as an exponential decay in the scattering intensity (Guinier's law), and a mass scaling regime in the form of a power-law relation (Porod's law).[113] Therefore, a Porod region is identified as a horizontal line when plotting the derivative of log [I(q)] with respect to log [q] as a function of q. a) ITO-PEG dispersion with [PEG]= 8.00 mM exhibits a narrow Porod regime around q~ 0.045 $Å^{-1}$, b) the Porod regime of the ITO-PEG gel with [PEG]= 46.0 mM is delimited by 0.016 $Å^{-1}$ < q <0.028 $Å^{-1}$, c) the Porod regime of the ITO-PEG dispersion with [PEG]= 85.8 mM is convoluted in the high and low q Guinier regimes, d) ITO-PEG dispersion with [PEG]= 271 mM exhibits a narrow Porod regime between 0.04 $Å^{-1}$ < q <0.045 $Å^{-1}$, e) ITO-PEG gel with [PEG]= 534 mM exhibits two Porod regimes: a mid-q Porod regime delimited by 0.04 $Å^{-1}$ < q <0.058 $Å^{-1}$ and a low q Porod regime delimited by 0.01 $Å^{-1}$ < q <0.02 $Å^{-1}$, f) derivative of the SAXS data for the ITO-PEG gel with [PEG]= 534 mM aged five month to further confirm the presence of a low q Porod regime.

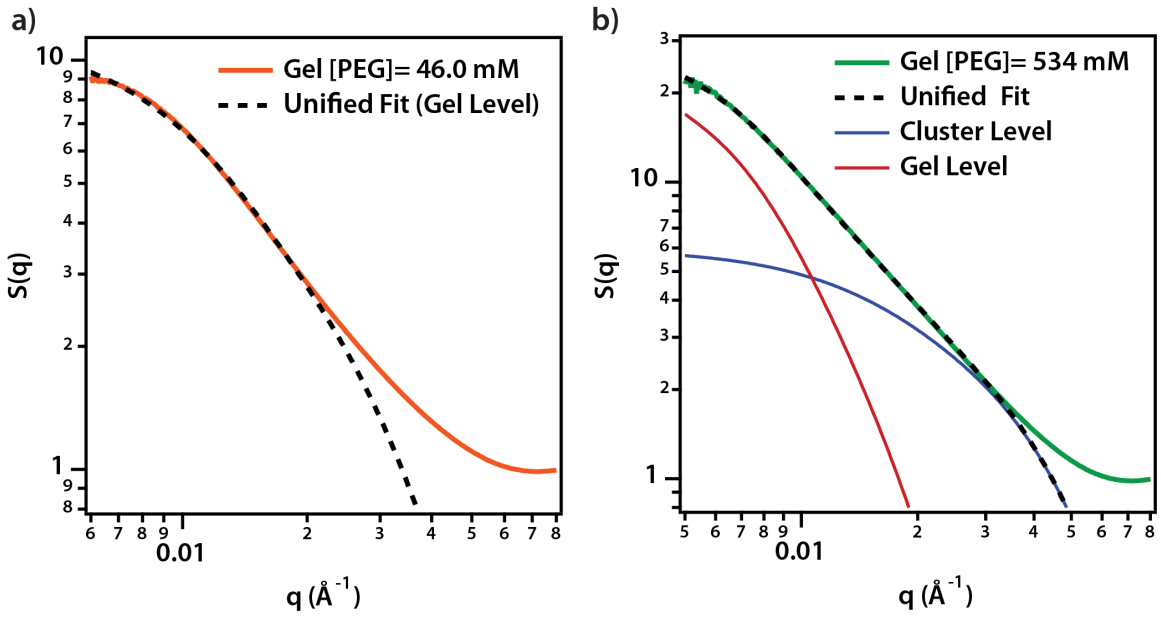

Figure 2.5: Unified fitting of ITO-PEG gels S(q).

a) Guinier and Porod unified fit of ITO-PEG gel ([PEG]= 46.0 mM) and b) two-level Guinier and Porod unified fit of ITO-PEG gel ([PEG]= 534 mM).

Table 2.1: Summary of SAXS unified fit results.

Parameters correspond to the fits shown in Figure 2.5. G and B are scaling coefficients in the unified function, R_g is the radius of gyration, and P is the Porod exponent. The parameters are defined and described in more detail in work by Beaucage.[112,114,117]

	Gel Level (Level 1)	
Gel [PEG]= 46.0 mM	G	11.6
	Rg [Å]	136
	B	8.52E-04
	P	2.20
	Rg cut off	29

	Cluster Level (Level 1)		Gel Level (Level 2)	
Gel [PEG]= 534 mM	G	5.98	G	48.3
	Rg [Å]	82.7	Rg [Å]	530
	B	0.006	B	4.60E-04
	P	1.85	P	2.09
	Rg cut off	29	Rg cut off	84

In the SAXS data of all [PEG], we observe the form factor of the discrete nanocrystal spheres, with fitting results yielding constituent particles with a radius of 2.95, 2.89, and 2.82 nm in the case of the lowest [PEG] dispersion, low [PEG] gel, and high [PEG] gel, respectively. This consistency suggests that the nanocrystals remain discrete under all PEG-induced assembly conditions. The persistence of the nanocrystals' morphology is further supported by high-resolution transmission electron microscopy imaging of a dried and diluted gel with [PEG] = 534 mM (Figure 2.6), where individual nanocrystals are discerned without apparent crystallographic continuity (i.e., oriented attachment) between them. Detecting a prevalent crystallographic orientation continuous between neighboring nanocrystals would suggest inter-nanocrystal fusion since metal oxides are known to fuse into extended nanostructures by oriented attachment.[118,119] Scherrer analysis of X-ray diffraction complements our observations by high-resolution transmission electron microscopy, where the crystallite size of discrete ligand-stripped nanocrystals (6.19 nm for the (222) peak) is found to be comparable to the nanocrystal size in the gel with [PEG]= 534 mM (5.89 nm for the (222) peak, Figure 2.7 and Table 2.2), both of which are in turn consistent with diameters measured by electron microscopy, SAXS, and dynamic light scattering. Preventing nanocrystal fusion throughout the assembly process is particularly advantageous for depletion gelation since the attraction strength can be weakened by reducing the depletant concentration relative to the primary particle and, in principle, reverse gelation. We achieved the disassembly of the ITO-PEG gel ([PEG]= 534 mM) by adding 600 μL of ITO-PEG flowing dispersion ([PEG]= 8.00 mM) to dilute [PEG] in the mixture by a factor of three at a fixed nanocrystal vol. %). A stable flowing dispersion is recovered by gentle manual agitation without using sonication or vortexing.

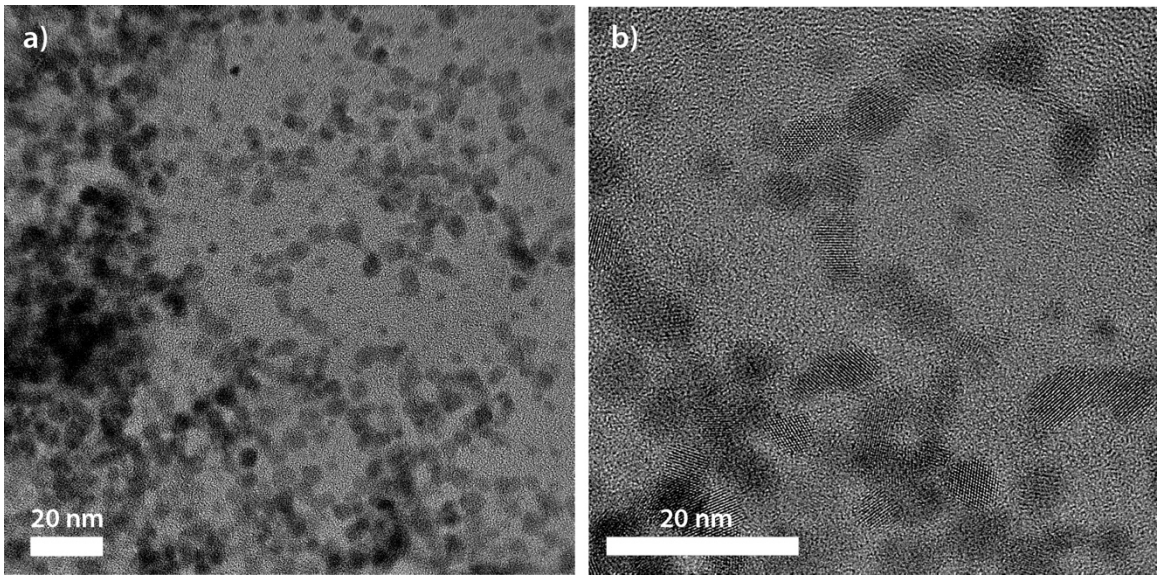

Figure 2.6: Transmission electron microscopy images of freeze-dried and diluted ITO-PEG gel ([PEG]= 534 mM).

a) Low magnification transmission electron microscopy image showing chains composed of discrete nanocrystals that do not exhibit a wire-like morphology characteristic of physical fusion during gelation. The nanocrystals exhibit various diffraction contrasts, meaning that bonding does not occur by oriented attachment, which is the preferred fusion mechanism in metal oxide networks and b) high resolution transmission electron microscopy image of the same area showing a curved chain of at least 10 discrete ITO nanocrystals exhibiting different crystal orientations without apparent crystallographic continuity between adjacent nanocrystals.

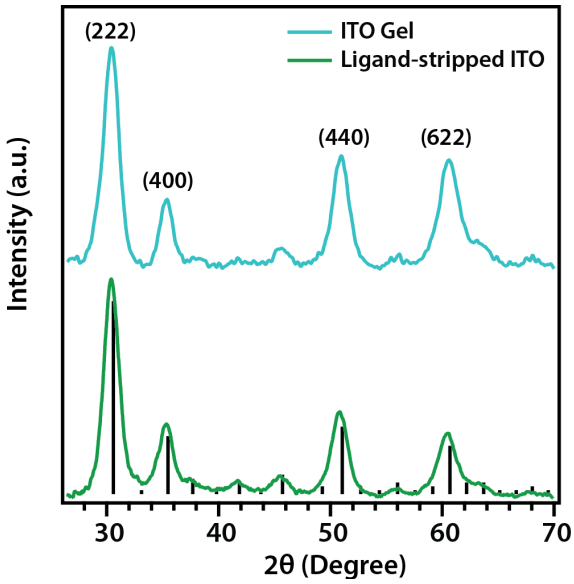

Figure 2.7: X-ray diffraction patterns of nanocrystals and gel.

Ligand-stripped nanocrystals (green) and nanocrystal gel ([PEG]= 534 mM, light blue). Indium oxide (In_2O_3) bixbyite reference pattern (PDF # 00-006-0416) is included at the bottom.

Table 2.2: Summary of Scherrer analysis results for the four most intense In_2O_3 diffraction peaks.

Crystallite sizes were calculated using the Scherrer equation $\tau = \frac{\lambda}{\beta \cos(\theta)}$, where τ is the crystallite size, λ is the X-ray wavelength (0.154 nm), β is the full-width at half-max (FWHM) of the diffraction peak in radians, and θ is the Bragg angle of the diffraction peak. β is corrected for instrumental broadening using $\beta = \sqrt{B_{exp}^2 - B_{LaB6}^2}$, where B_{exp} is the measured FWHM of the diffraction peak and B_{LaB6} is the FWHM of the lanthanum hexaboride standard.

(hkl)	Sample	2 theta (degrees)	Crystallite size (nm)
222	ITO gel	30.4	5.89
	ligand-stripped ITO	30.4	6.19
400	ITO gel	35.3	7.11
	ligand-stripped ITO	35.3	6.16
440	ITO gel	50.9	5.72
	ligand-stripped ITO	50.8	5.37
622	ITO gel	60.6	4.89
	ligand-stripped ITO	60.4	5.26

Considering the [PEG]-dependent phase progression including a reentrant regime, we hypothesized that gelation might be influenced by inter-nanocrystal attractions other than depletion-attractions. Specifically, we propose that, in addition to its depletant role, PEG can bridge adjacent ITO nanocrystals. Because PEG chains are known to preferentially adsorb on acidic oxide surfaces (the isoelectric point of the nanocrystals used in this work is between 4 and 5) via hydrogen bonding and subsequently aggregate oxide particles,[120-122] we deduce that low PEG concentrations (e.g., [PEG]= 46.0 mM) can favor bridging gelation. It is worth noting that PEG adsorption on the metal oxide surface does not hinder the internanocrystal long-range electrostatic repulsion necessary to form open depletion gels since dispersed ITO-PEG clusters still exhibit a strong positive zeta potential. In this light, prior work by Luo, Zhao, and co-workers[40,123] described an analogous experimental phase progression in a polystyrene microsphere system where bridging and depletant effects are both operative. They showed the emergence of the following phase transition sequence as the concentration of the smaller adsorbing species (poly(N-isopropylacrylamide)) in the system increases: bridging-induced aggregation → stabilization of discrete microspheres → depletion-induced aggregation. Moreover, they determined that since depletion-attraction interactions are only favored once the adsorbing molecules have saturated the colloidal surface and bridging attractions are hindered, the assembly mechanism (i.e., bridging or depletion) is highly sensitive to changes in the colloid-to-adsorbing molecule concentration ratios.

To assess our proposed mechanism for reentrant gelation in ITO-PEG dispersions, we devised a theoretical model that is unique in possessing a unified description of bridging and depletion effects. The free-energy theory synergistically combines a well-accepted theoretical treatment for the Asakura Oosawa model (depletion) with the accurate Wertheim theory for strong association (bridging). As detailed microstructural prediction is not our goal, simplification comes from approximating the stabilizing repulsions with hard-core interactions for the purposes of bulk thermodynamic calculations.[124,125] Various physical parameters enter the theory: the nanocrystal-to-polymer diameter ratio (d_{NC}/d_P),

the number of polymers that can adsorb onto the nanocrystal surface before saturation (n_{ads}), the number of nanocrystals that a single polymer chain can bridge (n_{bind}), and the polymer-nanocrystal thermal adsorption volume (v), which encapsulates the combined effects of adsorption energy, temperature and the spatial range of the attraction (more details are included in Appendix 1). To specifically model our nanocrystal gels, for d_{NC}/d_P we use the experimental value of ~ 3, and for n_{bind} we use the physically reasonable value of 2 based on the short PEG chains employed and nanocrystal size. For v and n_{ads} we explored various possibilities and the associated phase behavior, one example of which is shown in Figure 2.8 for n_{ads}=30 and v= 0.181 yielding a reentrant (liquid→gel→liquid→gel) phase diagram that is almost quantitatively in accord with the experimental results. Given our choices above for n_{ads} and n_{bind}, zero-temperature mean-field theoretical calculations[53] indicate that the bridging regime should not exceed a polymer-to-colloid ratio of 435 at any volume fraction or value of v. Therefore, the first spinodally unstable regime with increasing depletant is driven by nanocrystal-polymer bridging (which saturates upon surface coating) and the second by depletion. Importantly, the phase diagram is always qualitatively the same for physically reasonable values of n_{bind}: bridging gels form when the ratio of the number of polymers per nanocrystal is of order 10-100 and whereas of order 1000 is required for depletion—as seen in the experiments.

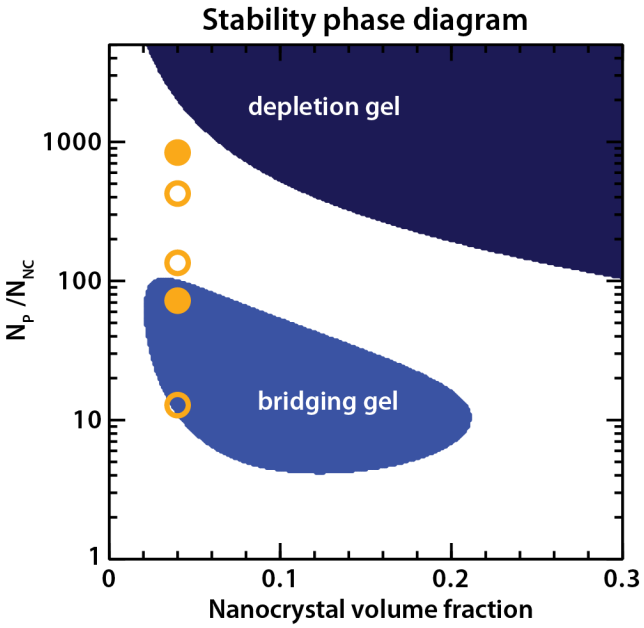

Figure 2.8: Comparison of theoretical model to experimental observations.

Theoretical phase diagram overlaid with experimental data points. N_P/N_{NC} denotes the ratio of number of polymers per nanocrystal. Open circles represent experimental flowing dispersions and closed circles represent experimental observation of gels. Regions where bridging and depletion gelation are predicted to occur are delimited by light and dark blue areas, respectively.

Our nanocrystal gels assembled via bridging and depletion interactions are optically active and exhibit an extinction spectrum reminiscent of that of the discrete nanocrystal building blocks. As shown in Figure 2.9, the LSPR peak of both the bridging ([PEG]= 46.0 mM) and depletion ([PEG]= 534 mM) gels is red-shifted (by 212 and 101 cm^{-1} for the bridging and depletion gel, respectively) from that of dispersed nanocrystals in acetonitrile. We attribute the similarity between these spectra to our successful preservation of the nanocrystal morphology as they are integrated in the gel network, avoiding ITO nanocrystal fusion by oriented attachment. The modest red-shift of both gel LSPRs, their reduced peak intensity, and significant broadening towards lower energies compared to the spectrum of isolated nanocrystals are all characteristic of LSPR coupling between nearest neighbors, as previously studied in extended assemblies, such as films, of colloidal metal

nanoparticles[126-128] and metal oxide nanocrystals.[10,129,130] Moreover, considering our gel structure analysis from SAXS, we hypothesized that the difference in LSPR peak broadening and shifting between the bridging and depletion gels is correlated to their structural differences. Since the depletion gel network is composed of discrete nanocrystal clusters, not detected in the bridging gel network, we expect the gel LSPR to be affected by variations in the nearest neighbor environment of nanocrystals.

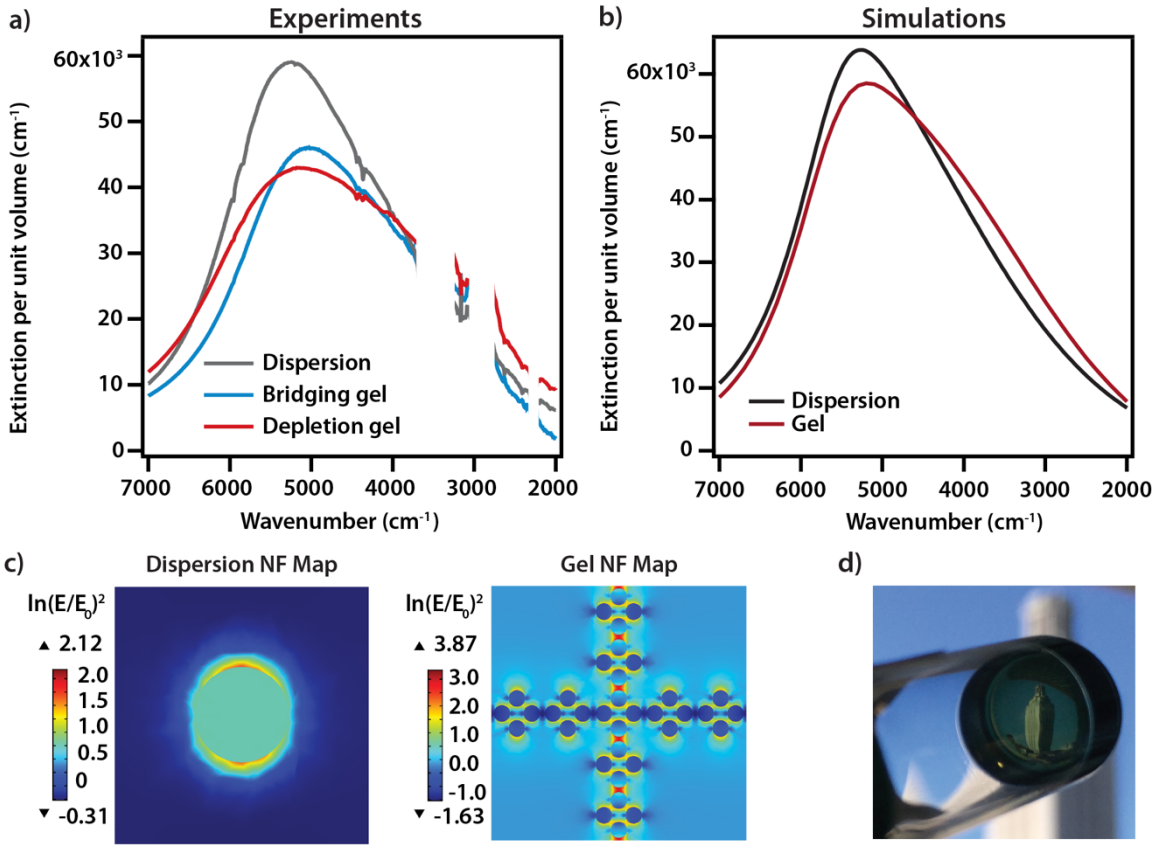

Figure 2.9: Experimental and simulated optical properties of ITO-PEG gels.

a) Experimental extinction spectra of depletion gel ([PEG]= 534 mM, red), bridging gel ([PEG]= 46.0 mM, blue), and ligand-stripped nanocrystal dispersion (grey), b) simulated extinction spectra of nanocrystal gel and ligand-stripped nanocrystal dispersion, c) simulated near-field (NF) maps of nanocrystal gel and ligand-stripped nanocrystal dispersion, and d) photograph of highly transparent nanocrystal depletion gel under natural lighting against the University of Texas Tower.

To investigate the influence of nanocrystal clustering on the gel's far-field optical properties and to anticipate near-field optical properties, we simulated the optical response of an extended network composed of PEG-coated ITO octahedral clusters (10 nm in radius) with a nanocrystal volume fraction of 3.88 vol. %, similar to that of the depletion gel studied experimentally (see Appendix 1 for more details). Although an idealized structural representation was used to ensure computational tractability, the simulated network was designed to approximate the experimentally measured nanocrystal volume fraction in the gel and the structural hierarchy ascertained from analysis of the SAXS data described earlier. As shown in Figure 2.9b, the simulated depletion gel LSPR does not precisely capture the features of the experimental depletion gel LSPR due to simulation limitations, mainly the size of the simulated box. Nonetheless, the simulated spectrum qualitatively reflects the LSPR characteristics of the bridging and depletion configurations, thus highlighting the optical sensitivity to LSPR-LSPR coupling facilitated by arranging ITO nanocrystal building blocks in close proximity in the gel network. Based on the simulations, we anticipated that such coupling effects should give rise to intense "hot spots" of greatly enhanced electric field intensity confined between nanocrystals in gel assemblies where the electromagnetic near-fields of neighboring constituents overlap. Simulated near-field maps shown in Figure 2.9c demonstrate the near-field enhancement under resonant optical excitation of the ITO nanocrystal gel network. Altogether, these findings support nanocrystal gel assemblies' potential to achieve highly tunable and complex plasmonic materials by leveraging the dependence of optical properties on the mesoscale arrangement of discrete nanocrystal building blocks. In addition, assembling closely spaced nanocrystals into a gel network allows generation of localized "hot spots", thereby providing coupling opportunities to other optical transitions relevant to surface enhanced infrared absorption spectroscopy and sensing applications[10,11,131] otherwise inaccessible in networks built from crystallographic junctions of fused nanocrystals.

CONCLUSIONS AND OUTLOOK

The strategy described here demonstrates the potential for tunable gels based on reversible physical bonds, and with responsive optical properties. A basic requirement for optical materials is that scattering does not interfere with the absorption, reflection, and luminescence properties of interest. Our depletion attraction strategy produces a highly transparent ITO nanocrystal gel that remains stable for over 1 year without developing haze noticeable to the eye (Figure 2.9d). Obtaining transparent self-supported nanocrystal gels has remained a challenge in the field since most established gelation methods give rise to fast-growing networks of large aggregates (scatterers) that ultimately form opaque gels. Instead, as alluded to earlier for our system, competing electrostatic repulsions and attractions (via bridging or depletion) favor slow bonding kinetics and thereby facilitate the formation of fractal aggregates with characteristic length scales smaller than the wavelength of visible light (R_g = 13.6 and 53.0 nm for bridging and depletion gel, respectively, Table 2.1). Our results are consistent with a previous study by Korala and Brock[72] on the aggregation kinetics of CdSe in which it was determined that simultaneously accessing the reaction-limited clustering aggregation regime and suppressing large scale aggregation are necessary conditions to induce transparency in a nanocrystal gel. Accordingly, gaining insight into the interplay between interparticle interactions, structure, and aggregation kinetics is key to rationalize and exploit the nanocrystal gel properties stemming from nanoscale building blocks.

More generally, we showed how the combination of depletion attractions and electrostatic repulsions can realize the assembly of nanocrystal gels. While the addition of PEG mediates attractions between dispersed nanocrystals, competing long-range electrostatic repulsions resulting from ligand stripping encourage the formation of a self-supported gel rather than a dense and collapsed material. We observed the emergence of two gelation windows interspaced with flowing dispersion states of discrete nanocrystal clusters. Transitioning from a flowing to a solid-like gel state was accompanied by a strong S(q) divergence and intensity increase at the lowest resolvable q, a characteristic of colloidal aggregation through spinodal decomposition reported in prior literature. In this

regard, our theoretical phase behavior predictions, based on a unified bridging and depletion attraction description that captured PEG's affinity for oxide surfaces and ability to bridge adjacent ITO nanocrystals, supported our experimental results and identified two spinodally unstable regions favoring bridging and depletion gelation at low and high [PEG], respectively. Moreover, we structurally differentiated the dominant assembly mechanism in each gel since we recognized two scattering length scales (nanocrystal < fractal gel) in the bridging gel as opposed to the three scattering length scales (nanocrystal < cluster < fractal gel) apparent in the depletion gel likely due to depletion attractions acting on pre-assembled clusters instead of discrete nanocrystals.

Our ITO nanocrystal model system was selected to investigate the gelation of charge-stabilized nanocrystals driven by depletion attractions, to experimentally demonstrate its feasibility, and to develop an adaptable gelation strategy that should in principle be broadly applicable across nanocrystal systems. For instance, other nanocrystal compositions with size and zeta potential similar to our nanocrystals are already available by established colloidal syntheses and represent the most immediate candidates to extend this work. Based on our analysis, depletant molecular weight may be varied to achieve similar assembly results with nanocrystals of different sizes. Also, as long as internanocrystal electrostatic repulsions are sufficient for colloidal stabilization, similar phase behavior is expected. Since bridging attractions between nanocrystals and depletants depend on surface chemical interactions, nanocrystal and depletant compositions can be strategically paired to tune bridging gelation or even suppress its emergence.

From an application perspective, we demonstrated optically active nanocrystal gels featuring LSPR representative of the nanocrystal building blocks by retaining their discrete morphology in the network, which has not been achieved with previously reported self-supported gel processing methods for plasmonic nanoparticles. By limiting the extent of aggregation, our gelation approach favored the formation of transparent gels, showing no signs of visible haze or scattering. In addition, we compared our optical spectra from experiments to electromagnetic simulations to highlight near-field enhancement opportunities generated by nearest-neighbor coupling effects in the gel network, a

promising feature that encourages further exploring nanocrystal gels as an alternative material for coupling applications. Finally, we envision that, extending our gelation approach to other nanocrystal systems could motivate further studies to improve our insight on structure-property relationships in assemblies to thus achieve systematic design of nanocrystal gel properties. We believe that our framework could also contribute to the development and diversification of multicomponent nanocrystal gels as a means to unlock even more complex nanocrystal gel functionality.

Chapter 3: Universal Gelation of Metal Oxide Nanocrystals via Depletion Attractions*

Nanocrystal gelation provides a powerful framework to translate nanoscale properties into bulk materials and to engineer emergent properties through the gel's assembled microstructure. However, many established gelation strategies rely on chemical reactions and specific interactions, e.g., stabilizing ligands or ions on the nanocrystals' surfaces, and are therefore not easily transferrable. Here, we report a general gelation strategy via non-specific and purely entropic depletion attractions applied to three types of metal oxide nanocrystals. The gelation thresholds of two compositionally distinct spherical nanocrystals agree quantitatively, demonstrating the adaptability of the approach for different chemistries. Consistent with theoretical phase behavior predictions, nanocrystal cubes form gels at a lower polymer concentration than nanocrystal spheres, allowing shape to serve as a handle to control gelation. These results suggest that the nature of depletion-driven assembly, traditionally associated with colloidal length and time scales, is unchanged at the nanoscale.

INTRODUCTION

Colloidal nanocrystals are functional building blocks that exhibit remarkable properties inherent to the nanoscale[1-4,59] and can be used to self-assemble structures over multiple length scales.[6] Considering the influence of the spatial arrangement of neighboring nanocrystals on nanoscale optoelectronic properties (e.g., localized surface plasmon resonance,[1,10-12] photoluminescence,[13-15] and photocatalysis[16-19]), self-assembly methods have become powerful tools to diversify and even enhance properties in

* This chapter has been adapted with permission from a manuscript in revision and submitted to arXiv preprint (arXiv:2003.11633), copyright © 2020. Written in collaboration with Zachary M. Sherman, Michael P. Howard, Manuel N. Dominguez, Shin Hum Cho, Gary K. Ong, Allison Green, Thomas M. Truskett, and Delia J. Milliron. C.A.S.C wrote the manuscript, conceived experiments, prepared nanocrystal dispersions and gel samples, and conducted electron microscopy, DLS, zeta potential, FTIR, and SAXS, characterization, and analyzed the data.

macroscopic materials and devices.[6] Among these methods, nanocrystal gelation assembles self-supported, open, and percolated networks and has gained significant interest in the past decade owing to its exceptional ability to translate and retain nanoscale properties in a bulk material compared to denser assemblies.[21-23] Nanocrystal gelation also offers structural control over multiple length scales. Both the local structure around an individual nanocrystal (e.g. volume fraction, valence, and interparticle distance) and the global topology of the network may be tuned by changing the physicochemical interactions of the building blocks.[53,54,72] Therefore, this framework presents opportunities for elucidating and designing structure-property relationships.

Nanocrystal gelation involves the controlled aggregation of colloidal dispersions and has been conventionally achieved by either removing the stabilizing ligands from the colloid surfaces or creating chemical bridges between the surface-bound ligands.[21,23,47,51,52] Although controlled ligand removal has been adapted for gelation of different types of nanocrystals and ligand combinations, precise structural control is frustrated by fast aggregation kinetics that typically lead to sedimented gels or sintering into continuous wire-like networks. Inducing controlled gelation using chemical linking is a viable strategy to circumvent these challenges, but this approach is limited to specific surface chemistries that are not easily adaptable across noble metals, metal chalcogenides, and metal oxides unless a suitable ligand exchange is found, or a new ligand-linker combination is designed. Recen efforts to generalize nanocrystal gelation leverage electrostatic interactions to mediate the assembly of different single-component and composite gels.[57,58] However, non-specific physical interactions remain largely unexplored in nanocrystal gel systems despite their potential to facilitate assembly of different nanocrystal sizes, complex shapes, hybrid nanocrystals, and combinations thereof.

Depletion attractions are physical and purely entropic forces that offer a general tunable strategy to assemble colloidal gels that does not depend on the composition and surface chemistry of the building blocks. In principle, the strength and range of attraction can be easily and independently controlled by changing the relative sizes of the primary colloid and the smaller cosolute (depletant) and/or the depletant concentration.

Experimental soft material systems such as polymer microspheres[109,132-135] and surfactant-stabilized emulsions[136] have leveraged the intrinsic versatility of depletion attractions to form gels with different colloids in the presence of the same depletant and vice versa, but this capability has not been demonstrated with inorganic materials, especially nanostructured ones. Moreover, the strategic selection of particle shape, which dictates the geometry of densest packing and therefore determines the magnitude of the overlap excluded volume, allows further control of the strength of attractions and imparts directionality to the interaction.[137-139] In particular, this shape-dependence has been used to selectively aggregate faceted particles in mixed dispersions and separate them from spherical particles.[137,138] While depletion-mediated superlattice assembly of microcubes,[140] nanoprisms,[141] and nanopolyhedra[142] has been studied, to our knowledge, gelation with faceted particles has not been reported before.

In this work, we demonstrate a universal approach to nanocrystal gelation using depletion attractions. We expand on a protocol that we developed previously[143] based on the combination of long-range electrostatic repulsions and polymer-mediated short-range depletion attractions. As a model system, we use metal oxide nanocrystals of similar size, but different compositions and shapes: iron oxide (FeO_x) spheres, tin-doped indium oxide ($Sn:In_2O_3$) spheres, and fluorine,tin-codoped indium oxide ($F,Sn:In_2O_3$) cubes. FeO_x, $Sn:In_2O_3$, and $F,Sn:In_2O_3$ gels were assembled by adding the same polyethylene glycol (PEG) depletant to charge-stabilized nanocrystal dispersions in acetonitrile. We assess our proposed gelation mechanism via PEG-induced depletion attractions and rationalize the phase behavior observed in all three systems with theoretical predictions of the phase behavior of the nanocrystal-depletant mixture. The gelation thresholds for $Sn:In_2O_3$ and FeO_x spheres are in quantitative agreement and do not depend on the nanocrystal composition. Consistent with calculated spinodal boundaries for spherical and cubic colloids, $F,Sn:In_2O_3$ nanocubes form a gel at a lower PEG concentration than $Sn:In_2O_3$ nanospheres. Small-angle X-ray scattering (SAXS) confirms that the gels form percolated networks that scatter as mass fractals. Samples prepared with lower PEG concentrations

remain flowing dispersions and appear by SAXS as dispersed nanocrystals with minimal clustering, as predicted theoretically

EXPERIMENTAL METHODS

Synthesis of Iron Oxide (FeO_x) Nanocrystals

FeO_x nanocrystals were synthesized in an inert environment using a standard Schlenk line technique by following an established colloidal method previously published in the literature.[144] Briefly, 1.325 g (15 mmol) of iron (III) oxide, 16.95 g (60 mmol) of oleic acid, and 37.5 g of octadecene were mixed in a round bottom flask and degassed for one hour at 120 °C. Then, the mixture was heated to 320 °C to reflux under nitrogen and left to react for one hour. Once the reaction flask was cooled to 70 °C, 20 mL of toluene were added to dilute the solution. To recover and purify the nanocrystals, the solution was transferred to centrifuge tube and centrifuged at 2000 rpm for five minutes. The dark precipitate was discarded while the supernatant was further purified by flocculating the nanocrystals with reagent alcohol (antisolvent), centrifuging at 7500 rpm for five minutes, and redispersing the resulting precipitate in hexane. This washing procedure was repeated two more times.

Synthesis of Tin-Doped Indium Oxide ($Sn:In_2O_3$) Nanocrystals

$Sn:In_2O_3$ nanocrystals were synthesized in an inert environment using a standard Schlenk line technique by following a continuous slow injection colloidal method previously published in the literature.[145] Briefly, 1.612 g (5.52 mmol) of indium (III) acetate, 170.34 mg (0.48 mmol) of tin (IV) acetate, and 7.5 mL of oleic acid were mixed in a round bottom flask and degassed at 100 °C under constant stirring for 20 min. Then, this precursor mixture was heated to 150 °C under nitrogen for two hours. During this step, the solution turned orange, which indicates the formation of indium oleate. In a separate round bottom flask, 13 mL of oleyl alcohol were degassed at 100 °C for two hours and subsequently ramped to 290 °C under nitrogen. 2.75 mL of indium oleate precursor were

then injected into the heated oleyl alcohol held at 290 °C at a rate of 0.2 mL/min. Nanocrystal growth was terminated by removing the heating mantle and cooling the reaction mixture by blowing air on the flask. To recover and purify the nanocrystals, the solution was precipitated with isopropyl alcohol (antisolvent) and centrifuged at 7500 rpm for five minutes. The supernatant was discarded and the resulting blue pellet was redispersed in hexane. This step was repeated four more times.

Synthesis of Fluorine, Tin-Codoped Indium Oxide (F,Sn:In_2O_3) Nanocrystals

F,Sn:In_2O_3 nanocrystals were synthesized in an inert environment using a standard Schlenk line technique by following a continuous slow injection colloidal method previously published in the literature.[146] Briefly, 1.387 g (4.75 mmol) of indium (III) acetate, 48.68 mg (5%, 0.25 mmol) of tin (IV) fluoride, and 10 mL of oleic acid were mixed in a round bottom flask in a nitrogen-filled glovebox. Next, the reaction flask was transferred to the Schlenk line and degassed at 120 °C for 15 min under constant stirring. 5 ml of this precursor solution were injected at a rate of 0.2 mL/min into another flask containing 13 mL of oleyl alcohol maintained at 290 °C, vented with a 19-gauge needle under constant nitrogen flow. Nanocrystal growth was terminated by removing the heating mantle and cooling the reaction mixture by blowing air on the flask. To recover and purify the nanocrystals, the solution was precipitated with isopropyl alcohol (antisolvent) and centrifuged at 7500 rpm for 10 minutes. The supernatant was discarded and the resulting pellet was redispersed in hexane. This step was repeated two more times. Then, the nanocrystal dispersion was centrifuged at 2000 rpm for three min to remove non-dispersible aggregates and the supernatant was collected as the final sample.

Ligand Stripping of FeO_x Nanocrystals

The native hydrophobic ligands bound to the surface of FeO_x were chemically removed by following a procedure reported previously.[100,108] Briefly, 60 mg of nitrosonium tetrafluoroborate were added to a two-phase mixture containing equal volumes of dimethylformamide (10 mL) and FeO_x nanocrystals dispersed in hexane (10 mg/ml, 10

mL) in a 20 mL vial. The mixture was swirled to allow nitrosonium tetrafluoroborate to react with the surface of FeO_x and then sonicated for 30 min. The process is complete when the dimethylformamide layer adopts a dark brown color and the hexane layer becomes pale orange, visibly indicating that the FeO_x nanocrystals have been transferred from the non-polar to the polar solvent. Next, the hexane layer was removed and replaced with 10 mL of neat hexane to further promote the removal of the ligands and wash the bare FeO_x nanocrystals. The mixture was sonicated for an additional 15 minutes. After discarding the hexane layer once more, the ligand-stripped FeO_x nanocrystals were purified by precipitating them with toluene (antisolvent), centrifuging at 7500 rpm for five minutes, and redispersing them in neat dimethylformamide. This step was repeated six more times. To disperse ligand-stripped FeO_x in acetonitrile, the colloid was precipitated and centrifuged once more and redispersed in neat acetonitrile or PEG in acetonitrile solution instead of dimethylformamide.

Ligand Stripping of Sn:In_2O_3 Nanocrystals

The native hydrophobic ligands bound to the surface of Sn:In_2O_3 were chemically removed by following a procedure reported previously.[100,143] Briefly, 60 mg of nitrosonium tetrafluoroborate were added to a two-phase mixture containing equal volumes of dimethylformamide (2 mL) and Sn:In_2O_3 nanocrystals dispersed in hexane (50 mg/ml, 2 mL) in a 20 mL vial. The mixture was swirled to allow nitrosonium tetrafluoroborate to react with the surface of Sn:In_2O_3 and then sonicated for 30 min. After adding 2 mL of neat hexane to further promote the removal of the ligands, the mixture was sonicated for an additional 15 minutes. The process is complete when the dimethylformamide layer adopts a transparent blue color and the hexane layer becomes clear, visibly indicating that the Sn:In_2O_3 nanocrystals have been transferred from the non-polar to the polar solvent. After discarding the hexane layer, the ligand-stripped Sn:In_2O_3 nanocrystals were purified by precipitating them with toluene (antisolvent), centrifuging at 7500 rpm for five minutes, and redispersing them in neat dimethylformamide. This step was repeated six more times. To disperse ligand-stripped Sn:In_2O_3 in acetonitrile, the colloid was precipitated and

centrifuged once more and redispersed in neat acetonitrile or PEG in acetonitrile solution instead of dimethylformamide.

Ligand Stripping of F,Sn:In_2O_3 Nanocrystals

The native hydrophobic ligands bound to the surface of F,Sn:In_2O_3 were chemically removed by following a procedure reported previously.[105,147] Briefly, F,Sn:In_2O_3 dispersed in toluene (20 mg/mL, 2 mL) were mixed with a triethyloxonium tetrafluoroborate (Meerwein's salt, 100 mg/mL, 2 mL) in anhydrous acetonitrile solution in a nitrogen glovebox. Upon adding the Meerwein's salt solution, the initially transparent F,Sn:In_2O_3 dispersion becomes a white and opaque solution. This mixture is stirred for 2 hours. Next, the white and opaque solution was transferred into a centrifuge tube and then centrifuged at 4500 rpm for five minutes. After discarding the supernatant, the nanocrystal pellet was dispersed in anhydrous dimethylformamide in the glovebox. Ligand-stripped F,Sn:In_2O_3 nanocrystals were further washed by precipitating with toluene, centrifuging at 7500 rpm for five minutes, and redispersing in anhydrous dimethylformamide. This process was repeated two more times and the nanocrystals were redispersed in anhydrous acetonitrile or PEG acetonitrile solution after the last centrifugation step. Ligand-stripping F,Sn:In_2O_3 with nitrosonium tetrafluoroborate resulted in nanocrystals that were partially dispersible at low concentrations and aggregated in dimethylformamide and not dispersible in acetonitrile.

Nanocrystal Gel Assembly

The assembly of FeO_x, Sn:In_2O_3, and F,Sn:In_2O_3 nanocrystal gels and flowing dispersions with PEG was adapted from a procedure that we developed recently.[143] Ligand-stripped nanocrystals (286 mg/mL for Sn:In_2O_3 and F,Sn:In_2O_3 and 200 mg/mL for FeO_x) were dispersed in a 2.26 mg/mL PEG in acetonitrile solution and stirred overnight. This nanocrystal-PEG dispersion is referred to as the stock solution. It is recommended to disperse the nanocrystals in neat acetonitrile or PEG in acetonitrile solution on the same day or the day after ligand-stripping since the nanocrystals won't be dispersible in

acetonitrile after being stored in dimethylformamide for a few days. To prepare samples of fixed ϕ_c and varying [PEG], different PEG amounts were added to 300 μL of the stock solution (Table 3.1). Once PEG was fully dissolved, small aliquots were injected into capillaries for SAXS measurements. Gels were formed after leaving the samples undisturbed for 48 hours (FeO_x and F,Sn:In_2O_3) and 7 days (Sn:In_2O_3).

The nanocrystal volume fraction of ϕ_c = 0.04 was estimated as $\phi_c = \frac{[NC]}{\rho_{NC}}$, where [NC] is the nanocrystal concentration and ρ_{NC} is the bulk density of the metal oxide (ρ = 7.14 g/mL for Sn:In_2O_3 and F,Sn:In_2O_3 and 5.07 g/mL for FeO_x). The depletant concentration [PEG], in mass per volume, is normalized by the polymer overlap concentration $[PEG]^* = 3M_n/(4\pi R_g^3 N_A)$, where $M_n = 1100$ g/mol is the polymer molecular weight, $R_g = 0.98$ nm [106,143]is the polymer radius of gyration, and N_A is Avogadro's number.

Table 3.1. Summary of different quantities used to prepare nanocrystal-PEG mixtures

Nanocrystal	m_{PEG} (mg)	[PEG] (mg/mL)	[PEG]/[PEG]*	State
FeO_x or Sn:In_2O_3	290	967	2.09	Gel
	105	351	0.758	Flowing dispersion
	26.4	87.9	0.190	Flowing dispersion
	0.68	2.26	0.005	Flowing dispersion
F,Sn:In_2O_3	105	351	0.758	Gel
	0.68	2.26	0.005	Flowing dispersion

Small-angle X-ray Scattering

SAXS measurements were performed in transmission configuration with a sample-to-detector distance of 1.085 m on a SAXSLAB Ganesha instrument using Cu Kα radiation. Dilute nanocrystal dispersions, nanocrystal-PEG flowing dispersions, and nanocrystal-PEG gels were enclosed in flame-sealed glass capillaries (Charles-Supper Company, Boron Rich, 1.5 mm diameter, 0.01 mm wall thickness). A capillary containing neat acetonitrile was used for background subtraction. Scattering patterns were calibrated using a silver behenate standard[101] and were converted into 1D data by circular averaging

using the Igor Pro-based Nika[102] software for two-dimensional data reduction. The Irena[103] tool suite for modeling and analysis in Igor Pro was used for background subtraction and for fitting the nanocrystal form factor following a procedure described in a previous publication.[51] More details on SAXS data analysis are reported in Appendix 2.

Electron Microscopy

Electron microscopy was performed on a Hitachi S5500 SEM/STEM instrument. Nanocrystals were imaged in bright-field scanning transmission electron (STEM) mode at a 30 kV accelerating voltage. Samples were drop-cast on Type-A ultrathin carbon copper TEM grids (Ted Pella, 01822, 400 mesh) from dilute nanocrystal dispersions in hexane.

Fourier Transform Infrared Spectroscopy

FTIR spectroscopy was carried out in transmission geometry with a 4 cm^{-1} resolution and an average of 120 scans on a Bruker Vertex 70 spectrometer. Dilute dispersions (~ 1 mg/mL) of as-synthesized and ligand-stripped FeO_x, $Sn:In_2O_3$, and F, $Sn:In_2O_3$ nanocrystals were dropcast onto undoped, double side polished silicon substrates (Virginia Semiconductor). Ligand-stripped nanocrystal films were annealed at 200 °C under inert atmosphere for at least 12 hours to remove any residual dimethylformamide from the sample. A neat silicon substrate was used for background subtraction. The substrates were cleaned by sonicating them in chloroform, acetone, and finally isopropanol for at least 30 minutes prior to dropcasting the nanocrystal films.

Zeta Potential

Zeta potential measurements were conducted in a Malvern Zetasizer Nano ZS. Dilute dispersions (~ 1 mg/mL) of ligand-stripped FeO_x, $Sn:In_2O_3$, and F, $Sn:In_2O_3$ nanocrystals were filtered through a polytetrafluoroethylene membrane (0.45 μm pore size, PALL) and transferred to a glass cuvette. Zeta potential values were collected by electrophoresis using an immersed dip cell (ZEN1002, Malvern).

RESULTS AND DISCUSSION

FeO_x, $Sn:In_2O_3$, and $F,Sn:In_2O_3$ nanocrystals of uniform size and shape (Figure 3.1a-c) were synthesized using established colloidal methods. The native, hydrophobic oleate ligands on the surface of the metal oxides were chemically removed using tetrafluoroborate salts[100,105] to produce charge-stabilized nanocrystal dispersions in polar solvents. Fourier transform infrared spectroscopy of the resulting nanocrystal dispersions shows the disappearance of the characteristic $-CH_2$ stretches from oleate, which is indicative of effective ligand removal (Figure 3.2). Zeta potential measurements confirm that long-range electrostatic repulsions originating from the metal oxide surface stabilize the nanocrystals (ζ = +38, +41, and +42 mV for FeO_x, $Sn:In_2O_3$, and $F,Sn:In_2O_3$, respectively, Figure 3.3). We use SAXS to probe the colloidal stability of these dispersions and find that they scatter as dilute and stable individual spheres and cubes (Figure 3.1d-f). We attribute the slight deviations in the low q scattering, relative to the simulated form factors, to weak interparticle interactions.[148] Suppressing aggregation in the initial dispersion, before adding depletion attractions, is crucial to avoid introducing uncontrolled structures that would ultimately be convoluted with longer length scale structures formed by depletion-induced assembly. In addition, the average nanocrystal size and size distribution were estimated by fitting the SAXS of the dispersions: the radii of FeO_x and $Sn:In_2O_3$ spheres are 4.63 ± 0.16 nm and 5.34 ± 0.48 nm, respectively, while the half edge length of $F,Sn:In_2O_3$ cubes is 4.36 ± 0.45 nm. Because the nanocrystals are of similar and uniform size, the same depletant can be used to induce attractions with an approximately equal range relative to the size of the nanocrystal.

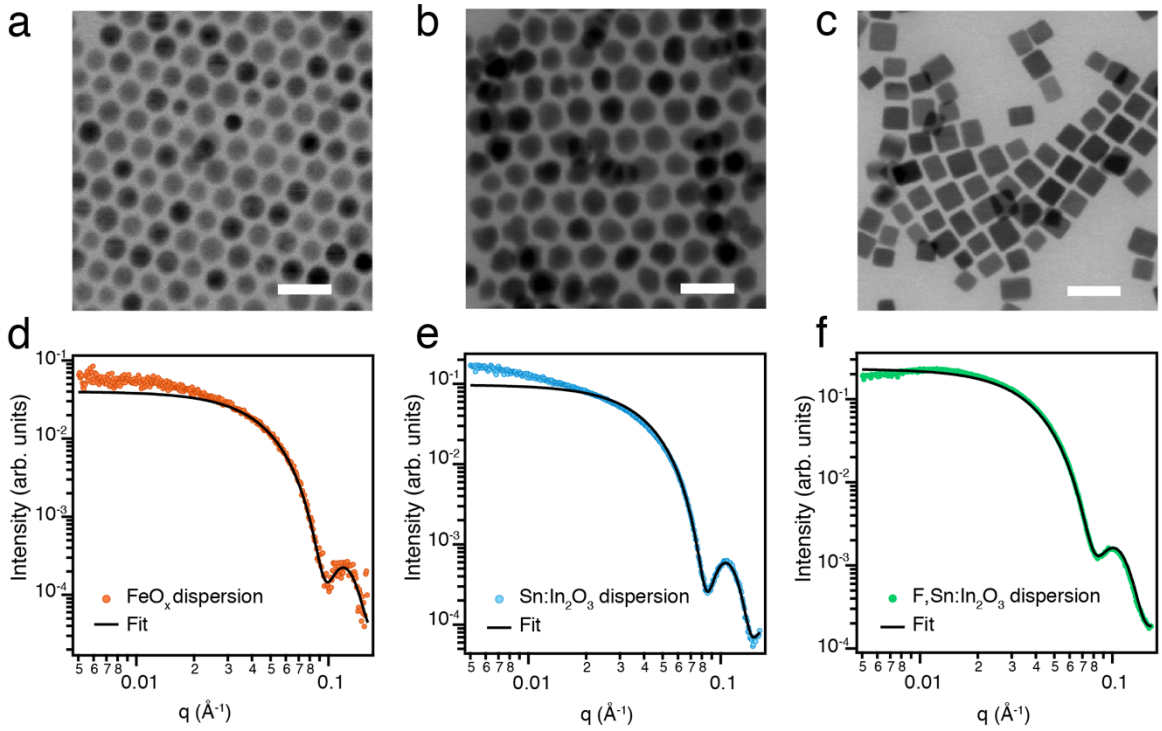

Figure 3.1: Morphology, size, and colloidal stability of nanocrystals.

Scanning transmission electron microscopy (STEM) image of as-synthesized a) FeO_x, b) $Sn:In_2O_3$, c) and $F,Sn:In_2O_3$ nanocrystals. Scale bar = 20 nm. SAXS of dilute (~1 mg/mL) charge-stabilized nanocrystal dispersions in acetonitrile: d) FeO_x and spheroid model fit (R = 4.63 ± 0.16 nm), e) $Sn:In_2O_3$ and spheroid model fit (R = 5.34 ± 0.48 nm), and f) $F,Sn:In_2O_3$ and cuboid model fit (L = 4.36 ± 0.45 nm). R is the radius of a sphere and L is half the edge length of a cube.

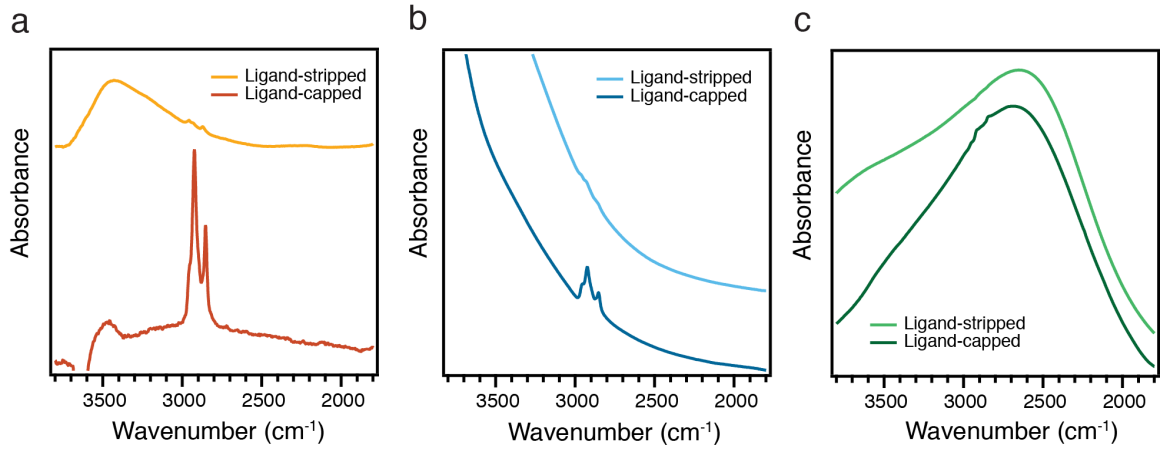

Figure 3.2: FTIR of nanocrystal before and after ligand-stripping.

a) Ligand-capped (orange) and ligand-stripped (yellow) FeO_x nanocrystals, b) ligand-capped (dark blue) and ligand-stripped (light blue) $Sn:In_2O_3$ nanocrystals, and c) ligand-capped (dark green) and ligand-stripped (light green) $F,Sn:In_2O_3$ nanocrystals. Disappearance of $-CH_2$ stretches (2925 and 2854 cm^{-1}) from oleic acid[104] in the ligand-stripped spectra indicate effective ligand removal. The sloping profile in the $Sn:In_2O_3$ nanocrystal spectra and intense peak at ~ 2700 cm^{-1} in the $F,Sn:In_2O_3$ nanocrystal spectra correspond to the localized surface plasmon resonance.

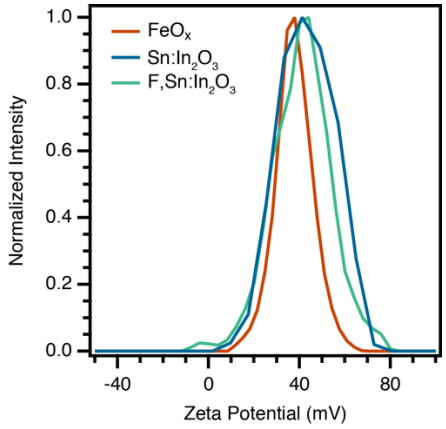

Figure 3.3: Zeta potential of ligand-stripped nanocrystal dispersions.

Zeta potential of ligand-stripped FeO_x (ζ = +38 mV, orange), $Sn:In_2O_3$ (ζ = +41 mV, blue), and $F,Sn:In_2O_3$ (ζ = +42 mV, green) nanocrystal dispersions.

Depletion gels were formed by adding PEG depletant (1 kDa number average molecular weight M_n, radius of gyration R_g = 0.98 nm[106,143]) to dispersions in acetonitrile at a fixed nanocrystal volume fraction (ϕ_c = 0.04). We recently showed that PEG having this M_n effectively drives the gelation of Sn:In_2O_3 nanocrystal spheres (R = 2.83 nm, ϕ_c = 0.04) dispersed in acetonitrile at a PEG concentration ([PEG]) of 587 mg/mL. In this sutyd, the size ratio of depletant to nanocrystal is smaller by nearly a factor of 2, which shortens the effective length scale and lowers the strength of the depletion attractions. Therefore, gelation occurs at higher [PEG]: 967 mg/mL for FeO_x and Sn:In_2O_3, respectively (insets in Figure 3.4). F,Sn:In_2O_3 cubes gel at a lower [PEG] (351 mg/mL), which we attribute to their ability to pack face-to-face, leading to larger overlap excluded volumes and therefore stronger depletion attractions compared to the spheres. Mixing the nanocrystals with lower [PEG] resulted in stable flowing dispersions (Table 3.1). Likewise, a solution of pure PEG in acetonitrile at the equivalent concentration used to induce gelation remained transparent and did not show signs of precipitation (Appendix 2), suggesting that gelation arises due to PEG-mediated attractions between nanocrystals.

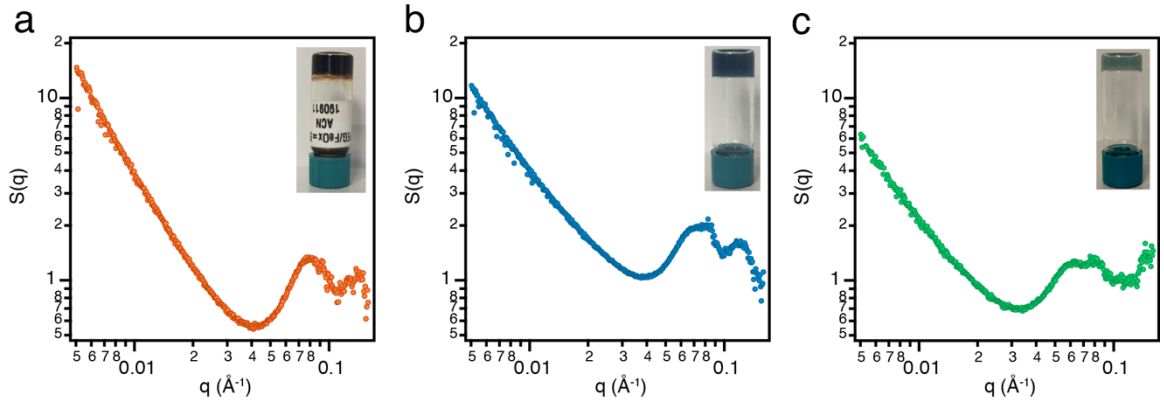

Figure 3.4: Structure factor of depletion gels.
S(q) of nanocrystal gels with photographs of the corresponding vials (insets) for a) FeO_x, b) Sn:In_2O_3, and c) F,Sn:In_2O_3 nanocrystals.

The gel structure was probed with SAXS to confirm the assembly of fully percolated networks (Figure 3.4). In particular, we isolate the structure factors S(q) of the

gels by dividing the total scattering intensity by the form factors of the corresponding nanocrystals (Appendix 2). S(q) diverges as q approaches zero for all samples and seems to follow a power law scaling characteristic of scattering from a mass fractal object.[41,113] To validate this observation and determine the number of structural length scales in the networks, we performed a derivative analysis (Figure 3.5). We find that each of the three gels scatters as a mass fractal with a single characteristic length scale. This single length scale suggests that the gel networks are formed as a result of depletion attractions between discrete nanocrystals, rather than depletion attractions between clusters of bridged nanocrystals as found previously for smaller $Sn:In_2O_3$ nanocrystals.[143] The fractal dimensions of the networks can be extracted from power law fits to S(q) in the region $q < 0.03$ $Å^{-1}$ (Figure 3.6). We obtained fractal dimensions of 2.0 for a FeO_x nanocrystal gel and 1.7 for $Sn:In_2O_3$ and $F,Sn:In_2O_3$ nanocrystal gels, all of which fall within the range of fractal dimensions reported in the literature for percolated colloidal gels.[73,143,149,150] We also notice oscillatory features in S(q) at high q reminiscent of those that originate from hard sphere or sticky hard sphere interactions.[20,151,152] The primary peak appears at q = 0.078, 0.074, and 0.062 $Å^{-1}$, for FeO_x, $Sn:In_2O_3$, and $F,Sn:In_2O_3$ gels, respectively. These q values approximately correspond to the center-to-center distance of two adjacent nanocrystals (d= 8.05, 8.45, and 10.1 nm, respectively), which is consistent with the characteristic length scale for locally dense packing between nanocrystals in the gel.

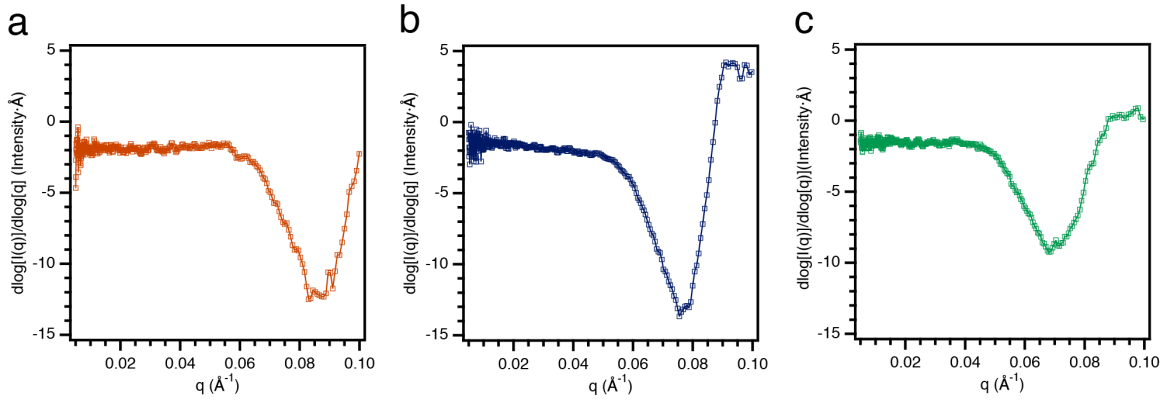

Figure 3.5: Identification of Porod regions by derivative analysis.

Analysis of gels composed of a) FeO_x, b) $Sn:In_2O_3$, and c) $F,Sn:In_2O_3$ nanocrystals. In the Porod region, the total scattering intensity $I(q) \propto q^{-P}$, where P is the Porod exponent and reflects the dimensionality of the scattering object or assembly. Therefore, when dlog[I(q)]/dlog[q] is plotted with respect to q, the Porod region appears as a line of zero slope that intersects the y axis at a value equal to -P. The I(q) data corresponding to FeO_x, $Sn:In_2O_3$, and $F,Sn:In_2O_3$ nanocrystal gels shown in Appendix 2 were used for this analysis. The derivative plots reveal that the scattering pattern of each of the three gels is composed of a single Porod region (i.e., only one characteristic length scale). The onset of the Porod region approximately occurs $q < 0.03$ Å^{-1}.

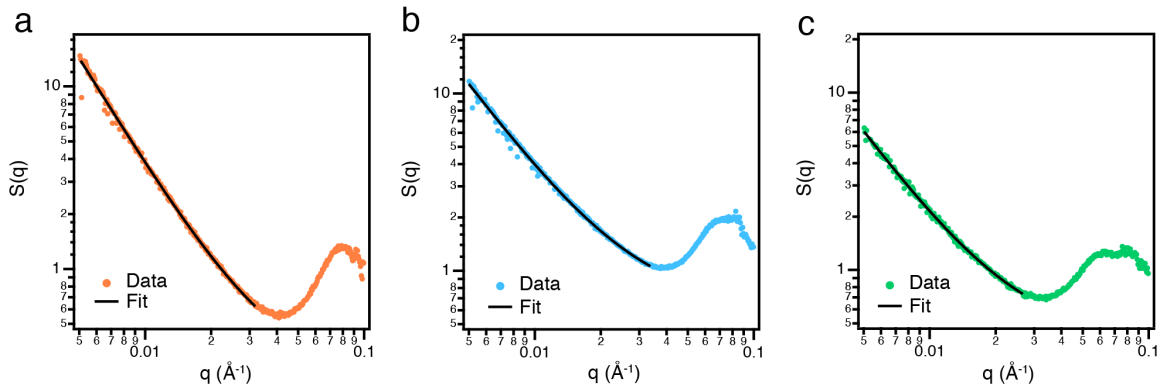

Figure 3.6: Power law fits of Porod region.

S(q) of gels composed of a) FeO_x ($D_f = 2.0$), b) $Sn:In_2O_3$ ($D_f = 1.7$), and c) $F,Sn:In_2O_3$ ($D_f = 1.7$) nanocrystals. For a mass fractal composed of a single structural level, $S(q) \propto q^{-P}$, where $D_f = -P$ is the fractal dimension. The upper and lower q limits for the fits were selected based on the derivative analysis (Figure 3.5).

To assess our proposed mechanism of depletion-driven gelation and better understand the influence of nanocrystal shape on the gelation threshold, we compare theoretical predictions for the phase behavior of the nanocrystal-depletant mixture to our experimental observations. Phase diagrams incorporating depletion attractions for both spherical[35] and cubic[153] nanocrystals can be computed using free volume theory and scaled particle theory to determine the spinodal boundaries. Details of these calculations are found in Appendix 2. At [PEG] above the spinodal curve, a homogeneous dispersed phase of nanocrystals is mechanically unstable with respect to fluctuations in nanocrystal concentration, and the dispersion undergoes phase separation via spinodal decomposition. Because of the strong interparticle depletion forces, the nanocrystals typically arrest in percolated networks,[109] so the spinodal boundary is the relevant one to compare with gelation in the experiments.[143] For both the sphere and the cube systems, we see good agreement between the predicted and experimental phase boundaries as a function of nanocrystal volume fraction (ϕ_c) and [PEG] normalized by the polymer overlap concentration $[PEG]^*$ (Figure 3.7, Appendix 2 for wider ϕ_c and [PEG] ranges, and Figure 3.8 for the FeO_x nanocrystal spheres). Specifically, the nanocrystal gels lie at [PEG] above the spinodal, where gelation is expected, while the nanocrystal dispersions that remain flowing lie below the spinodal. Moreover, the phase diagrams clearly show that the gelation threshold is expected to occur at significantly lower [PEG] for the cubes compared to the spheres at all ϕ_c due to stronger depletion forces between flat surfaces compared to curved surfaces. This is confirmed in the experiments, where the $Sn:In_2O_3$ nanospheres remain flowing at $[PEG]/[PEG]^* = 0.758$ while the $F,Sn:In_2O_3$ nanocubes gel.

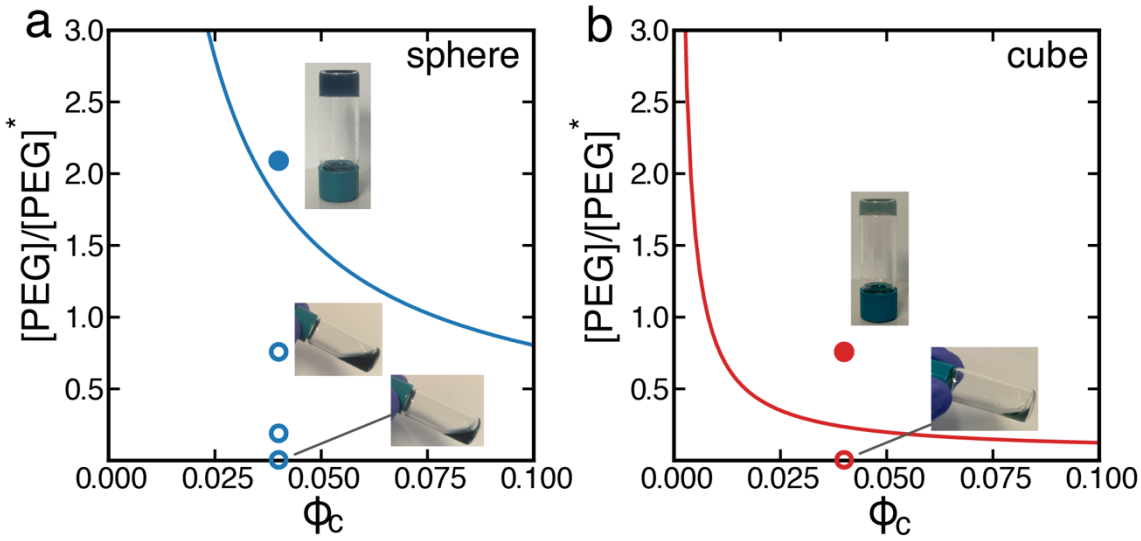

Figure 3.7: Comparison of predicted phase behavior and experiments.

Theoretical spinodal boundaries (lines) and experimental observations (points) for a) Sn:In_2O_3 nanocrystal spheres and b) F,Sn:In_2O_3 nanocrystal cubes. The nanocrystal volume fraction is denoted by ϕ_C, and the free polymer mass concentration [PEG] is normalized by the overlap concentration $[PEG]^* = 3M_n/(4\pi R_g^3 N_A)$, where M_n is the polymer molecular weight, R_g is the polymer radius of gyration, and N_A is Avogadro's number. Open circles represent flowing dispersion samples while filled circles represent gel samples.

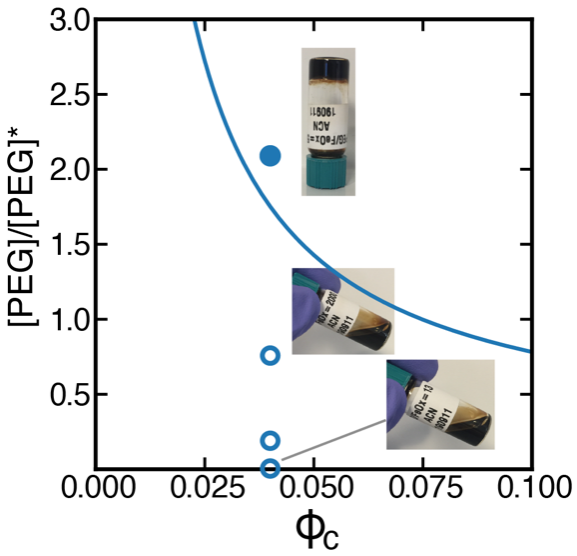

Figure 3.8: Theoretical spinodal boundary (line) and experimental observations (points) for FeO_x nanocrystal spheres.

Open circles represent flowing dispersion samples while filled circles represent gel samples.

Depletion attractions were sufficient to account for the observed phase behavior of the nanocrystal dispersions, distinct from our previous work, where bridging of nanocrystals by PEG was observed to induce gelation at low [PEG]. For the nanocrystals studied here, monitoring the time evolution of S(q) for low [PEG] samples revealed only limited aggregation and no evidence for extended network formation, and the dispersions remained readily flowing even after several weeks (Figure 3.9 and Appendix 2). Although PEG adsorption on the metal oxides persists, PEG-mediated bridging attractions are significantly weaker, likely due to size constraints and smaller nanocrystal surface-to-volume ratios. In fact, we detect minimal clustering in all flowing dispersions. Aggregate sizes are only on the order of two adjacent nanocrystals (d = 19, 23, and 22 nm for FeO_x, Sn:In_2O_3, and F,Sn:In_2O_3, respectively) and do not grow significantly until after four weeks (Appendix 2). We note that S(q) of the gels appears unchanged indicating the gel structures are not significantly changed by aging on this time scale.

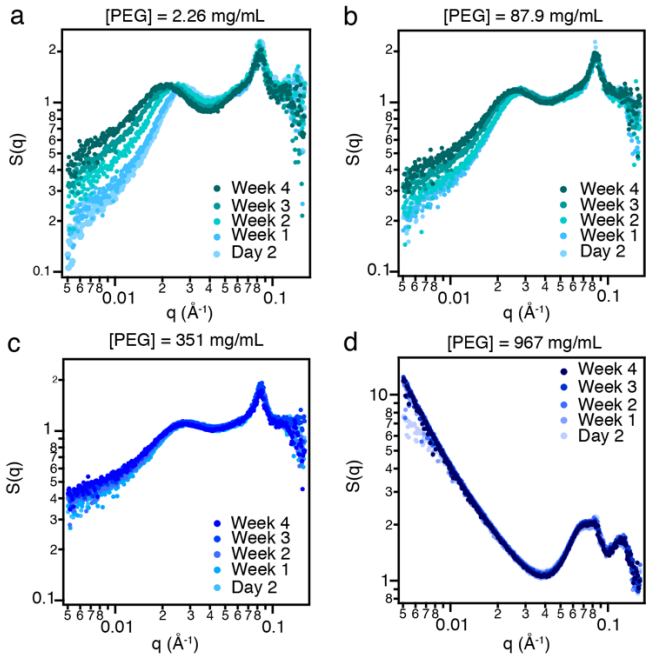

Figure 3.9: Evolution of structure factor S(q) of Sn:In_2O_3 nanocrystal-PEG mixtures over 4 weeks.

a) Flowing dispersion ([PEG]= 2.26 mg/mL, [PEG]/[PEG]*= 0.005), b) flowing dispersion ([PEG]= 87.9 mg/mL, [PEG]/[PEG]*= 0.190), c) flowing dispersion ([PEG]= 351 mg/mL, [PEG]/[PEG]*= 0.758), and d) gel ([PEG]= 967 mg/mL, [PEG]/[PEG]*= 2.09). The broad peaks around $q < 0.03$ Å^{-1} in the flowing dispersions indicate the presence of small aggregates. The sharp peak at $q \sim 0.08$ Å^{-1} ($d = 7.8$ nm) is likely due to Sn:In_2O_3 nanocrystals attaching to each other before PEG adsorbs on their surface since ligand-stripped nanocrystals are more prone to aggregate at such high concentration ($\phi_c = 0.04$ or [Sn:In_2O_3] = 286 mg/mL). The fact that this peak is present at all [PEG] and does not evolve over time further supports this assertion.

CONCLUSIONS AND OUTLOOK

In conclusion, we have demonstrated a gelation strategy broadly applicable to metal oxide nanocrystals. Nanocrystals of similar sizes, but different compositions and shapes, were assembled using the same PEG depletant and solvent combination. As expected, FeO_x and Sn:In_2O_3 nanocrystal spheres formed gels at the same [PEG] while F,Sn:In_2O_3 nanocrystal cubes formed gels at a lower [PEG] due to the influence of shape on the strength of depletion attractions. Gel structure was characterized with SAXS, and our

experimental observations were found to be consistent with depletion-driven gelation by comparison to theoretically predicted phase behavior. We also showed evidence supporting the assembly of discrete nanocrystals rather than assembly of clusters of nanocrystals due to the excellent colloidal stability of our initial dispersions and the suppression of competing bridging attractions during the timeframe of gelation. Limiting nanocrystal aggregation, prior to the onset of depletion attractions, allows systematic control over the characteristic length scales of the microstructure in the gel. Finally, our findings motivate using depletion attractions to explore the connection between the gelation mechanism, the gel microstructure, and emergent properties. This work demonstrates the tunability and versatility of depletion attractions for nanocrystal assembly and provides a guide to expand the range of building blocks that can be used to incorporate targeted optical, electronic, or catalytic functionality in nanocrystal gels. Although varying nanocrystal composition and shape was our primary focus, within the paradigm described here, gels could be developed that utilize customized depletants among a wide variety of candidates (molecules, polymers, nanocrystals, etc), including ones that are stimuli responsive.

Chapter 4: Aqueous Processing and Spray Deposition of Polymer-Wrapped Tin-Doped Indium Oxide Nanocrystals as Electrochromic Thin Films*

Plasmonic metal oxide nanocrystals are interesting electrochromic materials because they display high modulation of infrared light, fast switching kinetics, and durability. Nanocrystals facilitate solution-based and high-throughput deposition, but typically require handling hazardous non-aqueous solvents and further processing of the as-deposited film with energy-intensive or chemical treatments. We report on a method to produce aqueous dispersions of tin-doped indium oxide (ITO) by re-functionalizing the nanocrystal surface, previously stripped of its native hydrophobic ligands, with a hydrophilic polymer (PAA-mPEO$_4$). To determine conditions favoring the adsorption of polymer on ITO, we varied the pH and chemical species present in the exchange solution. The extent of polymer wrapping on the nanocrystal surface can be tuned as a function of the pH to prevent aggregation in solution and deposit uniform, smooth, and optical quality spray coated thin films. We demonstrate the utility of polymer-wrapped ITO nanocrystal thin films as an electrochromic material and achieve fast, stable, and reversible near-infrared modulation without the need to remove the polymer after deposition provided that a wrapping density of at most 22 % relative mass is not exceeded.

INTRODUCTION

Among transparent conducting oxides, tin-doped indium oxide (ITO) nanocrystals have attracted considerable interest over the last decade as a dynamic electrochromic material for next-generation smart windows.[63,65,154-159] Owing to their localized surface plasmon resonance (LSPR) and low carrier concentration (~10^{20}-10^{21} cm^{-3}), ITO nanocrystals strongly absorb near-infrared (NIR) wavelengths of light between 1500 and

* This chapter has been adapted with permission from a manuscript in preparation written in collaboration with Anthony Maho, Kendall A. Meyertons, Lauren C. Reimnitz, Brett Helms, and Delia J. Milliron. C.A.S.C. wrote the manuscript, conceived experiments, prepared polymer-wrapped ITO dispersions, and conducted SEM, DLS, FTIR, TGA, and profilometer characterizations, and analyzed the data.

2000 nm. This optical response can be significantly tuned as a function of the nanostructure of the material. Colloidal synthesis methods allow to customize the strength and range of NIR modulation as a function of size, shape, and concentration and distribution of tin dopants,[1,99,145,146] while reversible electrochemical doping by subjecting ITO nanocrystals to an external bias achieves greater shifts in absorption intensity and frequency.[63,155,159,160] Moreover, the capacitive nature of electrochemical charging in ITO, as opposed to intercalative charging, leads to exceptional NIR electrochromic performance including fast switching kinetics, high coloration efficiency, and extended cycling stability compared to conventional bulk metal oxides.[63,65,155]

Nanocrystal dispersions are suitable for lower cost, high throughput, and more energy efficient solution processing methods for thin films. Additional advantages of wet depositions[63,65,161] that do not rely on high temperatures and ultra-high vacuum include compatibility with diverse substrates, especially flexible ones, and the fabrication of homogeneous composites with precise compositional control of the different elements. However, the deposition of nanocrystal thin films is typically achieved from non-aqueous, hazardous, and flammable solvents. Specifically, as-synthesized nanocrystals are stabilized by hydrophobic organic ligands and are therefore deposited from polar solvents (e.g., toluene, hexane, octane, etc).[98,99,145] Because these insulating organic ligands obstruct electronic conductivity across the thin film and intimate contact with the electrolyte in devices, either harsh thermal or chemical post-deposition treatments[162] (high temperature annealing and/or soaking in acidic/alkaline solutions), or the removal of ligands in solution before deposition using tetrafluoroborate salts,[100,105] are needed. The latter yields nanocrystals dispersions in polar solvents such as various formamides, dimethyl sulfoxide, and acetonitrile, but this procedure is not suitable for directly dispersing ITO in aqueous media or mixtures of water and alcohol. Within this context, there is a clear need to diversify the solvent compatibility of inorganic nanocrystals and develop methods to handle ITO and other metal oxides in water and solvents of low toxicity in general. This is particularly relevant to deposition techniques that involve large quantities of vapor effluents such as spray coating,[159,163] which is one of the leading candidates for the

economically scalable and high throughput fabrication of optical quality nanocrystal thin films.

So far, the primary strategy to disperse nanocrystals in aqueous solvent is to functionalize their surface with hydrophilic molecules. To this end, two approaches have mostly been explored: ligand exchange with inorganic oxoanions and polyoxometalates, [164,165] and with polymers and other organic molecules.[166-169] First, stabilizing semiconductor nanocrystals with inorganic ligands grants conductive pathways to the film along with circumventing post-deposition ligand removal and conferring additional properties to the composite. In particular, aqueous dispersions of ITO nanocrystals functionalized with polyoxoniobates enabled the direct deposition of homogeneous and tunable NbO_x glass-ITO composites that displayed selective and dual-band (visible and infrared) electrochromic modulation.[170,171] Nevertheless, this precursor dispersion is strongly alkaline, which is not necessarily suitable for all applications and composite assemblies, and converting the polyoxoniobate matrix into NbO_x requires additional treatment such as high temperature annealing or dipping the composite in an acidic solution. On the other hand, polymer-wrapping metal oxide nanocrystals and dispersing them in aqueous solutions remains largely unexplored, possibility due to challenges related to finding a polymer that adsorbs on the metal oxide surface without restricting the electron transport. Notably, Mendelsberg and coworkers[167] demonstrated that ligand-stripped ITO nanocrystals wrapped with the diblock copolymer poly(ethylene oxide)-b-poly(N,N-dimethylacrylamide) (PEO-b-PDMA) can be dispersed in water and undergo redox reactions with chemical species in solution. The polymer was designed to adsorb on the bare ITO surface (PDMA block) and provide steric stabilization and water solubility (PEO block). Likewise, metal oxides can also be functionalized with a random copolymer of poly(acrylic acid) grafted with methoxy-terminated poly(ethylene oxide) (PAA-$mPEO_4$), [166] but to the best of our knowledge this polymer has not been used to functionalize ITO. Beyond their hydrophilic and biocompatible properties, PEO-functionalized ITO nanocrystals could potentially be integrated into electrochromic devices, without the need for additional processing steps to remove the organic layer, due to the Li^+ transport

properties of the PEO moieties.[172-174] However, more rigorous studies on how the morphology and properties of these thin films are influenced by the surface chemistry of metal oxides and polymers and the extent of polymer wrapping are needed towards the systematical engineering of these materials.

In this work, we functionalize ITO nanocrystals with PAA-mPEO$_4$ to achieve colloidally stable aqueous "inks" suitable for the spray coating of optical quality electrochromic thin films in a more energy efficient and less toxic way. We expand on the polymer wrapping method developed previously by Duong and coworkers[166] to explore conditions favorable for PAA-mPEO$_4$ adsorption on ITO and control the wrapping density of the polymer layer by varying the pH and species present in the exchange solution (borate buffer, hydroxides, or pure Milli-Q water). First, we identify a pH dependence on the extent of PAA-mPEO$_4$ adsorption and thus colloid stability using a combination of transmission electron microscopy, dynamic light scattering, zeta potential, Fourier-transform infrared spectroscopy, and thermogravimetric analysis. Then, we compare the morphology and electrochromic behavior of thin films obtained from ITO of varying PAA-mPEO$_4$ wrapping densities. We find a trade-off between maximizing PAA-mPEO$_4$ coverage and key electrochromic parameters including optical contrast, reversibility, and coloration efficiency. In spite of this, we show that wrapping densities between 10 and 22% by mass lead to uniform optical quality composites with an electrochromic performance comparable to conventional ITO films.

EXPERIMENTAL METHODS

ITO Nanocrystal Synthesis and Ligand Stripping

Tin-doped indium oxide (ITO) nanocrystals were synthesized using a standard Schlenk line technique and under inert conditions. The synthesis was adapted from previously established colloidal methods.[98,99] Briefly, 2.5 g (8.6 mmol) In(ac)$_3$ and 0.225 g (0.95 mmol) Sn(ac)$_2$ were mixed with 10 mL of oleylamine and degassed under vacuum for 1 hour at 120°C. The solution was then heated to 230°C under nitrogen and was reacted

for 1 hour. After cooling to 60°C, 5 mL of toluene and 1 mL of oleic acid were added to the solution. The ITO nanocrystals were purified and recovered by adding reagent alcohol, centrifuging, and re-dispersing in toluene. After adding 100 μL of oleic acid to the ITO dispersion in toluene, four more washing cycles were performed (precipitation with reagent alcohol, centrifugation, re-dispersion in toluene).

The hydrophobic ligands bound to the ITO surface were chemically removed using nitrosonium tetraborofluorate ($NOBF_4$) following a procedure reported previously.[100] Briefly, $NOBF_4$ is added to a mixture containing equal volumes of as-synthesized ITO in toluene and N, N-dimethylformamide (DMF) based on a 1.7:1 ITO-to-$NOBF_4$ mass ratio. Ligand removal is then promoted by sonication, which leads to the transfer of bare ITO from toluene to DMF. The ITO is then recovered by precipitating with toluene, centrifuging, and re-dispersing in DMF and purified by repeating this washing cycle seven times.

Polymer Wrapping Procedure

PAA-$mPEO_4$ random copolymer was synthesized by the Helms group as described in their previous publication.[175] Bare ITO was polymer-wrapped by adapting methods previously developed for other nanocrystal and polymer compositions by Helms, Milliron, and co-workers.[166,167] Briefly, 10 mg of PAA-$mPEO_4$ were dissolved in 700 μL of DMF under gentle stirring. Once the polymer was completely dissolved, 300 μL of 90 mg/ml ligand-stripped ITO in DMF were added dropwise to the polymer solution (final volume 1 mL, 10 mg of PAA-$mPEO_4$ and 27 mg of ITO). The mixture was stirred at 400 rpm for 24 hours and subsequently added dropwise under constant stirring to an aqueous solution (19 mL) of either pure Milli-Q water (pH= 6.5) or 50 mM borate buffer (pH= 7.9, 8.5, or 9.1), which is henceforth referred to as the exchange solution. After stirring at 600 rpm for 48 hours, the exchange solution containing PAA-$mPEO_4$-wrapped ITO was purified with Milli-Q water by spin dialysis using 50 kDa Millipore Amicon Ultra centrifugal tubes. The final dispersion in Milli-Q water was filtered through a 0.45 μm PVDF membrane (Acrodisc, Pall).

Spray Coating

Film of PAA-mPEO$_4$-wrapped ITO were deposited onto 1.5 x 2.0 x 0.4 cm conductive FTO glass or 2.0 x 2.0 cm silicon substrates from ~8 mg/mL aqueous dispersions using an ExactaCoat® (Sono-Tek®) spray coater. Deposition is achieved at room temperature using a 0.05 mL/min flow rate, a nozzle-substrate distance of 8.5 cm, a carrier gas (N_2) pressure of 0.90 kPa, and a nozzle moving speed of 8 mm/s following a S-shaped motion with a spacing of 4 mm between each arc. This raster pattern is applied 10 consecutive times, resulting in coatings with an average thickness of ~130 nm (values are determined on a Vecco Dektak 150+ Profiler instrument). Samples are finally dried on a hot plate at 120 °C for 10 min to drive water evaporation.

Electron Microscopy

Transmission Electron Microscopy (TEM) micrographs of the PAA-mPEO$_4$-wrapped ITO dispersions were captured JEOL 2010F instrument with a Schottky Field Emission source operated at 200 kV. Samples were prepared by dropcasting the aqueous dispersions on TEM grids (Pelco® ultrathin carbon-A 400 mesh grid, Ted Pella), allowing them to fully evaporate under ambient conditions, and subsequently wicking them with acetonitrile to mitigate the degradation of hydrocarbons during exposure to the electron beam. Scanning electron microscopy (SEM) images of the resulting PAA-mPEO$_4$-wrapped ITO thin films sprayed onto silicon were captured on a Hitachi S5500 at a 15 kV accelerating voltage.

Fourier-transform Infrared Spectroscopy

FTIR spectra of polymer-wrapped ITO films sprayed onto undoped, double side polished silicon were recorded in transmission geometry with a Burker Vertex 70 spectrometer. Peak intensities from PAA-mPEO$_4$ vibrational mode reflect the relative polymer content across samples since dispersions of equivalent ITO concentration were spray coated to obtain films of similar ITO volume fraction.

Dynamic Light Scattering and Zeta Potential

Hydrodynamic diameter and zeta potential measurements were conducted on a Malvern Zetasizer Nano ZS. ITO nanocrystal dispersions were enclosed in disposable plastic micro cuvettes (ZEN0040, Malvern) for size measurements and in glass cuvettes to record zeta potentials with a dip cell (ZEN 1002, Malvern).

Thermogravimetric Analysis

The amount of PAA-mPEO$_4$ coating the nanocrystal surface was determined by TGA (Mettler Toledo TGA 2). In a typical experiment, 100 µL of polymer-wrapped ITO dispersion was added to a disposable aluminum crucible and the water evaporated under vacuum at room temperature over 24 hours. Samples were run in air from 30 ºC to 600 ºC at 5 ºC/min ramp rate.

Electrochemical Modulation

A custom-built spectroelectrochemical cell connected to a potentiostat (Bio-logic VMP3) and spectrometer (ASD Quality Spec Pro) was used for electrochemical and *in-situ* optical measurements in an Ar glovebox. The electrochromic performance of the spray coated ITO films was measured in a three-electrode and half-cell configuration, in which the ITO film deposited on FTO-coated glass (working electrode) and Li foil (both counter and reference electrode) are immersed in an electrolyte (1 M LiTFSI in tetraglyme). Optical modulation is induced by switching the applied potential between +4.0 (transparent state) and +1.5 V vs. Li/Li$^+$ (dark state). Each potential is held for 1 min. To measure coloration efficiency, samples were first fully bleached by applying a +4.0 V potential bias for 10 min, then subjected to amperostatic coulometry at -15 µA (corresponding to 10 times the value of the leakage current) during which consecutive absorbance spectra were recorded at a specific time interval of 5 s until the electrode reached a +1.5 V potential value corresponding to a fully darkened state.

RESULTS AND DISCUSSION

As-synthesized ITO nanocrystals, stabilized with hydrophobic ligands, were transferred into aqueous media after performing a two-step ligand-exchange procedure: ligand removal with $NOBF_4$ to produce stable ITO dispersions in DMF followed by polymer wrapping with PAA-$mPEO_4$ in water. Polymer wrapping was performed in aqueous solutions of varying pH (Milli-Q water at pH= 6.5 and borate buffers at pH= 7.9, 8.5, and 9.1) to explore conditions favorable for both the colloidal stability of ITO and electrochromic modulation when further processed into thin films. To produce the final colloid (Figure 4.1, insets), each exchange solution containing PAA-$mPEO_4$-wrapped ITO was purified via spin-dialysis with Milli-Q water. Characterization of the ITO morphology after each surface modification steps confirmed that our ligand exchange procedure is not destructive. TEM images of the final dispersions (Figure 4.1) show that, in all four cases, the original morphology of the ITO (Figure 4.2) is conserved without signs of etching. The only noticeable difference between these TEMs is the presence of aggregates in the dispersion obtained from the exchange solution at pH= 9.1 (Figure 4.1a), likely due to poor PAA-$mPEO_4$ coverage.

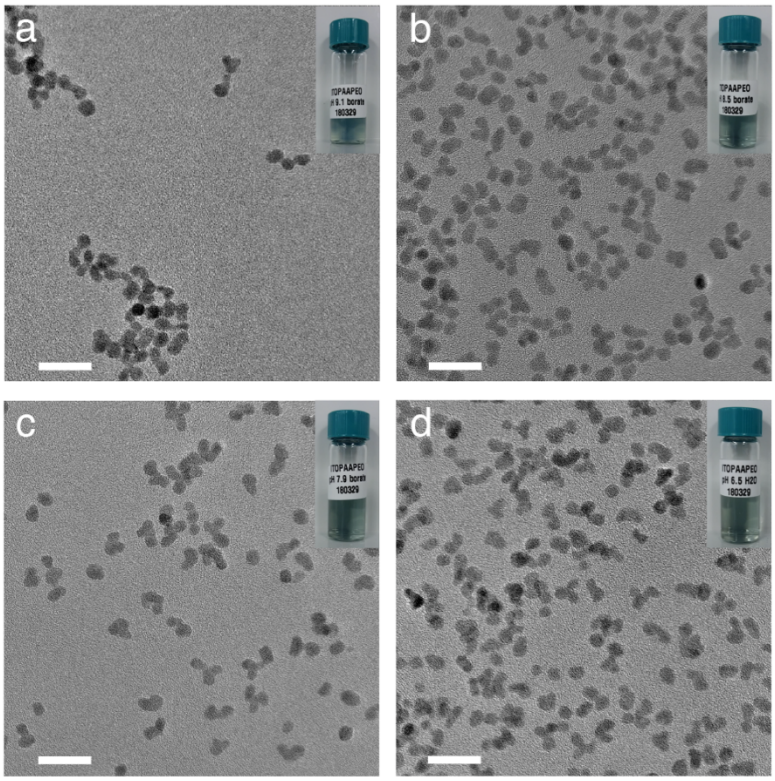

Figure 4.1: TEM of ITO aqueous dispersions after PAA-mPEO$_4$ wrapping.

a) pH= 9.1 borate buffer, b) pH= 8.5 borate buffer, c) pH= 7.9 borate buffer, and d) pH= 6.5 Milli-Q water. Scale bars = 20 nm. Inset: photograph of the corresponding vial.

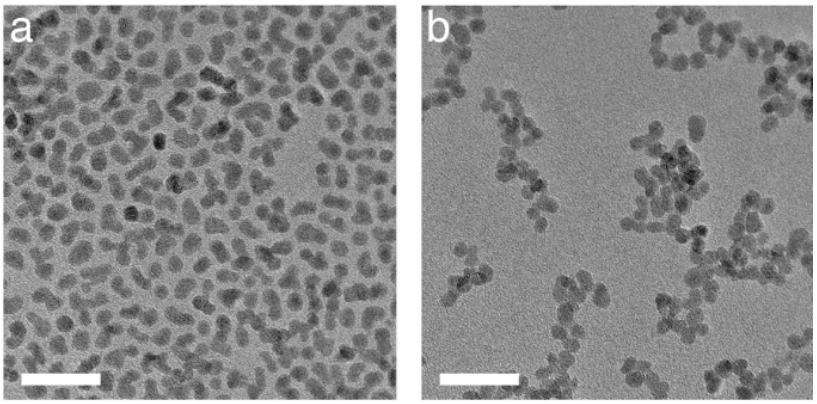

Figure 4.2: TEM images comparing the morphology of ITO nanocrystals before and after ligand removal.

a) As-synthesized ligand-capped and b) ligand-stripped. Scale bar = 25 nm.

To investigate the influence of pH on the colloidal stability of PAA-mPEO$_4$-wrapped ITO, we measured the hydrodynamic diameter and zeta potential of the four final dispersions described above. As shown in Figure 4.3a, transferring PAA-mPEO$_4$-wrapped ITO into pure Milli-Q water and mildly alkaline borate buffers (pH= 7.9 and 8.5) yields a hydrodynamic diameter of 10 nm while raising the pH to 9.1 leads to a larger hydrodynamic diameter (28 nm) with a broader distribution. Considering that the hydrodynamic diameter of both ligand-capped and ligand-stripped ITO nanocrystals is ~7 nm (see Chapter 2 or Appendix 3), we determined that aqueous exchange solutions at pH= 6.5, 7.9, and 8.5 stabilize discrete ITO nanocrystals whereas the exchange solution at pH= 9.1 favors the formation of ITO aggregates. Zeta potential measurements further support this result, since the magnitude of the zeta potential of the dispersion obtained from the exchange solution at pH= 9.1 is lower than 20 mV and thus indicative of poor colloidal stability, unlike the magnitude of the other three dispersions (Figure 4.3b). In addition, a negative zeta potential value for all four PAA-mPEO$_4$-wrapped ITO dispersions provides evidence of polymer coordination to the ITO surface, since the anionic carboxylate groups on the PAA backbone can coordinate to the positive charges on the ligand-stripped ITO surface (see Chapter 2 or Appendix 3). However, introducing other anionic species in the aqueous exchange solution (e.g., borate or hydroxide) could hinder the stabilization of ITO by PAA-mPEO$_4$ wrapping if they competitively adsorbed onto the surface.

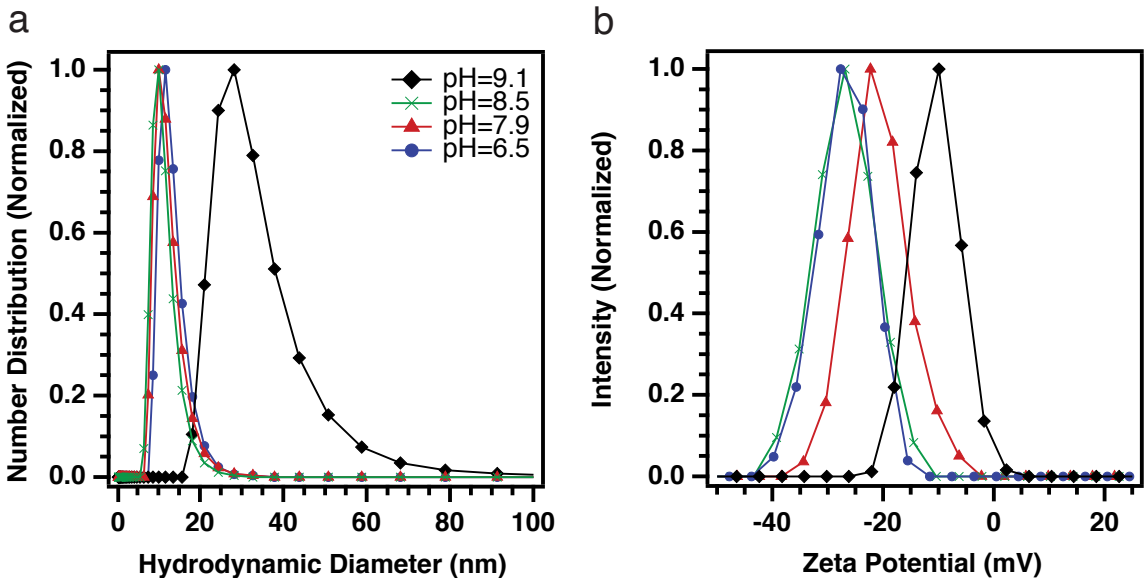

Figure 4.3: Colloidal stability of ITO aqueous dispersions after PAA-mPEO4 wrapping in exchange solutions of different pH.

a) Hydrodynamic diameter comparison and b) zeta potential comparison.

To further understand the exchange solution conditions that mediate the interaction between PAA-mPEO$_4$ and the ITO surface, we tracked and quantified polymer adsorption by FTIR and TGA. We detect PAA-mPEO$_4$ adsorption on the ITO surface and find that as the pH of the exchange solution increases, the amount of PAA-mPEO$_4$ wrapping decreases. First, examining the 2400-4000 cm^{-1} spectral region by FTIR reveals a gradual decrease in the intensity of CH_2 stretches (2900 cm^{-1}) from both PAA and PEO moieties[176,177] as pH increases (Figure 4.4a). In the 1400-1750 cm^{-1} spectral region, C=O stretches are significantly weaker compared to pure PAA-mPEO$_4$ (Appendix 3), suggesting that most of the carboxylic acid groups in PAA are deprotonated (Figure 4.4b).[178,179] In fact, the bands characteristic of asymmetric and symmetric carboxylate stretches appear at 1574 and 1452 cm^{-1}, respectively, and indicate carboxylate-metal bridging coordination on the ITO surface given a separation of $\Delta\nu$= 122 cm^{-1}.[179] Moreover, as pH increases, we note the gradual weakening of C-O-C stretches from PEO[176] (1140 cm^{-1}) accompanied by the emergence of borate bands: B-OH stretches from tetrahedral $B(OH)_4^-$ around 1030 cm^{-1}

(the broadness of the peak is likely due to additional contributions from In-OH and Sn-OH vibrational modes[180]) and B-O stretches from trigonal $(BOH)_3$ around 1412-1354 cm^{-1} (see Appendix 3 for borate FTIR reference).[181-183] These borate peaks are particularly predominant in the spectrum of the ITO dispersion processed from the exchange solution at pH= 9.1. Based on these FTIR results, we infer that borate anions compete with PAA-$mPEO_4$ for adsorption sites on the ITO surface and significantly prevent polymer adsorption when the buffer pH is around 9.1. Since the pKa of boric acid is close to 9.1,[184] we hypothesized that the concentration of borate anions at pH < 9.1 would decrease, thus improving the likelihood of PAA-$mPEO_4$ adsorption relative to borate. Although borate adsorption is favored at pH > 9.1, it is important to note that borate alone does not provide sufficient electrostatic stabilization since ITO dispersions prepared in the absence of polymer exhibit significant aggregation and precipitate out of solution in a matter of hours (Appendix 3). Therefore, the extent of electrostatic plus steric repulsion that PAA-$mPEO_4$ wrapping provides is key to ensure the colloidal stability of ITO aqueous dispersions over extended periods of time and even months. Quantifying polymer wrapping in these four dispersions by TGA further supports our claim, since the weight loss associated with the thermal decomposition of PAA-$mPEO_4$ decreases as pH increases: 28 % weight loss for pH= 6.5, 22 % weight loss for pH= 7.9, 18 % weight loss for pH= 8.5, and 10 % weight loss for pH= 9.1 (Figure 4.4c).

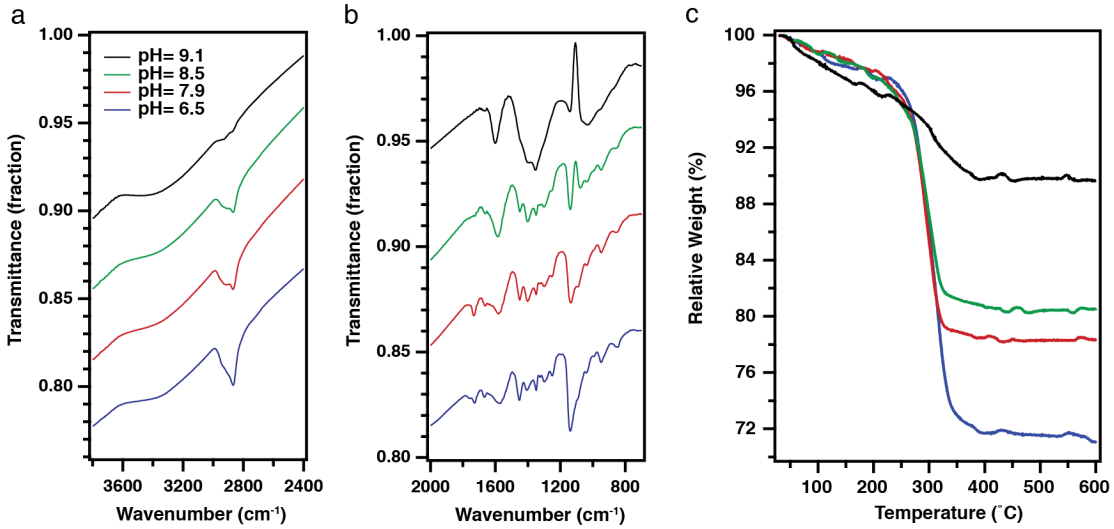

Figure 4.4: PAA-mPEO$_4$ adsorption on ITO is influenced by the pH of the exchange solution.

a) FTIR spectra showing a decrease in CH_2 stretch intensity with increasing pH. The sloping profile in the spectra is caused by absorption due to localized surface plasmon resonance, b) FTIR spectra showing a decrease in C-O-C stretch intensity and the emergence of borate vibrational modes with increasing pH, and c) TGA confirming a decrease in weight loss due to PAA-mPEO$_4$ decomposition with increasing pH. FTIR spectra were arbitrarily offset for clarity. Relative peak intensities are representative of PAA-mPEO$_4$ content since samples were prepared from dispersions having the same ITO concentration and resulted in films of similar thickness.

To deconvolute the influence of pH from the presence of borate anions on PAA-mPEO$_4$ adsorption, we performed the wrapping procedure in exchange solutions containing potassium hydroxide at two different pHs (8.3 and 12.4). The exchange solution at pH= 8.3 produces an ITO dispersion with a PAA-mPEO$_4$ wrapping density comparable to the wrapping density of the dispersion processed in Milli-Q water at pH= 6.5 (30 % weight loss by TGA, Figure 4.5), rather than the one obtained for pH= 8.5 with borate (18 % weight loss by TGA). The FTIR spectra of the samples obtained from aqueous solution pH= 6.5 and 8.3 are also in agreement (Figure 4.5). It is important to note that PAA-mPEO$_4$ wrapping of ITO in a phosphate buffer exchange solution at pH= 6.5 led to the irreversible aggregation of ITO and precipitation, which is why we were not able to control for the presence of additional anions at this pH. Nonetheless, the exchange solution at pH= 12.4

resulted in an ITO dispersion with a PAA-mPEO$_4$ wrapping density (8 % weight loss by TGA) comparable to the pH= 9.1 borate buffer case with FTIR bands characteristic of indium-hydroxyl coordination at 1100 cm^{-1} and O-H around 1630-1620 cm^{-1} instead of PAA-mPEO$_4$.[180] Therefore, as observed with borate buffer exchange solutions, hydroxide anions in solution compete with PAA-mPEO$_4$ for coordination sites on the ITO surface and significantly inhibit polymer adsorption above a threshold pH. The ability to tune PAA-mPEO$_4$ absorption on the ITO surface is thus not unique to borate anions; however, using borate buffer instead of hydroxide exchange solutions is preferred to avoid etching the ITO.

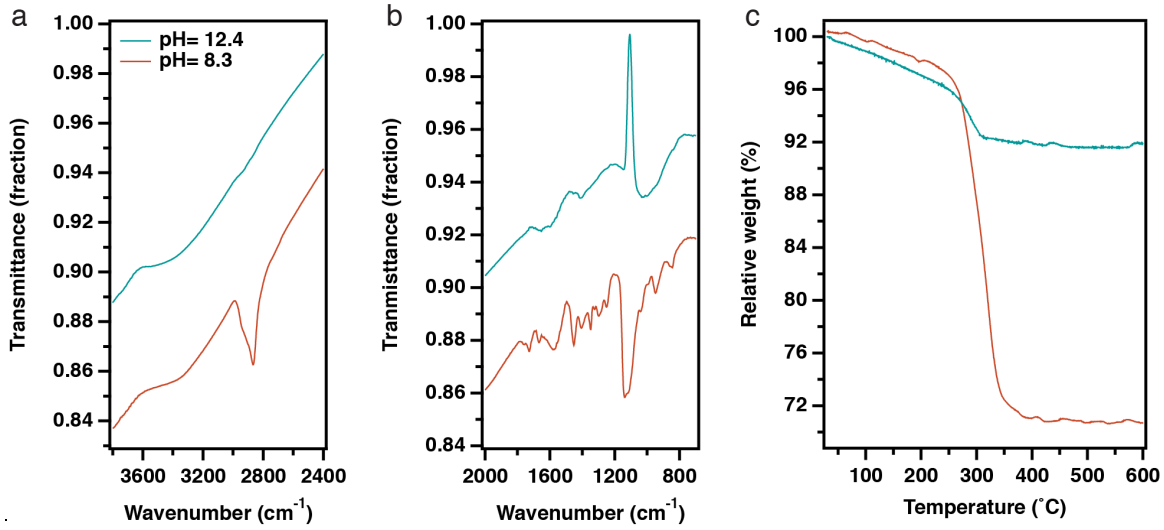

Figure 4.5: PAA-mPEO$_4$ adsorption on the ITO surface is inhibited by raising the pH of a potassium hydroxide exchange solution.

a) FTIR comparison of ITO functionalized in pH= 8.3 and 12.4 solutions highlights a decrease in CH_2 stretch intensity – the sloping profile in the spectra is caused by absorption due to localized surface plasmon resonance, b) FTIR comparison of ITO functionalized in pH= 8.3 and 12.4 exchange solutions highlights a decrease in C-O-C and carboxylate stretch intensity, and c) TGA confirms a significant decrease in PAA-mPEO$_4$ adsorption when ITO is functionalized in pH= 12.4 solution (8 % relative mass) compared to when ITO is functionalized in pH= 8.3 solution (30 % relative mass). FTIR spectra were arbitrarily offset for clarity. Relative peak intensities are representative of PAA-mPEO$_4$ content since samples were prepared from dispersions having the same ITO concentration and resulted in films of similar thickness.

PAA-mPEO$_4$-wrapped ITO dispersions (~8 mg/mL) were used as aqueous "inks" to produce uniform films (~130 nm) on 1.5 x 2.0 cm substrates through ultrasonic spray

deposition under ambient conditions (room temperature and atmospheric pressure) by applying a specific spray pattern at nozzle-substrate distance of 8.5 cm. SEM top-view images of ITO films show a complete coverage of the substrates (Figure 4.6). Film morphology is directly affected by the colloidal stability of the sprayed "inks": aggregated colloids (obtained from exchange solution at pH= 9.1) produce rough layers with obvious porosity (Figure 4.6a) while stable dispersions of discrete ITO nanocrystals (obtained from exchange solutions at lower pH) lead to smooth and uniform optical quality films (Figure 4.6b-d). Atomic force microscopy measurements further confirm the decrease of mean roughness R_a values for colloidally stable precursor inks (Appendix 3).

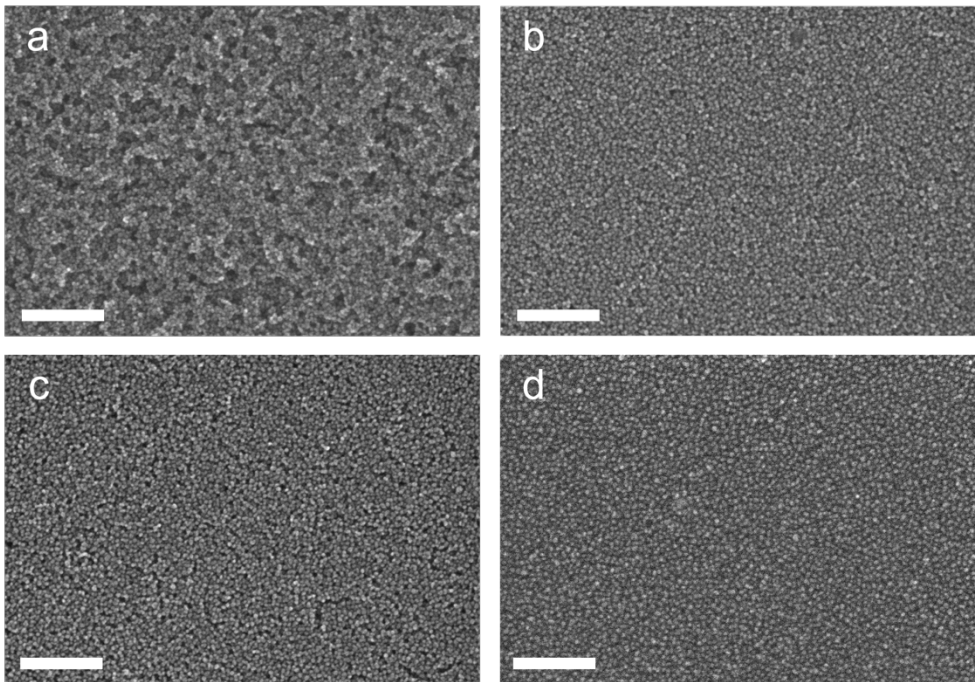

Figure 4.6: SEM of ITO films spray coated onto silicon substrates from aqueous dispersion after PAA-mPEO$_4$ wrapping.

a) pH= 9.1 borate buffer, b) pH= 8.5 borate buffer, c) pH= 7.9 borate buffer, and d) pH= 6.5 Milli-Q water. Scale bar = 100 nm.

The electrochromic behavior of ITO films, with varying PAA-mPEO$_4$ wrapping densities, spray coated onto FTO glass was investigated. Spectroelectrochemical

measurements (Figure 4.7) were conducted in a half cell configuration with the PAA-mPEO$_4$-ITO film (working electrode) and lithium foil (counter and reference electrodes) immersed in 1 M LiTFSI in tetraglyme electrolyte solution. First, the ITO films are bleached from their open circuit voltage state (black curve) to a fully transparent state (solid blue curve) by applying +4.0 V vs. Li/Li$^+$ and then darkened in the NIR by charging at +1.5 V (solid red curve). We observe that the amplitude of NIR modulation, measured at λ= 1900 nm, for the first electrochemical charging/discharging cycle (solid lines in Figure 4.7) is directly correlated to the PAA-mPEO$_4$ content in the ITO films. Optical contrast decreases as the relative polymer-to-ITO content in the film, directly related to the wrapping density on the dispersed ITO and the exchange solution conditions, increases: 39 % (ΔT= 75-36, Figure 4.7a) for the PAA-mPEO$_4$-ITO dispersion obtained from exchange solution pH= 9.1, 34 % (ΔT= 72-38, Figure 4.7b) from exchange solution pH= 8.5, 31 % (ΔT= 70-39, Figure 4.7c) from exchange solution pH= 7.9, and only 17 % (ΔT= 59-42, Figure 4.7d) from exchange solution pH= 6.5. After the second potentiostatic cycle, the effect of polymer wrapping density on optical modulation becomes more significant (dotted lines in Figure 4.7). While the film with the highest PAA-mPEO$_4$ wrapping density cannot be bleached back to its initial fully transparent state (2 % contrast or ΔT= 45-43, Figure 4.7d), ITO films with lower wrapping density exhibit large and stable contrasts (39 % or ΔT= 75-36 in Figure 4.7a, 33 % or ΔT= 72-39 in Figure 4.7b, and 27 % or ΔT= 68-41 in Figure 4.7c). These results suggest that exceeding a PAA-mPEO$_4$ wrapping density threshold on the ITO (of at least 28 % by relative mass) hinders the electrochromic reversibility of the composite film. To distinguish between the impact of PAA-mPEO$_4$ adsorption and the persistence of borate anions on the optical modulation, we recorded the spectroelectrochemical behavior of films deposited from PAA-mPEO$_4$-wrapped ITO processed in potassium hydroxide exchange solutions (Figure 4.8). Films of ITO dispersions processed in the absence of borate with a wrapping density of 30 % relative mass exhibit narrow and irreversible optical contrast (10 % or ΔT= 55-45). Conversely, films of ITO dispersions processed in the absence of borate with a wrapping density of 8 % relative mass achieve large and stable optical contrast (43 % or ΔT= 73-30).

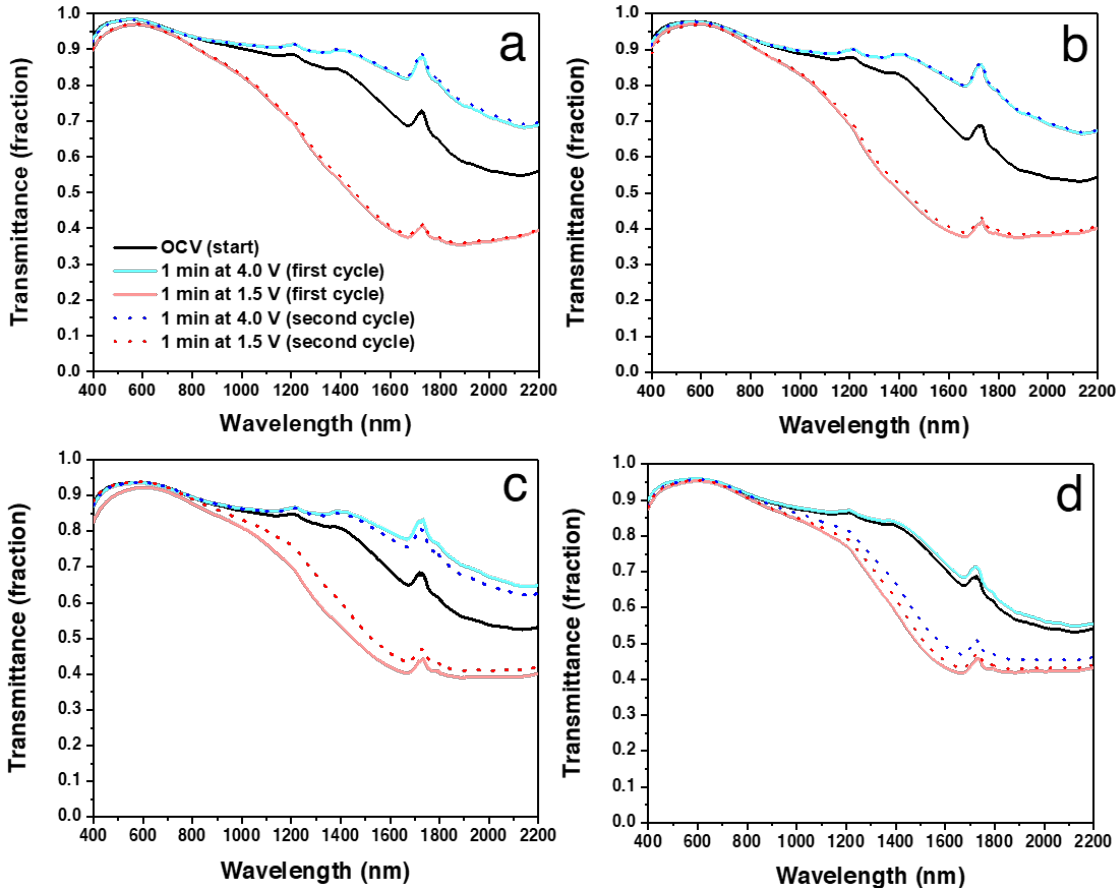

Figure 4.7: Electrochromic modulation of ITO films spray coated onto FTO glass from ITO aqueous dispersion after PAA-mPEO$_4$ wrapping.

a) pH= 9.1 borate buffer, b) pH= 8.5 borate buffer, c) pH= 7.9 borate buffer, and d) pH= 6.5 Milli-Q water. Transmittance spectra were recorded after applying 4.0 V ("bleached" state, blue curves) and 1.5 V ("darkened" state, red curves), referenced to a Li/Li$^+$ electrode in 1.0 M LiTFSI in tetraglyme, from the initial as-deposited state (black curves) at open circuit voltage. Solid lines correspond to the first potentiostatic "darkened-bleached" modulation cycle, and dotted lines correspond to the second cycle.

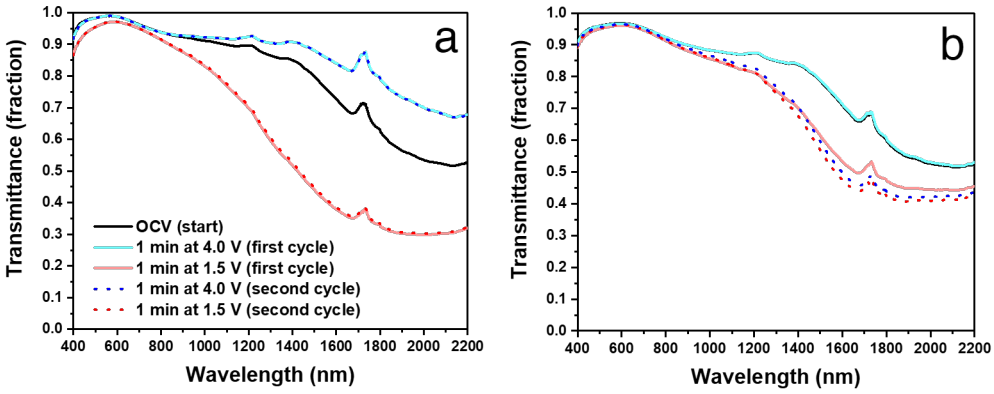

Figure 4.8: Electrochromic modulation of ITO films spray coated onto FTO glass from ITO aqueous dispersion after PAA-mPEO$_4$wrapping in potassium hydroxide exchange solution.

a) pH= 12.4 and b) pH= 8.3. Transmittance spectra were recorded after applying 4.0 V ("bleached" state, blue curves) and 1.5 V ("darkened" state, red curves), referenced to a Li/Li$^+$ electrode in 1.0 M LiTFSI in tetraglyme, from the initial as-deposited state (black curves) at open circuit voltage. Solid lines correspond to the first potentiostatic "darkened-bleached" modulation cycle and dotted lines correspond to the second cycle.

Coloration efficiency (CE), a measure of the change in optical density ΔOD per inserted charge density ΔQ, was obtained by fitting the linear region of the ΔOD vs. ΔQ curve (Figure 4.9). PAA-mPEO$_4$ wrapping on the ITO surface does not qualitatively diminish the electrochromic performance expected for capacitive charging of plasmonic metal oxides nanocrystals.[61,63,65] The four films deposited from ITO dispersions exposed to Milli-Q water and borate buffers exhibit CE values of similar order of magnitude as the values previously reported for bare ITO nanocrystal films: 535, 587, 673 and 802 cm^2/C in order of decreasing PAA-mPEO$_4$ wrapping density (or increasing exchange solution pH).[185,186] In addition, we observe that PAA-mPEO$_4$ wrapping density on ITO is inversely correlated to the CE of the resulting films. For instance, tracking the evolution of ΔOD over time (Appendix 3) shows that reaching a PAA-mPEO$_4$ wrapping density of 28 % relative mass leads to slower rate of coloration (ΔOD= 0.14 is reached after 600 s) relative to the other three films (ΔOD= 0.24, 0.28, and 0.32, in order of decreasing polymer wrapping density, is reached after 300 s) for the same amount of inserted charge (~1.4

mC/cm^2). Quantitative comparison of the CE values in this study to other reported values is not our goal, since CE could be strongly affected by film processing variabilities and the electrolyte composition.

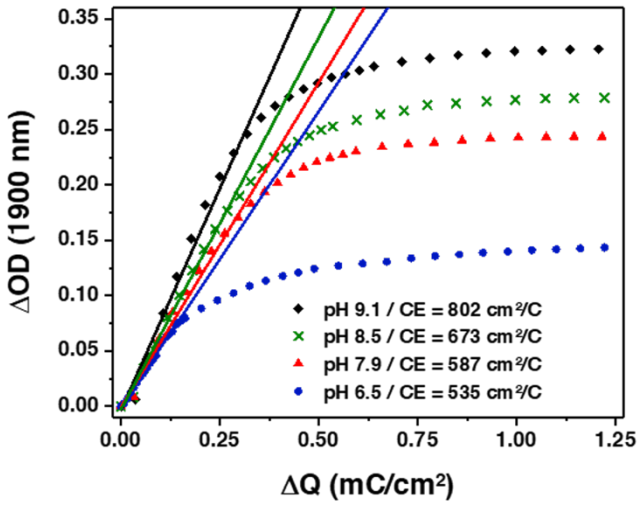

Figure 4.9: Coloration efficiency curves.

ITO films spray coated onto glass substrates from aqueous dispersion after PAA-mPEO$_4$ wrapping in different exchange solutions.

Table 4.1: Influence of PAA-mPEO$_4$ wrapping conditions on colloidal stability of ITO dispersions and electrochromic modulation of composite films.

Optical contrast and CE are measured at λ= 1900 nm.

Exchange solution	Zeta potential (mV)	Polymer density (%)	ΔT (%)		CE (cm²/C)	Reversible electrochromism?
			1st cycle	2nd cycle		
pH= 9.1 (borate)	-10	10	39	39	802	Yes
pH= 8.5 (borate)	-27	18	34	33	673	Yes
pH= 7.9 (borate)	-22	22	31	27	587	Yes
pH= 6.5 (Milli-Q)	-28	28	17	2	535	No

In view of the results summarized in Table 4.1, considering the extent of PAA-mPEO$_4$ wrapping on the ITO surface is crucial to achieve a compromise between colloidal stability and optimal electrochromic performance. In this system, an ITO dispersion with PAA-mPEO$_4$ wrapping of 18 % relative mass promotes colloidal stability without significantly inhibiting the optical modulation, coloration efficiency, and

charging/discharging kinetics of the resulting film compared to the best performing film obtained from an aggregated ITO dispersion (10 % relative mass). Furthermore, cyclic voltammetry (Appendix 3) reveals that the ITO film with the highest PAA-mPEO$_4$ wrapping density (28 % relative mass) exhibits a notably lower current density than the other three cases (10, 18, and 22 % relative mass). Given that PAA- and PEO-based polymers are widely used as solid electrolytes to enhance Li^+ transport,[172] we suspect that excessive wrapping with electronically insulating PAA-mPEO$_4$, could result in poor contact between ITO neighbors in the film and restrict electron conduction even more severely. Although beyond the scope of this work, further investigations would help elucidate the charge transport limitations of incorporating PAA-mPEO$_4$ into plasmonic nanocrystal films for electrochromic windows and other electrochemical devices. We envision that such studies could even motivate the design and implementation of other co-polymers to circumvent the current disadvantages of our system.

CONCLUSIONS AND OUTLOOK

We developed a method to produce colloidally stable dispersions of PAA-mPEO$_4$-wrapped ITO nanocrystals in water and demonstrated an environmentally conscious ("green") processing alternative for electrochromic thin films via ultrasonic spray deposition. We investigated the influence of the exchange solution conditions (pH and anionic species) on the extent of PAA-mPEO$_4$ wrapping on the ITO surface, which directly impacts the colloidal stability in water and thereby the morphology of the sprayed films. Although the as-deposited thin films modulate NIR light without the need to remove the polymer through post-deposition thermal or chemical treatments, we found that exceeding a polymer-wrapping density threshold results in irreversibly darkened films. Despite this limitation, we demonstrated the utility of PAA-mPEO$_4$-wrapped ITO, with polymer densities ranging from 10 to 22 % relative mass, as electrochromic films of comparable performance to conventional ligand-free plasmonic ITO films.[155,159,185] In particular, we identified a processing condition (borate buffer exchange solution at pH= 8.5, 18 % PAA-

mPEO$_4$ by mass relative to ITO) that favors colloidal stability while enabling reversible and fast optical modulation.

More generally, we have shown that the interaction between the polymer and the ligand exchange environment (e.g., pH and additional species in the aqueous solution) affects the extent of polymer wrapping and therefore colloidal stability. Control over these parameters allows the reliable deposition of optical quality films and optimization of the properties in composites. Beyond thin film deposition, designing and identifying processing conditions that promote colloidal stability is crucial to achieve multiscale assemblies (e.g., superlattices, gels, micelle-like structures, etc) of polymer-wrapped nanocrystals with controllable structures and unique properties. Furthermore, we envision that our functionalization method with PAA-mPEO$_4$ could broaden the applicability of ITO nanocrystals to areas where plasmonic metal oxides are less employed and explored such as hydrogels,[187-189] bioassays,[190,191] therapeutics,[61] toxicology studies,[192-195] and other biological applications.

Chapter 5: Future Directions for Depletion-Induced Nanocrystal Gelation

This dissertation sought to expand the assembly toolkit of metal oxide nanocrystals by inducing the gelation of these building blocks via polymer-mediated depletion attractions (Chapters 2 and 3) and achieving stable dispersions of polymer-wrapped tin-doped indium oxide nanocrystals (Chapter 4). Herein, we explored conditions to induce the gelation of charge-stabilized nanocrystals by varying the depletion attraction strength as a function of polymer (depletant) concentration. We demonstrated that the gelation threshold does not depend on the composition of the metal oxide, but is affected by the nanocrystal shape and the possibility of face-to-face packing. Furthermore, we found that bridging attractions can cause the formation of nanocrystal gels at low polymer concentration and complicate the phase behavior of the system. However, the composition (i.e. specific surface chemistry) and size of the nanocrystals seems to affect the extent of aggregation due to polymer adsorption, which we hypothesized would be suppressed by functionalizing the nanocrystal surface with a polymer that would not interact with the depletant. A combination of structure analysis using SAXS and theoretical phase behavior predictions of the nanocrystal-polymer mixtures (both dispersions and gels) allowed us to rationalize and support these findings. Finally, our gelation approach enabled the assembly of optically active macroscopic materials with a strong infrared light absorption reflective of both the nanoscale properties inherent to the building blocks and the gel structure.

Having developed these first steps towards establishing guidelines for depletion-based nanocrystal gelation, this framework offers rich opportunities to further control the gel microstructure by tuning internanocrystal interactions in dispersions and thereby explore structure-property relationships in gel assemblies. A few viable and interesting extensions of this work include i) investigating the influence of the nature and strength of repulsions on the gel microstructure and local packing of nanocrystals in the network, ii) comparing the mechanical and self-healing properties of nanocrystal gels induced via

depletion attractions and bridging attractions, and iii) the use of stimuli-responsive depletants to realize reconfigurable and switchable nanocrystals gels.

Regarding the first study, given that the range of parameters that affect the strength of repulsions such as the type of interaction (electrostatic, steric, or both), the colloid (size, surface charge, and characteristics of the stabilizing molecule) and the solvent conditions (dielectric constant, ionic strength, and mixing affinity with stabilizing molecule), tuning repulsions could provide multiple ways to broaden the variety of self-assembled gel microstructures, rather than solely tuning the strength of attractions. To this end, nanocrystal surface functionalization such as polymer-wrapping (Chapter 4) and coordinating charged species to the metal oxide surface[164,165] is a particularly useful strategy to tune repulsions while maintaining colloidal stability and diversify the solvent compatibility of the colloid. Accessing different microstructures with detailed nanoscale control is essential for developing a fundamental understanding of structure-property relationships in gel assemblies.

Related to the mechanical properties of nanocrystal gels assembled with different types of short-range attractions, preliminary rheology experiments using the bridging and depletion gels described in Chapter 2 show that both types of gel recover their elasticity after being subjected to complete deformation under high strain (Figure 5.1 and 5.2). We also note that the kinetics of network reformation are slower for the bridging gel compared to the depletion gel, which recovers instantaneously. However, issues related to solvent evaporation limit the number of low (0.1%) and high (100%) strain cycles that can be applied to the sample and therefore identify more trends, while the presence of small clusters of bridged nanocrystals in the depletion gel complicate the exhaustive interpretation of these results. Nonetheless, these experiments motivate further investigating the mechanical properties to understand the interplay between the type of interparticle interaction, the microstructure, and mechanical properties of the macroscopic material. Assembling these gels in aqueous solutions, given PEG's affinity for water (attempts to assemble nanocrystal gels in dimethylformamide and dimethylsulfoxide, which are organic solvents with higher boiling points than acetonitrile, resulted in PEG

precipitation), would be a promising way to circumvent solvent evaporation during the experiment. In addition, probing depletion gels composed of a network of discrete nanocrystals (Chapter 3), as opposed to a network of clusters of bridged nanocrystals, would allow to deduce more robust conclusions from rheology experiments.

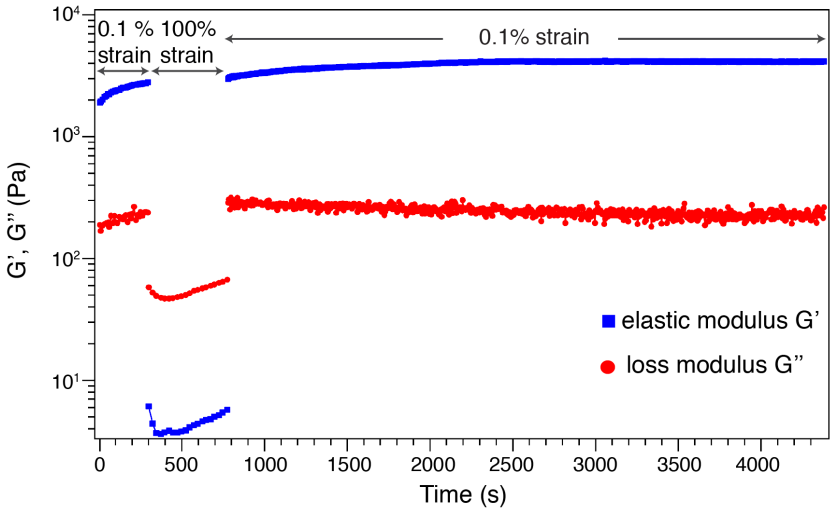

Figure 5.1: Evolution of the elastic and loss modulus of a tin-doped indium oxide nanocrystal depletion gel over time at a fixed frequency (5 rad/s).

Plot courtesy of Jennifer Imbrogno. Experiment designed in collaboration with Jennifer Imbrogno and Michael P. Howard. The analyzed sample corresponds to the depletion gel described in Chapter 2 (4 vol% nanocrystal, [PEG]= 534 mM or 587 mg/mL).

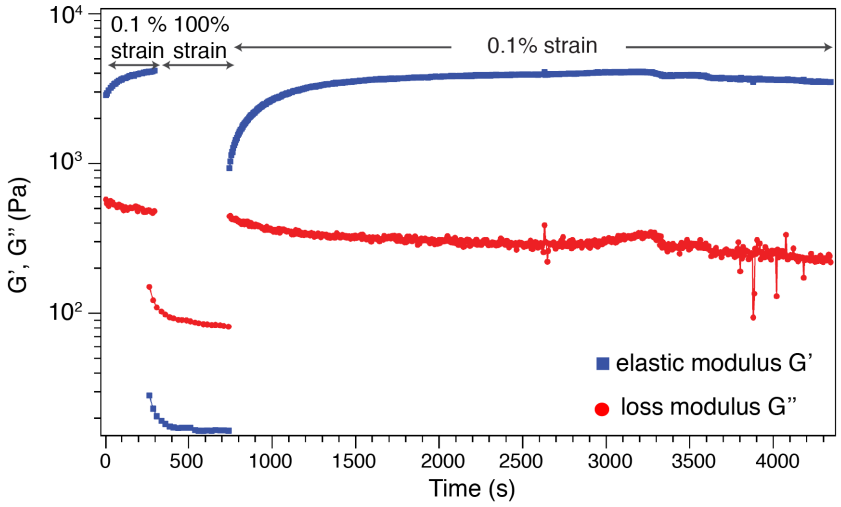

Figure 5.2: Evolution of the elastic and loss modulus of a tin-doped indium oxide nanocrystal bridging gel over time at a fixed frequency (5 rad/s).

Plot courtesy of Jennifer Imbrogno. Experiment designed in collaboration with Jennifer Imbrogno and Michael P. Howard. The analyzed sample corresponds to the bridging gel described in Chapter 2 (4 vol% nanocrystal, [PEG]= 46.0 mM or 50.6 mg/mL).

Although the universality of depletion attractions in the context of nanocrystal gelation was demonstrated in this dissertation by assembling metal oxide nanocrystals of different compositions and shapes, this versatile attribute was not explored for different depletants. The motivation to pursue this proposed study is two-fold: i) adapt the nanocrystal gelation via depletion attraction to diverse materials and solvent combinations, thereby addressing the surface chemistry limitations inherent to the nature of the building blocks, in an effort to maximize the generality of the approach and impact as many nanotechnologies as possible and ii) grant additional functionality to the composite and design complex nanocrystal gels with switchable and programmable responses to external stimuli. In the case of the latter, strategically selecting nanocrystal-depletant pairs to use these building blocks as each other's stimulus and target could lead to powerful macroscopic gels of nanomachine networks. Instances of coupled stimuli responses that mediate clustering in solution have been investigated with gold nanoparticle/poly(N-isopropylacrylamide) or PNIPAM and silver nanoparticle/PNIPAM system.[28,189]

Appendices

APPENDIX 1: SUPPORTING INFORMATION FOR CHAPTER 2

Experimental Supporting Figures

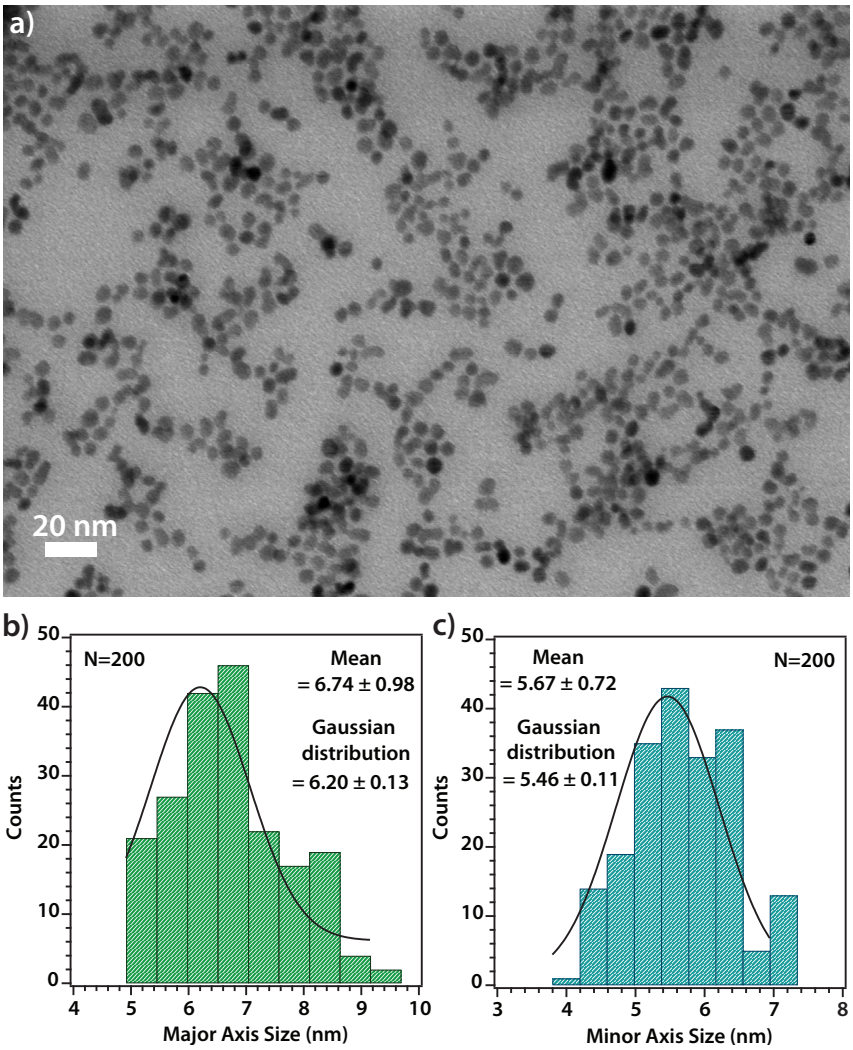

Figure A1.1: Sizing of as-synthesized tin-doped indium oxide (ITO) nanocrystals.

a) Scanning transmission electron microscopy image of nanocrystals sized using the ellipsoid tool in ImageJ, b) histogram of the manually measured major axis size for 200 nanocrystals, and c) histogram of the manually measured minor axis size for 200 nanocrystals. For both histograms, mean and standard deviation and results from a Gaussian fit are reported.

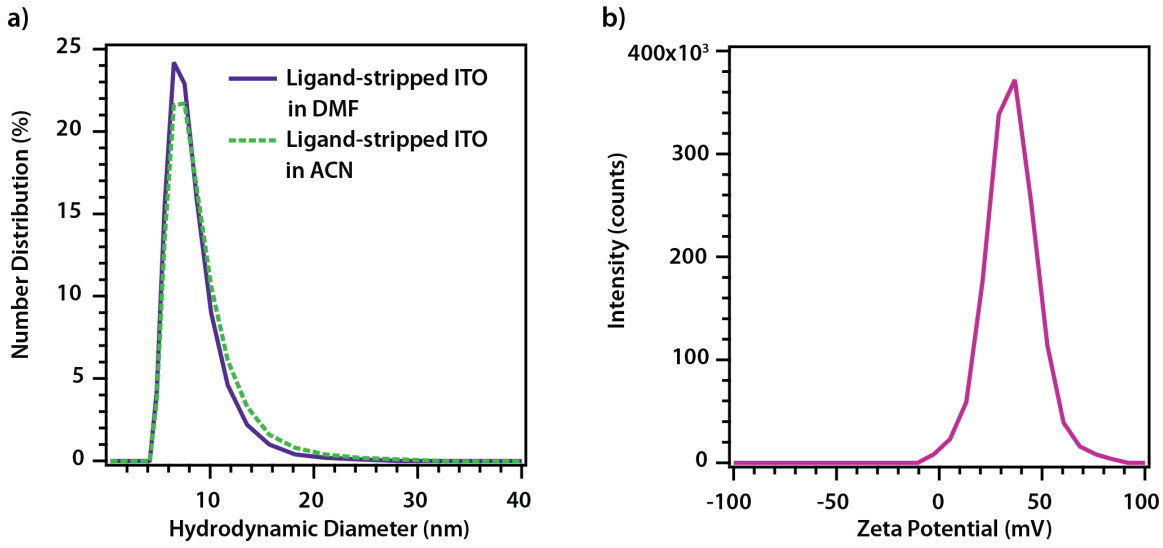

Figure A1.2: Colloidal stability of ligand-stripped nanocrystals in polar solvents.

a) Dynamic light scattering of ligand-stripped ITO nanocrystals dispersed in acetonitrile (ACN, dashed green) and dimethylformamide (DMF, purple). In both cases, the maximum number distribution corresponds to a hydrodynamic diameter D_h= 6.5 nm, close to the diameter measured by electron microscopy (Figure A1.1), thus confirming the integrity of the nanocrystal cores and b) zeta potential of ligand-stripped ITO nanocrystals dispersed in dimethylformamide (ζ= +36.5 mV).

Figure A1.3: Comparison of the solubility of polyethylene glycol (PEG, M_n= 1100 g/mol) in acetonitrile (left vial) and dimethylformamide (right vial) at a concentration of 664 mg/mL.

Although PEG dissolves in both dimethylformamide and acetonitrile, the latter has a Hildebrandt solubility parameter closer to the one of PEG[196,197] and was therefore chosen as the solvent matrix for our ITO-PEG gels. In fact, the PEG in acetonitrile solution shows no signs of precipitation for over a year while the PEG in dimethylformamide remains cloudy during the same timeframe.

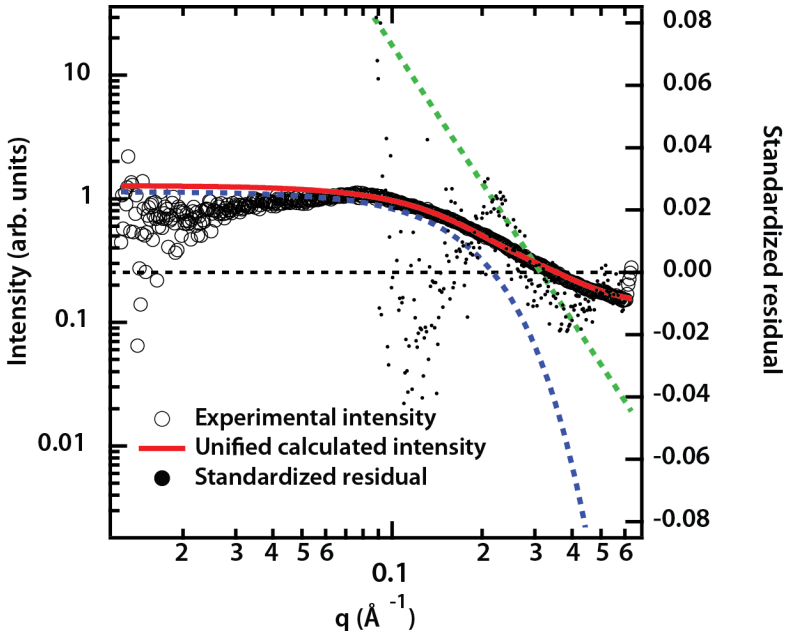

Figure A1.4: PEG (M_n= 1100 g/mol) in acetonitrile sizing by small angle X-ray scattering.

Unified fit (red) and component curves of the unified function (Guinier: dashed blue and Porod: dashed green) based on Beaucage's unified exponential-power law analysis. Fits were performed with Irena's Unified Fit tool in Igor Pro.

Table A1.1: Extracted unified fit parameters from PEG sizing by small-angle X-ray scattering.

G and B are scaling coefficients in the unified function, R_g is the radius of gyration, and P is the Porod exponent. The parameters are defined and described in more detail in work by Beaucage.[113,117]

Fitting Parameters	
G	1.14
Rg [Å]	9.80
B	0.003
P	3.70
Background	0.137

Table A1.2: Summary of nanocrystal volume fractions measured by inductively coupled plasma-atomic emission spectroscopy.

The overall tin dopant concentration of as-synthesized ITO nanocrystals and the volume fractions of ligand-stripped ITO dispersed in pure acetonitrile and ITO gel ([PEG]= 534 mM) were measured on a Varian 720-ES ICP Optical Emission Spectrometer. The samples were digested in 70 wt. % nitric acid for 36 hours. Calibration standards and samples were diluted to 2 vol. % nitric acid in ultrapure Milli-Q water. ITO nanocrystal mass was calculated assuming a $In_{2-x}Sn_xO_3$ stoichiometry and nanocrystal volume was calculated using the theoretical density of ITO[198] (ρ= 7.12 g/cm^3, 10 wt. % doped). The overall tin dopant concentration is 9.65 at. % (9.94 wt. %). The ligand-stripped ITO dilution series was used to determine extinction cross sections.

Sample	ITO mass (mg)	ITO volume (mL)	Total sample volume (mL)	Volume fraction (%)
Ligand-stripped ITO (dilution factor= 10.1)	6.10	$8.55 \cdot 10^{-4}$	4.00	$2.14 \cdot 10^{-2}$
Ligand-stripped ITO (dilution factor= 11.7)	5.32	$7.45 \cdot 10^{-4}$	4.02	$1.85 \cdot 10^{-2}$
Ligand-stripped ITO (dilution factor= 15.7)	3.94	$5.52 \cdot 10^{-4}$	4.00	$1.38 \cdot 10^{-2}$
Ligand-stripped ITO (dilution factor= 19.8)	3.14	$4.40 \cdot 10^{-4}$	4.01	$1.10 \cdot 10^{-2}$
Ligand-stripped ITO (dilution factor= 29.4)	2.11	$2.96 \cdot 10^{-4}$	4.01	$7.38 \cdot 10^{-3}$
ITO Gel [PEG]= 534 mM	0.656	$9.35 \cdot 10^{-5}$	$2.33 \cdot 10^{-3}$	4.00

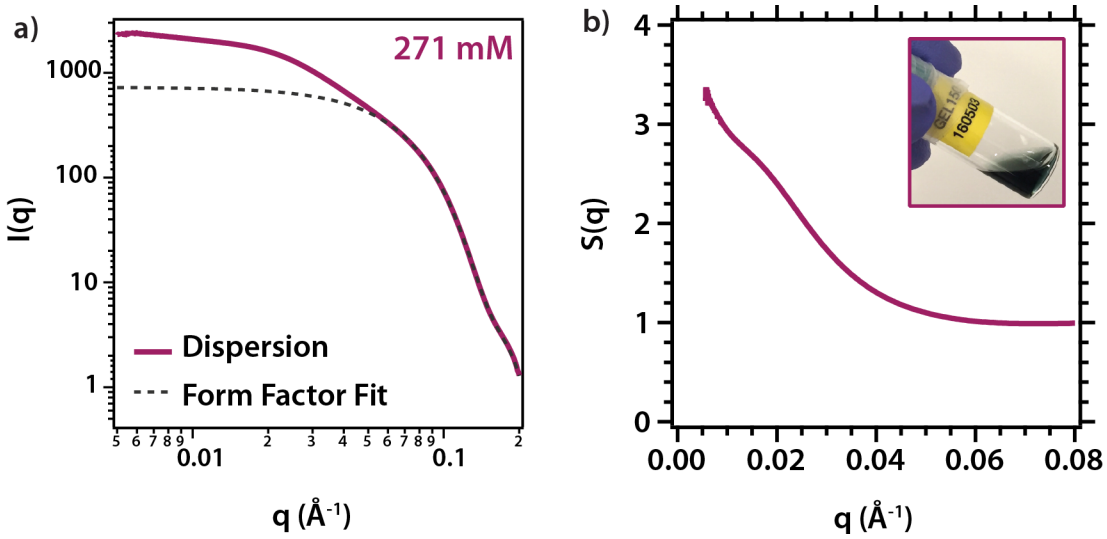

Figure A1.5: Small-angle X-ray scattering analysis of ITO-PEG dispersion with [PEG]= 271 mg/mL.

a) Total scattering intensity and form factor fit using the spheroid model and b) structure factor S(q) (inset: photograph of dispersion in a vial).

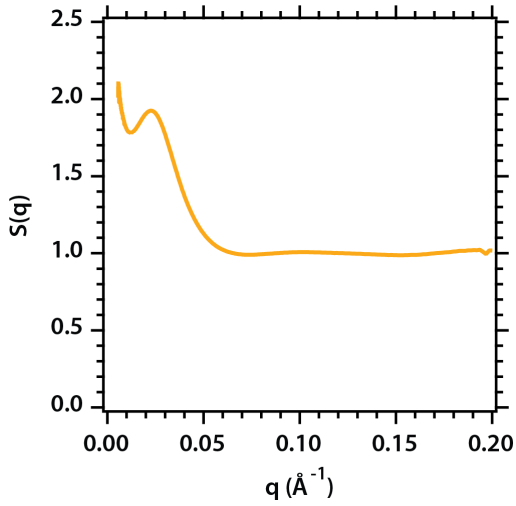

Figure A1.6: Full range of the structure factor S(q) of the ITO-PEG dispersion with [PEG]= 8.00 mM.

The broad and weak peak at q~ 0.1 $Å^{-1}$ can be attributed to adjacent nanocrystal interactions since the form factor fitting assumes a dilute system of negligible structure factor.

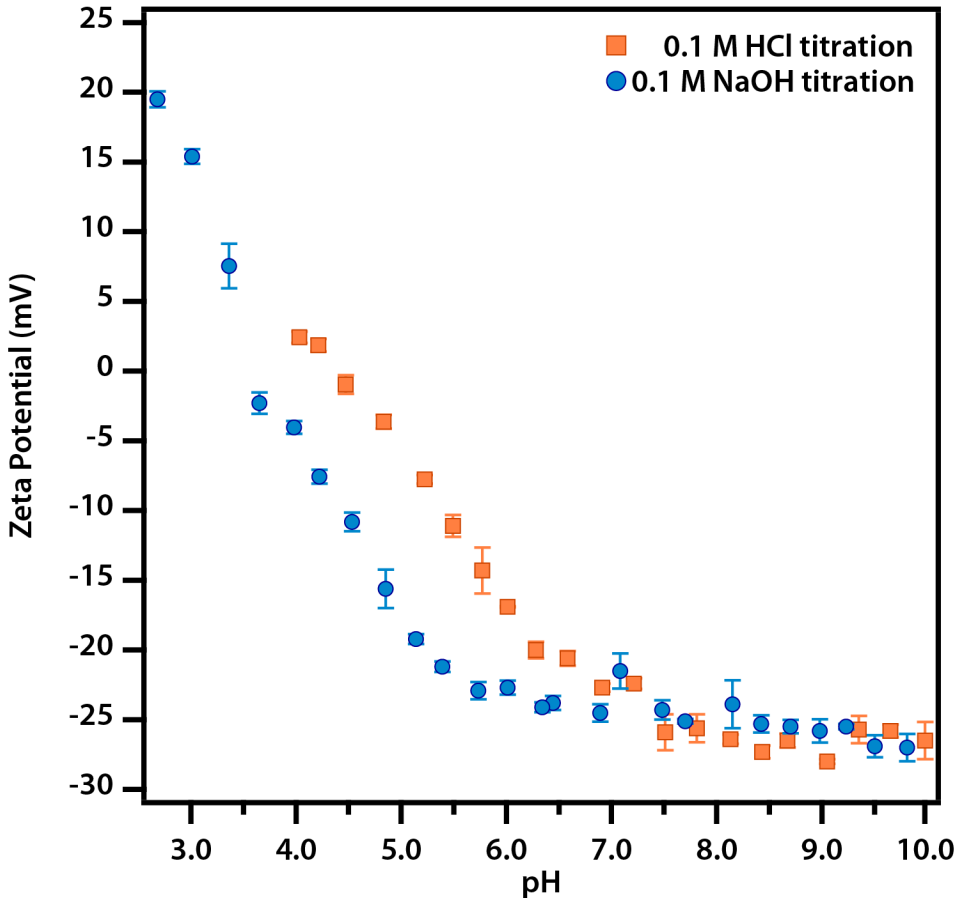

Figure A1.7: Isoelectric point measurement of ligand-stripped ITO nanocrystals.

Zeta potential values were collected as a function of pH using Malvern's MPT-2 autotitrator. Ligand-stripped nanocrystaks were dispersed in 1 mM hydrochloric acid (HCl) aqueous solution and titrated with a 0.1 M sodium hydroxide (NaOH) solution followed by a titration with a 0.1 M HCl solution in a folded capillary zeta cell (DTS1070, Malvern).

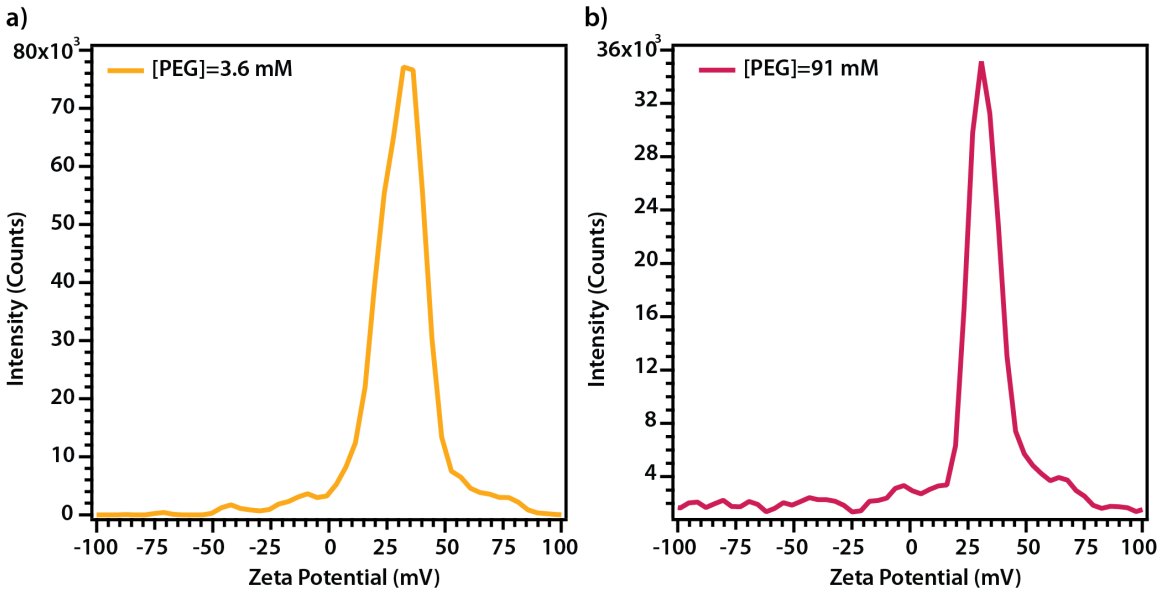

Figure A1.8: Zeta Potential of ITO-PEG dispersions.

a) Zeta potential (ζ= +33 mV) of an ITO-PEG mixture in acetonitrile with [PEG]= 3.6 mM and b) zeta potential (ζ= +31 mV) of an ITO-PEG mixture in acetonitrile with [PEG]= 91 mM.

Theoretical Model for Bridging and Depletion Gelation

At its core, the theory exploits a well-established free energy model for polymer depletion. Effects of strong polymer adsorption are then accounted for by Wertheim's first order association theory. To maintain consistency with the theoretical literature, below we use the generic terms colloid and polymer for the ITO nanocrystal and PEG, respectively.

As the foundation, we employ an accurate free energy model for the well-known Asakura Oosawa mixture. The Asakura Oosawa model treats the colloids as hard spheres of diameter d_C and the polymers as particles that interact with colloids as though they have a hard sphere diameter $d_P = 2R_G$ (R_G is the radius of gyration); however, the polymers are mutually non-interacting. Specifically, we model the Helmholtz free energy (A_{AO}) per volume (V) and unit of thermal energy (k_BT)

$$a_{AO} = \frac{A_{AO}}{Vk_BT} \quad (1)$$

using the theory of Lekkerkerker et al.,[36] which decomposes the free energy into colloid (C) and polymer (P) contributions

$$a_{AO} \cong a_{\mathrm{I}} + a_{\mathrm{C}}^{(\mathrm{ex})} + a_{\mathrm{P}}^{(\mathrm{ex})} \tag{2}$$

The ideal contribution, a_{I}, is

$$a_{\mathrm{I}} \equiv \rho_C ln\rho_C + \rho_P ln\rho_P - \rho_C - \rho_P \tag{3}$$

where $\rho_C \equiv N_C/V$ and $\rho_P \equiv N_P/V$ are the colloid and polymer number densities, respectively, and N_C and N_P are the corresponding number of colloids and polymers. The excess colloidal free energy, $a_{\mathrm{C}}^{(\mathrm{ex})}$, is approximated by the accurate Carnahan-Starling result for hard spheres

$$a_{\mathrm{C}}^{(\mathrm{ex})} \equiv \rho_C \left[\frac{1}{(1-\eta_C)^2} + \frac{2}{(1-\eta_C)} - 3\right] \tag{4}$$

where $\eta_C \equiv \rho_C \pi d_C^3/6$ is the colloid volume fraction. The excess polymer contribution, $a_{\mathrm{P}}^{(\mathrm{ex})}$, is based on free volume arguments yielding

$$a_{\mathrm{P}}^{(\mathrm{ex})} = \rho_C[A\gamma + B\gamma^2 + C\gamma^3 - \ln(1-\eta_C)] \tag{5}$$

$$A \equiv 3\lambda + 3\lambda^2 + \lambda^3$$

$$B \equiv 9\lambda^2/2 + 3\lambda^3$$

$$C \equiv 3\lambda^3$$

$$\lambda \equiv d_P/d_C$$

To account for strong polymer-colloid association we non-perturbatively add in attractions via Wertheim theory. The theory assumes that there is some fixed number of association sites available on the surface of the polymer (n_P) and the colloid (n_C). While in our context there are not literal adsorption sites, the colloid does have a limited surface area that can only harbor a finite number of adsorbed polymers. Moreover, the polymer can only bridge

some finite number of colloids due to geometric constraints. In the main text, we refer to n_P as n_{bind} and n_C as n_{ads}. With the fictive binding sites, the additional excess free energy contribution due to binding[199,200] is

$$a_{\mathrm{B}}^{(\mathrm{ex})} = \sum_{i=C,P} \rho_i \left[n_i ln X_i - \frac{n_i X_i}{2} + \frac{n_i}{2} \right] \tag{6}$$

where X_C and X_P are the fraction of the colloid and polymer site that are un-bonded and are determined by solving the following two coupled "reaction" equations

$$X_i = \left[1 + n_j \rho_j X_j \Delta_{P,C} \right]^{-1}, \; i \neq j \tag{7}$$

$$\Delta_{P,C} \sim g_{P,C} v_{P,C}$$

where $v_{P,C}$ is the thermal bond volume that incorporates the attraction strength (relative to the thermal energy/temperature) and range between polymer and colloid, and $g_{P,C}$ is the contact value of the radial distribution function at contact in a reference system where the polymer-colloid attractions are not present. $v_{P,C}$ can be regarded as a constant in the experiments; the value of 0.181 has been used in the figure of the main text to achieve rough agreement between experiment and theory. On the other hand, $g_{P,C}$ has a non-trivial dependence on the density and composition of the system. Specifically, we have used the approximation of Santos et al.[201]

$$g_{P,C} \cong \frac{1}{1-\eta_C} + \frac{2 d_P / d_C}{1 + d_P / d_C} \left[\frac{1 - \eta_C / 2}{(1-\eta_C)^3} - \frac{1}{1-\eta_C} \right] \tag{8}$$

Combined, the total theoretical free energy is

$$a \equiv a_{AO} + a_{\mathrm{B}}^{(\mathrm{ex})} \tag{9}$$

which through thermodynamic stability calculations provides predictions for spinodally unstable regions possessing a strong tendency for gelation. Spinodally unstable points are identified by satisfaction of the following condition

$$\begin{vmatrix} \frac{\partial^2 a}{\partial \rho_C^2} & \frac{\partial^2 a}{\partial \rho_C \rho_P} \\ \frac{\partial^2 a}{\partial \rho_P \rho_C} & \frac{\partial^2 a}{\partial \rho_P^2} \end{vmatrix} \leq 0 \tag{10}$$

where $|A|$ is the determinant of matrix A. Equation 10 essentially states the system is no longer stable against fluctuations in the composition, at least to second order.

LSPR Simulation and COMSOL Methods

The nanocrystal gel structure was designed using the design module in COMSOL. An idealized gel structure was designed with the purpose of understanding the impact of complex multi-scale optical coupling phenomenon originating from the fractal gel structure. The simulated structure was assembled as a periodic structure of a unit cell forming a 2D chain composed of clusters of PEG-coated ITO nanocrystals. These structures were then surrounded by the surrounding medium (i.e., acetonitrile (n=1.344), which was used for all experimental measurements) (Figure A1.9). To simulate the localized surface plasmon resonance (LSPR) – LSPR coupling in periodic arrays of the unit cell, the Maxwell equations were solved in full field mode. The maximum and minimum mesh size in the nanocrystal was set to 10 nm and 0.1 nm, respectively (Figure A1.10). This ensures fine meshing, yielding typically 2 million degrees of freedom, which corresponds to 3 – 15 GB of RAM when using the direct PARDISO or MUMPS solver.

The dielectric function of ITO is described by a frequency dependent dielectric function, which was expressed using the Extended Drude model.

$$\epsilon_p = \epsilon_\infty - \frac{\omega_p^2}{\omega^2 - \gamma\omega} \tag{11}$$

$$\gamma = \gamma_L - \frac{\gamma_L - \gamma_H}{\pi}\left[arctan\left(\frac{\omega - \gamma_X}{\gamma_W}\right) + \frac{\pi}{2}\right] \tag{12}$$

To obtain the dielectric function of ITO, spectra of ITO nanocrystal dispersions were fitted using Mie theory. The dielectric function used for ITO is tabulated in the table below (Table A1.3).

Table A1.3: Dielectric parameter for ITO.

	Plasma frequency, ω_p, cm^{-1}	Low frequency damping, γ_L, cm^{-1}	High frequency damping, γ_H, cm^{-1}	Crossover frequency, γ_X, cm^{-1}	Crossover width, γ_W, cm^{-1}
ITO	13272	4694	170	5319	936

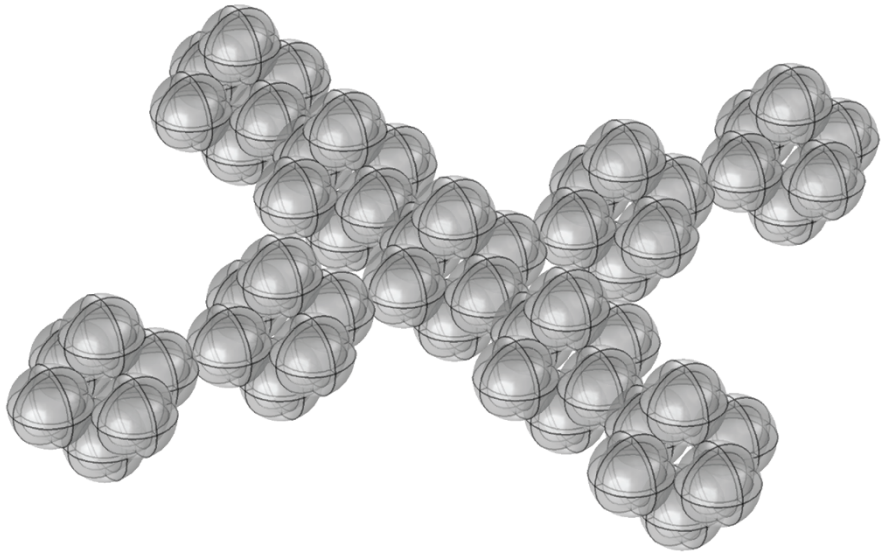

Figure A1.9: Simulated Structure Geometry.

A 2D chain of PEG-coated nanocrystal clusters was designed using the Design module in COMSOL.

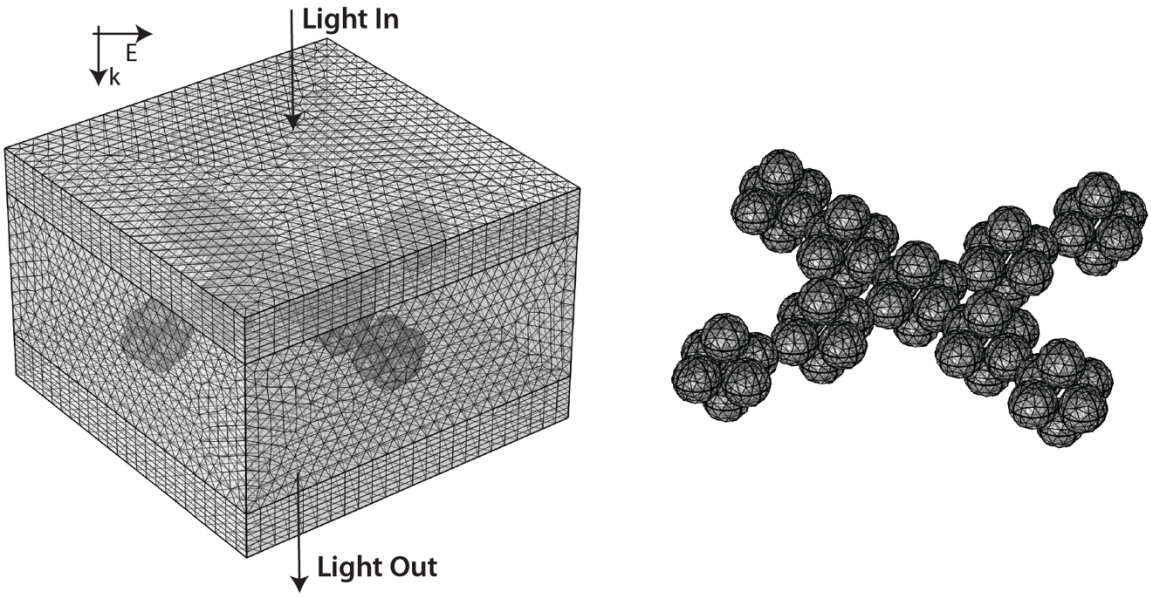

Figure A1.10: Meshing.

A 2D chain of PEG-coated nanocrystal clusters (right) in 2D periodic lattice (left).

APPENDIX 2: SUPPORTING INFORMATION FOR CHAPTER 3

Experimental Supporting Figures

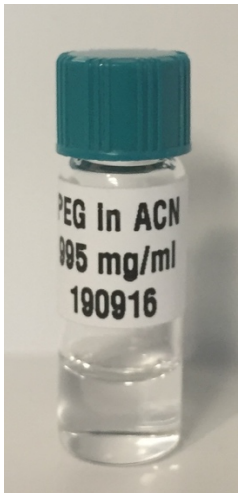

Figure A2.1: Photograph of PEG solution in acetonitrile.

The solution ([PEG] = 995 mg/mL) is transparent and does not show signs of precipitation.

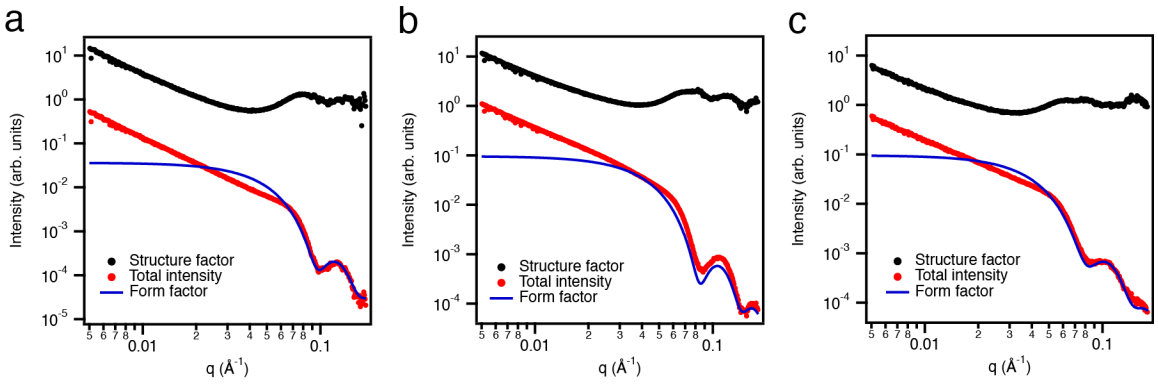

Figure A2.2: Structure factor S(q) deconvolution.

Total intensity, form factor and S(q) for gels composed of a) FeO_x, b) $Sn:In_2O_3$, and c) $F,Sn:In_2O_3$ nanocrystals. Form factor curves were obtained by fitting the experimental form factors as shown in Chapter 3 Figure 3.1. Structure factors were deconvoluted by dividing the total scattering intensity by the fitted form factor, assuming a decoupling approximation (nanocrystal size and shape are not correlated with position) and a local monodisperse

approximation.[20] The intensity of the fitted form factor was adjusted such that S(q) ~ 1 at the highest resolvable q.

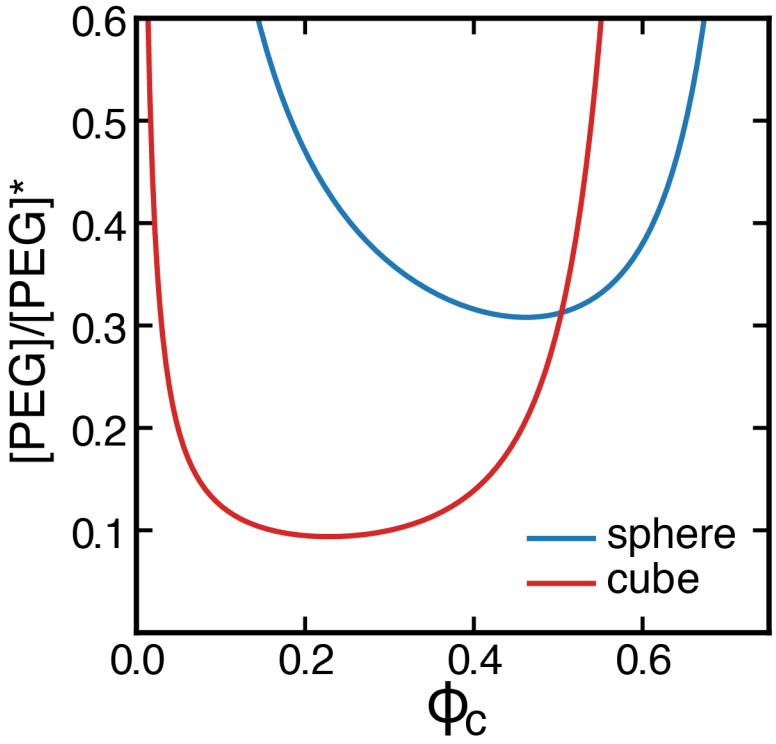

Figure A2.3: Theoretical spinodal boundaries for spherical Sn:In_2O_3 and cubic F,Sn:In_2O_3 nanocrystals.

The nanocrystal volume fraction is denoted by ϕ_C, and the free polymer mass concentration $[PEG]$ is normalized by the overlap concentration $[PEG]^* = 3M_n/4\pi R_g^3 N_A$, where M_n is the polymer molecular weight, R_g is the polymer radius of gyration, and N_A is Avogadro's number.

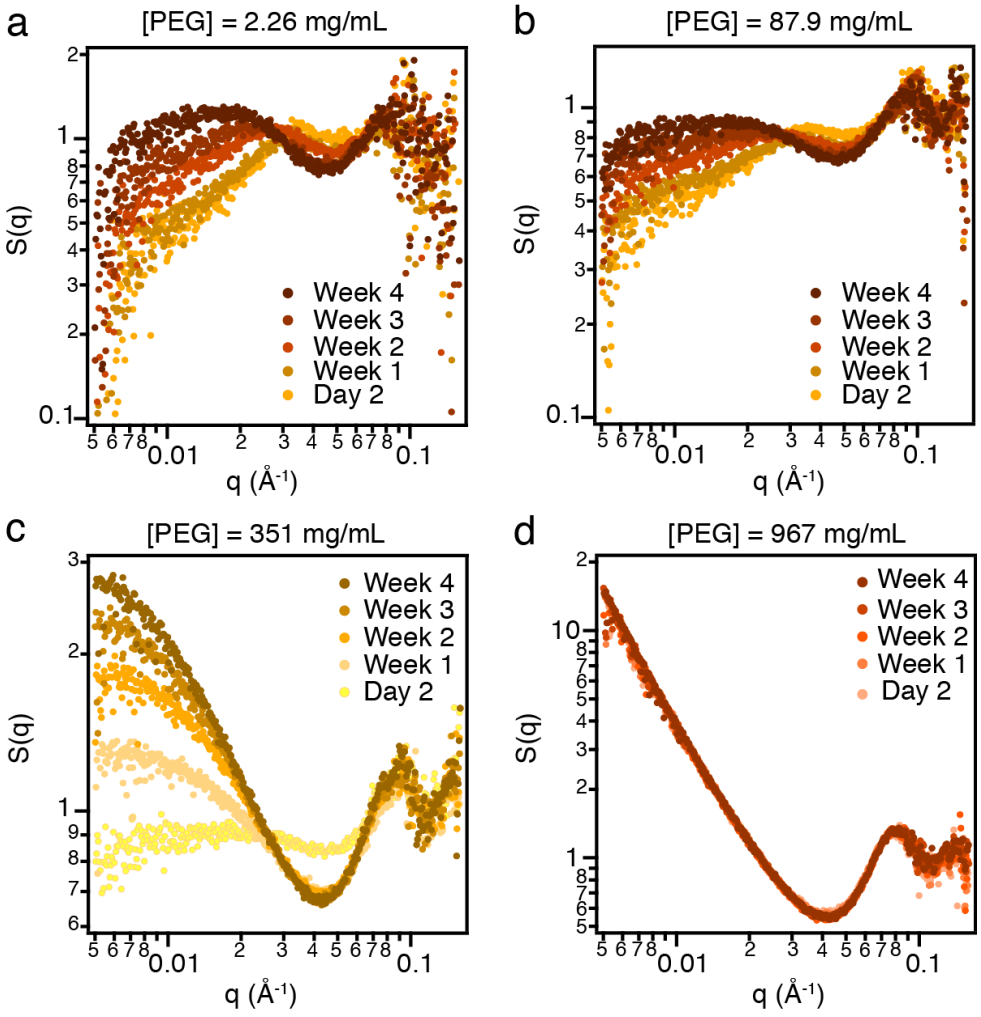

Figure A2.4: Evolution of structure factor S(q) of FeOx nanocrystal-PEG mixtures over 4 weeks.

a) Flowing dispersion ([PEG]= 2.26 mg/mL, [PEG]/[PEG]*= 0.005), b) flowing dispersion ([PEG]= 87.9 mg/mL[PEG]/[PEG]*= 0.190), c) flowing dispersion ([PEG]= 351 mg/mL, [PEG]/[PEG]*= 0.758), and d) gel ([PEG]= 967 mg/mL, [PEG]/[PEG]*= 2.09). The broad peaks around q < 0.03 Å^{-1} in the flowing dispersions indicate the presence of small aggregates.

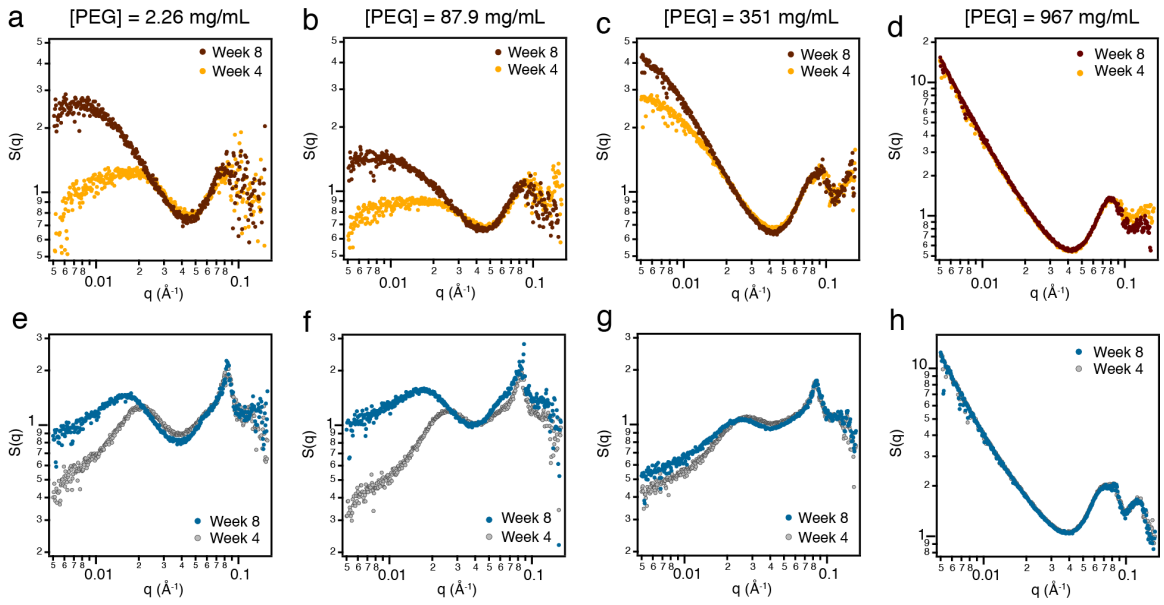

Figure A2.5: Evolution of structure factor S(q) of FeO_x nanocrystal-PEG and $Sn:In_2O_3$ nanocrystal-PEG mixtures between 4 and 8 weeks.

a) FeO_x nanocrystal flowing dispersion ([PEG]= 2.26 mg/mL, [PEG]/[PEG]*= 0.005), b) FeO_x nanocrystal flowing dispersion ([PEG]= 87.9 mg/mL, [PEG]/[PEG]*= 0.190), c) FeO_x nanocrystal flowing dispersion ([PEG]= 351 mg/mL, [PEG]/[PEG]*= 0.758), d) FeO_x nanocrystal gel ([PEG]= 967 mg/mL, ϕ_{PEG}= 2.09), e) $Sn:In_2O_3$ nanocrystal flowing dispersion ([PEG]= 2.26 mg/mL, [PEG]/[PEG]*= 0.005), f) $Sn:In_2O_3$ nanocrystal flowing dispersion ([PEG]= 87.9 mg/mL, [PEG]/[PEG]*= 0.190), g) $Sn:In_2O_3$ nanocrystal flowing dispersion ([PEG]= 351 mg/mL, [PEG]/[PEG]*= 0.758), and h) $Sn:In_2O_3$ nanocrystal gel ([PEG]= 967 mg/mL, [PEG]/[PEG]*= 2.09).

We note that $Sn:In_2O_3$ nanocrystal-PEG dispersions are more stable than FeO_x nanocrystal-PEG dispersions. The only difference between the systems is the surface chemistry of the metal oxide, which is known to affect the extent of PEG adsorption depending on the pH. The isoelectric point of FeO_x is typically around 6.5-7.5[202,203] while the isoelectric point of $Sn:In_2O_3$ is lower and closer to 5.[143] Since it has been shown that the basic ether groups in PEG preferentially interact with stronger acid sites on the metal oxide surface, [120,204,205] we expect that the extent of PEG adsorption on $Sn:In_2O_3$ is greater than on FeO_x, which in turn promotes the stability of the small clusters. Furthermore, as [PEG] increases in the $Sn:In_2O_3$ nanocrystal dispersions, the scattering intensity and sharpness of the peak around q ~0.025 $Å^{-1}$ decreases. This suggests that at [PEG]= 351

mg/mL the Sn:In_2O_3 surface is not saturated with PEG yet, unlike in the FeO_x nanocrystal-PEG system.

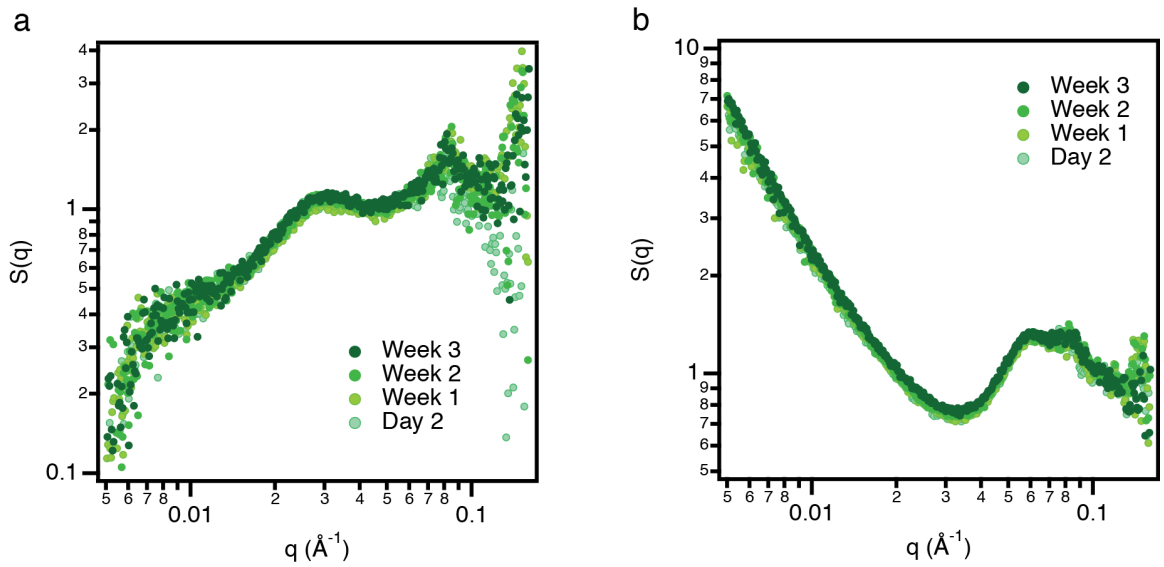

Figure A2.6: Evolution of structure factor S(q) of F,Sn:In_2O_3 nanocrystal-PEG mixtures over 3 weeks.

(a) Flowing dispersion ([PEG]= 2.26 mg/mL, [PEG]/[PEG]*= 0.005). The broad peaks around q ~ 0.03 Å^{-1} indicates the presence of small aggregates and (b) gel ([PEG]= 351 mg/mL, [PEG]/[PEG]*= 0.758).

Theoretical Methods

Using free volume theory and scaled particle theory, the equation of state for a nanocrystal dispersion having depletion attractions induced by noninteracting, penetrable depletant spheres can be written as

$$\tilde{P}(\phi_c, \phi_{PEG}^R) = \tilde{P}_0(\phi_c) + \phi_{PEG}^R \, f(\phi_c)$$

where

$$f(\phi_c) = \frac{1}{\delta^3}\left(\alpha(\phi_c) - \phi_c \frac{d\alpha}{d\phi_c}\right)$$

Here, $\tilde{P} = Pv_c/k_BT$ is the dimensionless pressure and $\tilde{P}_0 = P_0 v_c/k_BT$ is the dimensionless hard particle pressure in the absence of depletant), k_B is Boltzmann's constant, T is temperature, v_c is the volume of a single nanocrystal, $\delta = R_g/R$ is the ratio of depletant size R_g to R, the nanocrystal radius (for spheres) or half-width (for cubes), and ϕ_{PEG}^R is the volume fraction of PEG depletant in a hypothetical reservoir in equilibrium with the dispersion. For dilute nanocrystal volume fractions, the reservoir volume fraction is approximately equal to the bulk depletant volume fraction in the dispersion ϕ_{PEG}, though the depletant can partition differently between different phases if phase separation occurs. The PEG volume fraction $\phi_{PEG} \equiv [PEG]/[PEG]^*$ is written in terms of the PEG concentration relative to the overlap concentration $[PEG]^* \equiv 3M_n/4\pi R_g^3 N_A$, where $M_n = 1100\ \mathrm{g/mol}$ is the polymer molecular weight, $R_g = 0.98\ \mathrm{nm}$ is the polymer radius of gyration, and N_A is Avogadro's number. For nanocrystal spheres, the hard particle equations of state is well-approximated by the Carnahan-Starling[206] expression,

$$\tilde{P}_0(\phi_c) = \frac{\phi_c + \phi_c^2 + \phi_c^3 - \phi_c^4}{(1-\phi_c)^3},$$

and α is given by an expression from Lekkerkerker and Tuinier,[35]

$$\alpha(\phi_c) = (1-\phi_c)\exp\left[-\frac{3\delta(1+\delta)\phi_c}{1-\phi_c} - \frac{9\delta^2\phi_c^2}{2(1-\phi_c)^2} - \delta^3\tilde{P}_0\right].$$

For nanocrystal cubes, the hard particle equations of state is given by an expression from Boublík,[207]

$$\tilde{P}_0(\phi_c) = \frac{\phi_c + 5\phi_c^2/2 + 13\phi_c^3/4 - 6\phi_c^4}{(1-\phi_c)^3},$$

and α is given by an expression from García, Opdam, and Tuinier,[153]

$$\alpha(\phi_c) = (1-\phi_c)\exp\left[-\frac{3\delta(2+\pi\delta)\phi_c}{1-\phi_c} - \frac{18\delta^2\phi_c^2}{(1-\phi_c)^2} - \frac{\pi\delta^3\tilde{P}_0}{6}\right].$$

The spinodal curve $\phi_{PEG}^R(\phi_c)$ is computed by solving

$$\frac{d\tilde{P}}{d\phi_c} = 0$$

for ϕ_{PEG}^R in terms of ϕ_c.

APPENDIX 3: SUPPORTING INFORMATION FOR CHAPTER 4

Experimental Supporting Figures

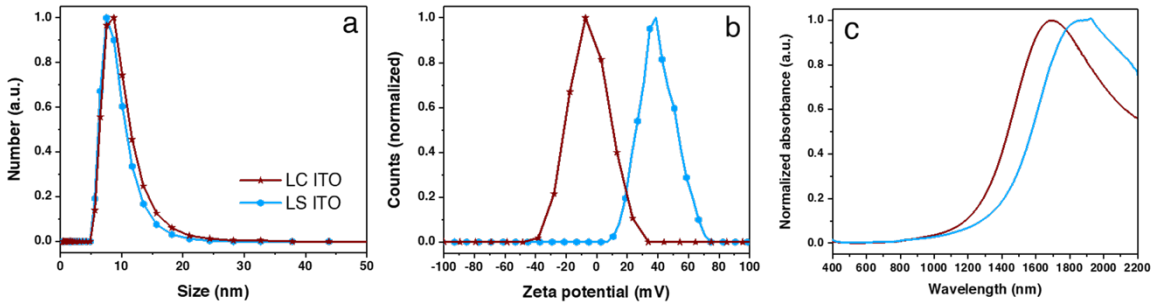

Figure A3.1: Comparison of ligand-capped (LC) and ligand-stripped (LS) ITO dispersions.

a) Hydrodynamic diameter, b) zeta potential, c) and localized surface plasmon resonance (LSPR). UV-vis-NIR measurements were collected on an Agilent-Cary 5000 spectrophotometer using a near-infrared quartz cuvette (1 mm path length, Spectrocell). The shift in LSPR peak position is caused by the change in dielectric environment (hexane for LC ITO and dimethylformamide for LS ITO).

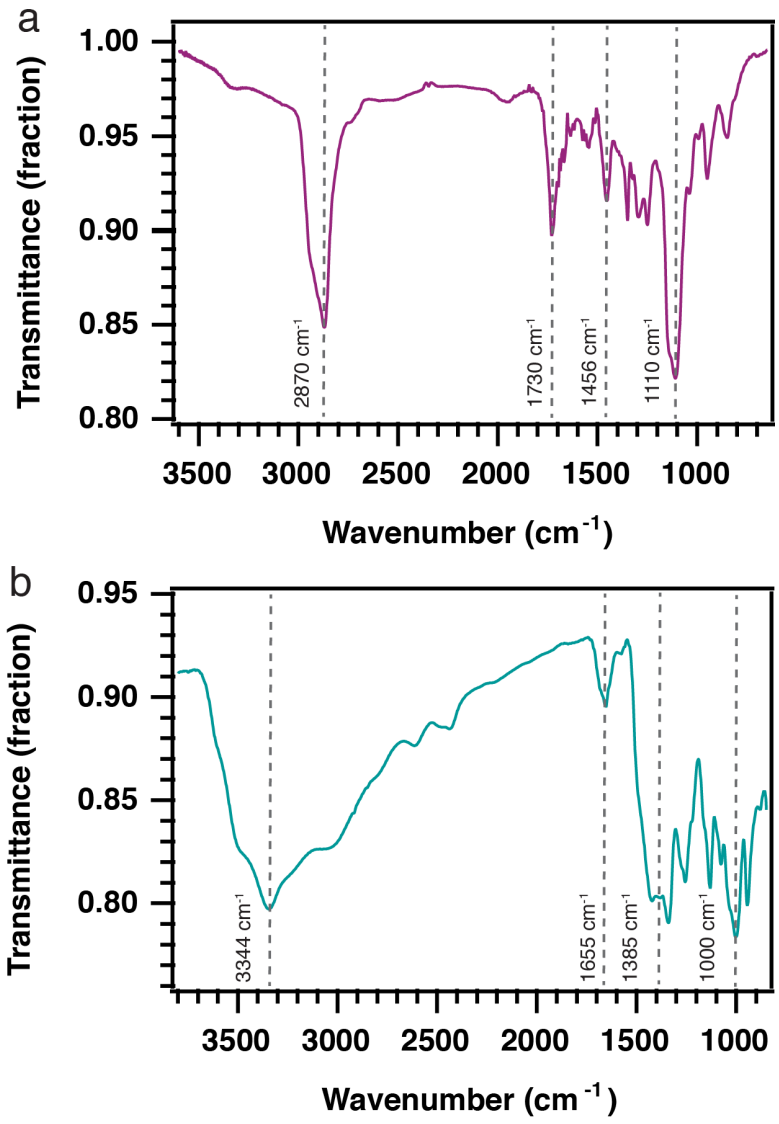

Figure A3.2: FTIR reference for PAA-mPEO$_4$ and sodium tetrafluoroborate.

a) Neat PAA-mPEO$_4$: the peaks at 2870, 1730, 1456, and 1100 cm^{-1} are assigned to CH_2, C=O, C-O, and C-O-C stretches, respectively[176,177] and (b) neat sodium tetraborate: the peaks at 3344, 1385, and 1100 cm^{-1} are assigned to OH and B-O stretches from $(BOH)_3$, and $(BOH)_4^-$, respectively, while the peak at 1655 cm^{-1} is assigned to H-O-H bends.[181-183] FTIR spectra of PAA-mPEO$_4$ and sodium tetraborate references were recorded in transmission geometry with a Burker Vertex 70 spectrometer. Samples were dropcasted from dilute solutions (~ 1 mg/ml) onto CaF_2 windows and left to dry under ambient conditions.

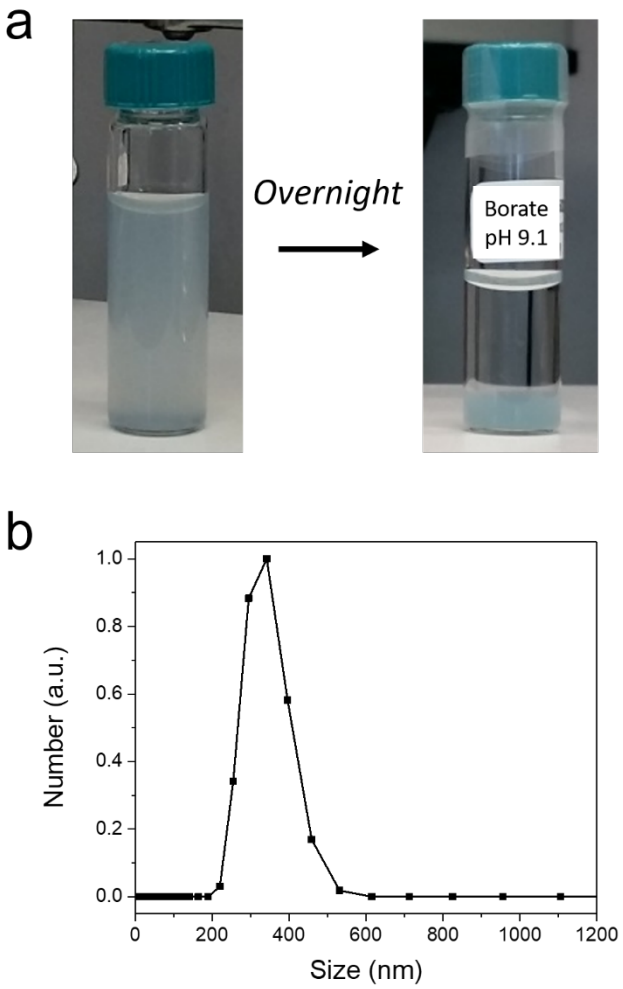

Figure A3.3: ITO dispersion after exposure to ligand exchange at pH= 9.1 containing borate only (no PAA-mPEO$_4$).

a) Aggregation and precipitation of ITO is observed after a few hours and b) dynamic light scattering measurement confirms presence of ITO aggregates with a ~350 nm average hydrodynamic diameter.

Table A3.1: Summary of roughness measurements by profilometry and atomic force microscopy.

Atomic force microscopy measurements were carried out on a Digital Instrument Nanoscope III microscope (Veeco) in tapping mode with a "Super Sharp Improved Super Cone" probe of 5 nm tip diameter (TeamNanotec). Reported values are averages and ± indicates standard deviation.

Exchange Solution	Roughness (R_a, nm)
pH= 9.1 borate buffer	2.77 ± 0.03
pH= 8.5 borate buffer	1.28 ± 0.04
pH= 7.9 borate buffer	0.82 ± 0.05
pH= 6.5 Milli-Q water	0.65 ± 0.11

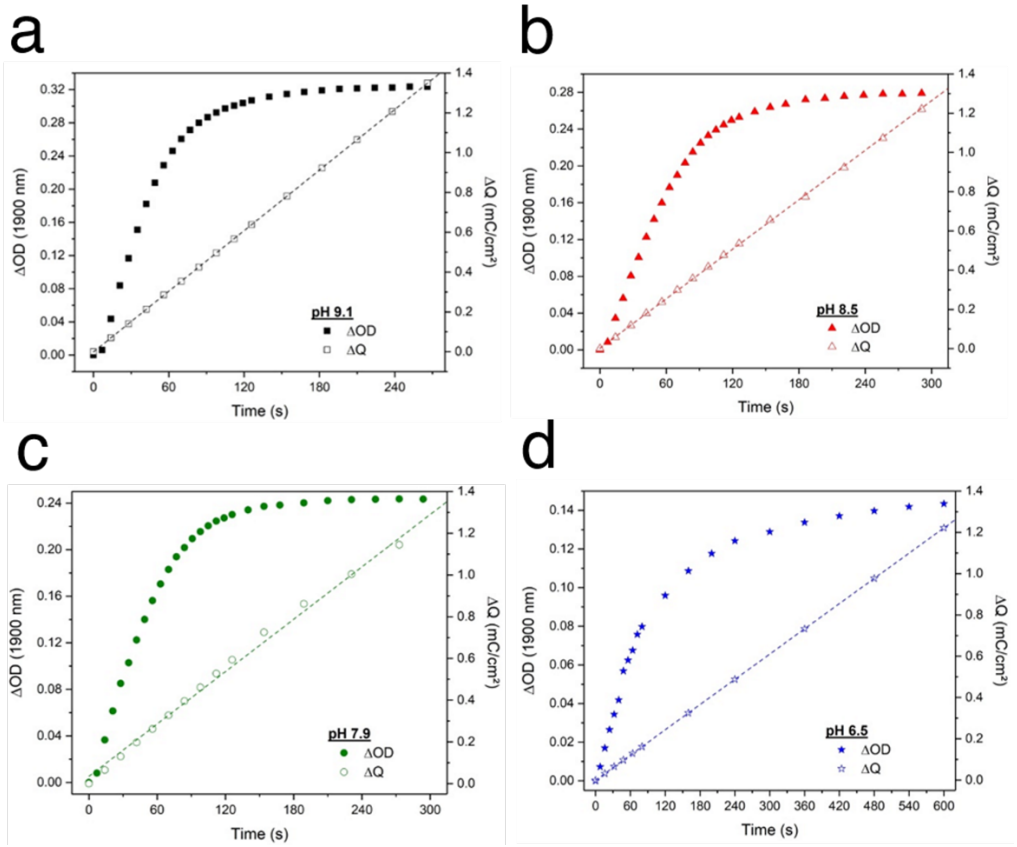

Figure A3.4: Evolution of differential optical density (ΔOD) and inserted charge density (ΔQ) as a function of time for PAA-mPEO$_4$-wrapped ITO films.

Film obtained from dispersion processed in: a) pH= 9.1 borate buffer, b) pH= 8.5 borate buffer, c) pH= 7.9 borate buffer, and d) pH= 6.5 Milli-Q water.

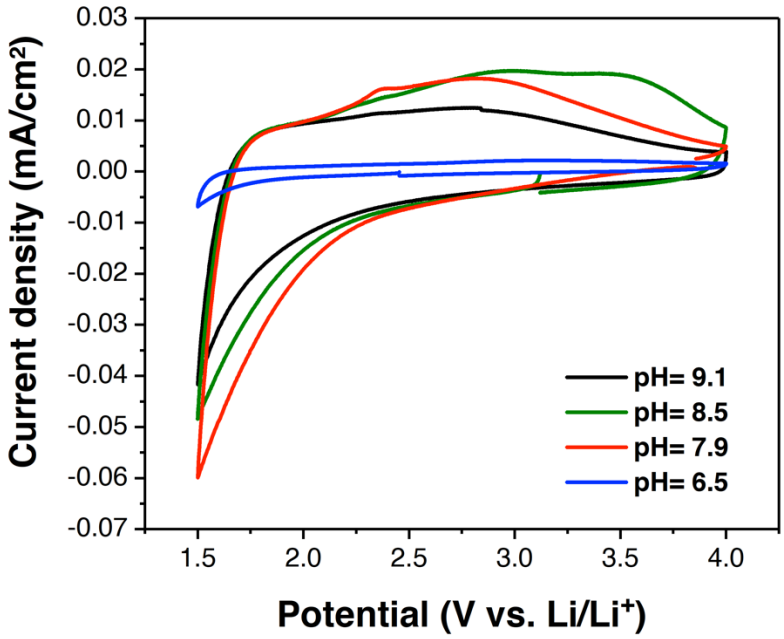

Figure A3.5: Cyclic voltammetry for PAA-mPEO$_4$-wrapped ITO films.

Cyclic voltammetry measurements were conducted in an Ar glovebox. PAA-mPEO$_4$-wrapped ITO films deposited on FTO glass (working electrode) and Li foil (counter and reference electrode) were immersed in 1 M LiTFSI in tetraglyme electrolyte in a quartz cuvette. Starting from open circuit potential, the applied bias (Bio-logic VMP3) was cycled between 4.0 and 1.5 V vs. Li/Li$^+$ at a scan rate of 20 mV/s.

References

(1) Agrawal, A.; Cho, S. H.; Zandi, O.; Ghosh, S.; Johns, R. W.; Milliron, D. J. Localized Surface Plasmon Resonance in Semiconductor Nanocrystals. *Chem. Rev.* **2018**, *118*, 3121–3207.

(2) Shamsi, J.; Urban, A. S.; Imran, M.; De Trizio, L.; Manna, L. Metal Halide Perovskite Nanocrystals: Synthesis, Post-Synthesis Modifications, and Their Optical Properties. *Chem. Rev.* **2019**, *119*, 3296–3348.

(3) Coughlan, C.; Ibáñez, M.; Dobrozhan, O.; Singh, A.; Cabot, A.; Ryan, K. M. Compound Copper Chalcogenide Nanocrystals. *Chem. Rev.* **2017**, *117*, 5865–6109.

(4) Liu, J.; Zhang, J. Nanointerface Chemistry: Lattice-Mismatch-Directed Synthesis and Application of Hybrid Nanocrystals. *Chem. Rev.* **2020**, *120*, 2123–2170.

(5) Glotzer, S. C.; Solomon, M. J.; Kotov, N. A. Self-Assembly: From Nanoscale to Microscale Colloids. *AIChE J.* **2004**, *50*, 2978–2985.

(6) Boles, M. A.; Engel, M.; Talapin, D. V. Self-Assembly of Colloidal Nanocrystals: From Intricate Structures to Functional Materials. *Chem. Rev.* **2016**, *116*, 11220–11289.

(7) Niederberger, M. Multiscale Nanoparticle Assembly: From Particulate Precise Manufacturing to Colloidal Processing. *Adv. Funct. Mater.* **2017**, *27*, 1–18.

(8) Isaacoff, B.; Brown, K. A. Progress in Top-Down Control of Bottom-Up Assembly. *Nano Lett.* **2017**, *17*, 6508–6510.

(9) Begley, M. R.; Gianola, D. S.; Ray, T. R. Bridging Functional Nanocomposites to Robust Macroscale Devices. *Science* **2019**, *364*, 1–8.

(10) Agrawal, A.; Singh, A.; Yazdi, S.; Singh, A.; Ong, G. K.; Bustillo, K.; Johns, R. W.; Ringe, E.; Milliron, D. J. Resonant Coupling Between Molecular Vibrations and Localized Surface Plasmon Resonance of Faceted Metal Oxide Nanocrystals. *Nano Lett.* **2017**, *17*, 2611–2620.

(11) Jiang, N.; Zhuo, X.; Wang, J. Active Plasmonics: Principles, Structures, and Applications. *Chem. Rev.* **2018**, *118*, 3054–3099.

(12) Ha, M.; Kim, J.-H.; You, M.; Li, Q.; Fan, C.; Nam, J.-M. Multicomponent Plasmonic Nanoparticles: From Heterostructured Nanoparticles to Colloidal Composite Nanostructures. *Chem. Rev.* **2019**, *119*, 12208–12278.

(13) Tikhomirov, G.; Hoogland, S.; Lee, P. E.; Fischer, A.; Sargent, E. H.; Kelley, S. O. DNA-Based Programming of Quantum Dot Valency, Self-Assembly and Luminescence. *Nat. Nanotechnol.* **2011**, *6*, 485–490.

(14) Pietryga, J. M.; Park, Y.-S.; Lim, J.; Fidler, A. F.; Bae, W. K.; Brovelli, S.; Klimov, V. I. Spectroscopic and Device Aspects of Nanocrystal Quantum Dots. *Chem. Rev.* **2016**, *116*, 10513–10622.

(15) Wolf, A.; Lesnyak, V.; Gaponik, N.; Eychmüller, A. Quantum-Dot-Based (Aero)Gels: Control of the Optical Properties. *J. Phys. Chem. Lett.* **2012**, *3*, 2188–2193.
(16) DeSario, P. A.; Pietron, J. J.; Dunkelberger, A.; Brintlinger, T. H.; Baturina, O.; Stroud, R. M.; Owrutsky, J. C.; Rolison, D. R. Plasmonic Aerogels as a Three-Dimensional Nanoscale Platform for Solar Fuel Photocatalysis. *Langmuir* **2017**, *33*, 9444–9454.
(17) Ma, K.; Yehezkeli, O.; He, L.; Cha, J. N. DNA for Assembly and Charge Transport Photocatalytic Reduction of CO_2. *Adv. Sustainable Syst.* **2018**, *2*, 1700156–1700159.
(18) Ma, K.; Yehezkeli, O.; Domaille, D. W.; Funke, H. H.; Cha, J. N. Enhanced Hydrogen Production From DNA-Assembled Z-Scheme TiO_2-CdS Photocatalyst Systems. *Angew. Chem. Int. Ed.* **2015**, *127*, 11652–11656.
(19) Luna, A. L.; Matter, F.; Schreck, M.; Wohlwend, J.; Tervoort, E.; Colbeau-Justin, C.; Niederberger, M. Monolithic Metal-Containing TiO_2 Aerogels Assembled From Crystalline Pre-Formed Nanoparticles as Efficient Photocatalysts for H_2 Generation. *Appl. Catal. B* **2020**, *267*, 1-10.
(20) Li, T.; Senesi, A. J.; Lee, B. Small Angle X-Ray Scattering for Nanoparticle Research. *Chem. Rev.* **2016**, *116*, 11128–11180.
(21) Ziegler, C.; Wolf, A.; Liu, W.; Herrmann, A.-K.; Gaponik, N.; Eychmüller, A. Modern Inorganic Aerogels. *Angew. Chem. Int. Ed.* **2017**, *56*, 13200–13221.
(22) Wen, D.; Eychmüller, A. 3D Assembly of Preformed Colloidal Nanoparticles Into Gels and Aerogels: Function-Led Design. *Chem. Comm.* **2017**, *53*, 12608–12621.
(23) Matter, F.; Luna, A. L.; Niederberger, M. From Colloidal Dispersions to Aerogels: How to Master Nanoparticle Gelation. *Nano Today* **2019**, 1–21.
(24) Poon, W. C. Phase Separation, Aggregation and Gelation in Colloid-Polymer Mixtures and Related Systems. *Curr. Opin. Colloid Interface Sci.* **1998**, *3*, 593–599.
(25) Lekkerkerker, H. N. W.; Tuinier, R. Introduction. In *Colloids and the Depletion Interaction*; Lecture Notes in Physics; Springer: Dordrecht, Netherlands, 2011; Vol. 833, pp 1–56.
(26) Kotov, N. A. Self-Assembly of Inorganic Nanoparticles: Ab Ovo. *Europhys Lett* **2017**, *119*, 1–6.
(27) Mallory, S. A.; Valeriani, C.; Cacciuto, A. An Active Approach to Colloidal Self-Assembly. *Annu. Rev. Phys. Chem.* **2018**, *69*, 59–79.
(28) Grzelczak, M.; Liz-Marzán, L. M.; Klajn, R. Stimuli-Responsive Self-Assembly of Nanoparticles. *Chem. Soc. Rev.* **2019**, *48*, 1342–1361.
(29) Grzybowski, B. A.; Fitzner, K.; Paczesny, J.; Granick, S. From Dynamic Self-Assembly to Networked Chemical Systems. *Chem. Soc. Rev.* **2017**, *46*, 5647–5678.
(30) Israelachvili, J. N. Electrostatic Forces Between Surfaces in Liquids. In *Intermolecular and Surface Forces*; Elsevier: Amsterdam, 2011; pp 291–340.

(31) Vincent, B.; Edwards, J.; Emmet, S.; Jones, A. Depletion Flocculation in Dispersions of Sterically-Stabilized Particles ("Soft Spheres"). *Colloids Surf.* **1986**, *18*, 261–281.
(32) Napper, D. H. Steric Stabilization. *J. Colloid Interface Sci.* **1976**, *58*, 390–407.
(33) De Gennes, P. G. Scaling Theory of Polymer Adsorption. *J. Phys. France* **1976**, *37*, 1445–1452.
(34) Israelachvili, J. N. Steric (Polymer-Mediated) and Thermal Fluctuation Forces. In *Intermolecular and Surface Forces*; Elsevier: Amsterdam, Netherlands, 2011; pp 381–413.
(35) Lekkerkerker, H. N. W.; Tuinier, R. Depletion Interaction. In *Colloids and the Depletion Interaction*; Lecture Notes in Physics; Springer: Dordrecht, Netherlands, 2011; Vol. 833, pp 57–108.
(36) Lekkerkerker, H. N. W.; Poon, W. C. K.; Pusey, P. N.; Stroobants, A.; Warren, P. B. Phase Behaviour of Colloid + Polymer Mixtures. *Europhys Lett* **1992**, *20*, 559–564.
(37) Zaccarelli, E. Colloidal Gels: Equilibrium and Non-Equilibrium Routes. *J. Phys.: Condens. Matter* **2007**, *19*, 323101–323151.
(38) Del Gado, E.; Fiocco, D.; Foffi, G.; Manley, S.; Trappe, V.; Zaccone, A. Colloidal Gelation. In *Fluids, Colloids and Soft Materials: An Introduction to Soft Matter Physics*; John Wiley & Sons, Ltd: Hoboken, New Jersey, 2016; Vol. 4, pp 279–291.
(39) Lazzari, S.; Nicoud, L.; Jaquet, B.; Lattuada, M.; Morbidelli, M. Fractal-Like Structures in Colloid Science. *Adv. Colloid Interface Sci.* **2016**, *235*, 1–13.
(40) Luo, J.; Yuan, G.; Zhao, C.; Han, C. C.; Chen, J.; Liu, Y. Gelation of Large Hard Particles with Short-Range Attraction Induced by Bridging of Small Soft Microgels. *Soft Matter* **2015**, *11*, 2494–2503.
(41) Martin, J. E.; Hurd, A. J. Scattering From Fractals. *J. Appl. Crystallogr.* **1987**, *20*, 61–78.
(42) Meakin, P. Reaction-Limited Cluster-Cluster Aggregation in Dimensionalities 2-10. *Phys. Rev. A* **1988**, *38*, 4799–4814.
(43) Lin, M. Y.; Lindsay, H. M.; Weitz, D. A.; Ball, R. C.; Klein, R.; Meakin, P. Universal Reaction-Limited Colloid Aggregation. *Phys. Rev. A* **1990**, *41*, 2005–2020.
(44) Lin, M. Y.; Lindsay, H. M.; Weitz, D. A.; Klein, R.; Pall, R. C.; Meakin, P. Universal Diffusion-Limited Colloid Aggregation. *J. Phys.: Condens. Matter* **1990**, *2*, 3093–3113.
(45) Lin, M. Y.; Lindsay, H. M.; Weitz, D. A.; Ball, R. C.; Klein, R.; Meakin, P. Universality in Colloid Aggregation. *Nature* **1989**, *339*, 1–3.
(46) Arachchige, I. U.; Mohanan, J. L.; Brock, S. L. Sol−Gel Processing of Semiconducting Metal Chalcogenide Xerogels: Influence of Dimensionality on Quantum Confinement Effects in a Nanoparticle Network. *Chem. Mater.* **2005**, *17*, 6644–6650.

(47) Arachchige, I. U.; Brock, S. L. Sol–Gel Methods for the Assembly of Metal Chalcogenide Quantum Dots. *Acc. Chem. Res.* **2007**, *40*, 801–809.
(48) Gacoin, T.; Lahlil, K.; Larregaray, P.; Boilot, J.-P. Transformation of CdS Colloids: Sols, Gels, and Precipitates. *J. Phys. Chem. B* **2001**, *105*, 10228–10235.
(49) Liu, W.; Herrmann, A.-K.; Bigall, N. C.; Rodriguez, P.; Wen, D.; Oezaslan, M.; Schmidt, T. J.; Gaponik, N.; Eychmüller, A. Noble Metal Aerogels—Synthesis, Characterization, and Application as Electrocatalysts. *Acc. Chem. Res.* **2015**, *48*, 154–162.
(50) Wen, D.; Liu, W.; Haubold, D.; Zhu, C.; Oschatz, M.; Holzschuh, M.; Wolf, A.; Simon, F.; Kaskel, S.; Eychmüller, A. Gold Aerogels: Three-Dimensional Assembly of Nanoparticles and Their Use as Electrocatalytic Interfaces. *ACS Nano* **2016**, *10*, 2559–2567.
(51) Singh, A.; Lindquist, B. A.; Ong, G. K.; Jadrich, R. B.; Singh, A.; Ha, H.; Ellison, C. J.; Truskett, T. M.; Milliron, D. J. Linking Semiconductor Nanocrystals Into Gel Networks Through All-Inorganic Bridges. *Angew. Chem. Int. Ed.* **2015**, *54*, 14840–14844.
(52) Sayevich, V.; Cai, B.; Benad, A.; Haubold, D.; Sonntag, L.; Gaponik, N.; Lesnyak, V.; Eychmüller, A. 3D Assembly of All-Inorganic Colloidal Nanocrystals Into Gels and Aerogels. *Angew. Chem. Int. Ed.* **2016**, *55*, 6334–6338.
(53) Lindquist, B. A.; Jadrich, R. B.; Milliron, D. J.; Truskett, T. M. On the Formation of Equilibrium Gels via a Macroscopic Bond Limitation. *J. Chem. Phys.* **2016**, *145*, 1–12
(54) Howard, M. P.; Jadrich, R. B.; Lindquist, B. A.; Khabaz, F.; Bonnecaze, R. T.; Milliron, D. J.; Truskett, T. M. Structure and Phase Behavior of Polymer-Linked Colloidal Gels. *J. Chem. Phys.* **2019**, *151*, 1249011–12490110.
(55) Marro, N.; Sala, della, F.; Kay, E. R. Programmable Dynamic Covalent Nanoparticle Building Blocks with Complementary Reactivity. *Chem. Sci.* **2020**, *11*, 372–383.
(56) Lesnyak, V.; Wolf, A.; Dubavik, A.; Borchardt, L.; Voitekhovich, S. V.; Gaponik, N.; Kaskel, S.; Eychmüller, A. 3D Assembly of Semiconductor and Metal Nanocrystals: Hybrid CdTe/Au Structures with Controlled Content. *J. Am. Chem. Soc.* **2011**, *133*, 13413–13420.
(57) Berestok, T.; Guardia, P.; Ibáñez, M.; Meyns, M.; Colombo, M.; Kovalenko, M. V.; Peiró, F.; Cabot, A. Electrostatic-Driven Gelation of Colloidal Nanocrystals. *Langmuir* **2018**, *34*, 9167–9174.
(58) Odziomek, M.; Chaput, F.; Lerouge, F.; Dujardin, C.; Sitarz, M.; Karpati, S.; Parola, S. From Nanoparticle Assembly to Monolithic Aerogels of YAG, Rare Earth Fluorides, and Composites. *Chem. Mater.* **2018**, *30*, 5460–5467.
(59) Talapin, D. V.; Lee, J.-S.; Kovalenko, M. V.; Shevchenko, E. V. Prospects of Colloidal Nanocrystals for Electronic and Optoelectronic Applications. *Chem. Rev.* **2010**, *110*, 389–458.

(60) Giannini, V.; Fernández-Domínguez, A. I.; Heck, S. C.; Maier, S. A. Plasmonic Nanoantennas: Fundamentals and Their Use in Controlling the Radiative Properties of Nanoemitters. *Chem. Rev.* **2011**, *111*, 3888–3912.
(61) Agrawal, A.; Johns, R. W.; Milliron, D. J. Control of Localized Surface Plasmon Resonances in Metal Oxide Nanocrystals. *Annu. Rev. Mater. Res.* **2017**, *47*, 1–31.
(62) Pu, C.; Qin, H.; Gao, Y.; Zhou, J.; Wang, P.; Peng, X. Synthetic Control of Exciton Behavior in Colloidal Quantum Dots. *J. Am. Chem. Soc.* **2017**, *139*, 3302–3311.
(63) Runnerstrom, E. L.; Llordés, A.; Lounis, S. D.; Milliron, D. J. Nanostructured Electrochromic Smart Windows: Traditional Materials and NIR-Selective Plasmonic Nanocrystals. *Chem. Commun.* **2014**, *50*, 10555–10572.
(64) Carey, G. H.; Abdelhady, A. L.; Ning, Z.; Thon, S. M.; Bakr, O. M.; Sargent, E. H. Colloidal Quantum Dot Solar Cells. *Chem. Rev.* **2015**, *115*, 12732–12763.
(65) Wang, Y.; Runnerstrom, E. L.; Milliron, D. J. Switchable Materials for Smart Windows. *Annu. Rev. Chem. Biomol. Eng.* **2016**, *7*, 283–304.
(66) Murray, C. B.; Kagan, A. C. R.; Bawendi, M. G. Synthesis and Characterization of Monodisperse Nanocrystals and Close-Packed Nanocrystal Assemblies. *Annu. Rev. of Mater. Sci.* **2000**, *30*, 545–610.
(67) Chen, C.-F.; Tzeng, S.-D.; Chen, H.-Y.; Lin, K.-J.; Gwo, S. Tunable Plasmonic Response From Alkanethiolate-Stabilized Gold Nanoparticle Superlattices: Evidence of Near-Field Coupling. *J. Am. Chem. Soc.* **2008**, *130*, 824–826.
(68) Wang, H.; Levin, C. S.; Halas, N. J. Nanosphere Arrays with Controlled Sub-10-Nm Gaps as Surface-Enhanced Raman Spectroscopy Substrates. *J. Am. Chem. Soc.* **2005**, *127*, 14992–14993.
(69) Zaccarelli, E.; Lu, P. J.; Ciulla, F.; Weitz, D. A.; Sciortino, F. Gelation as Arrested Phase Separation in Short-Ranged Attractive Colloid–Polymer Mixtures. *J. Phys.: Condens. Matter* **2008**, *20*, 1-8.
(70) Ruzicka, B.; Zaccarelli, E.; Zulian, L.; Angelini, R.; Sztucki, M.; Moussaïd, A.; Narayanan, T.; Sciortino, F. Observation of Empty Liquids and Equilibrium Gels in a Colloidal Clay. *Nat. Mater.* **2010**, *10*, 56–60.
(71) Sciortino, F.; Tartaglia, P.; Zaccarelli, E. One-Dimensional Cluster Growth and Branching Gels in Colloidal Systems with Short-Range Depletion Attraction and Screened Electrostatic Repulsion. *J. Phys. Chem. B* **2005**, *109*, 21942–21953.
(72) Korala, L.; Brock, S. L. Aggregation Kinetics of Metal Chalcogenide Nanocrystals: Generation of Transparent CdSe (ZnS) Core (Shell) Gels. *J. Phys. Chem. C* **2012**, *116*, 17110–17117.
(73) Yu, H.; Liu, Y.; Brock, S. L. Tuning the Optical Band Gap of Quantum Dot Assemblies by Varying Network Density. *ACS Nano* **2009**, *3*, 2000–2006.
(74) Herrmann, A.-K.; Formanek, P.; Borchardt, L.; Klose, M.; Giebeler, L.; Eckert, J.; Kaskel, S.; Gaponik, N.; Eychmüller, A. Multimetallic Aerogels by

Template-Free Self-Assembly of Au, Ag, Pt, and Pd Nanoparticles. *Chem. Mater.* **2014**, *26*, 1074–1083.
(75) Bigall, N. C.; Herrmann, A.-K.; Vogel, M.; Rose, M.; Simon, P.; Cabrera, W. C.; Dorfs, D.; Kaskel, S.; Gaponik, N.; Eychmüller, A. Hydrogels and Aerogels From Noble Metal Nanoparticles. *Angew. Chem. Int. Ed.*, *48*, 9731–9734.
(76) Naskar, S.; Freytag, A.; Deutsch, J.; Wendt, N.; Behrens, P.; Köckritz, A.; Bigall, N. C. Porous Aerogels From Shape-Controlled Metal Nanoparticles Directly From Nonpolar Colloidal Solution. *Chem. Mater.* **2017**, *29*, 9208–9217.
(77) Nahar, L.; Farghaly, A. A.; Esteves, R. J. A.; Arachchige, I. U. Shape Controlled Synthesis of Au/Ag/Pd Nanoalloys and Their Oxidation-Induced Self-Assembly Into Electrocatalytically Active Aerogel Monoliths. *Chem. Mater.* **2017**, *29*, 7704–7715.
(78) Mohanan, J. L.; Arachchige, I. U.; Brock, S. L. Porous Semiconductor Chalcogenide Aerogels. *Science* **2005**, *307*, 397–400.
(79) Kalebaila, K. K.; Brock, S. L. Lead Selenide Nanostructured Aerogels and Xerogels. *Z. Anorg. Allg. Chem.* **2012**, *638*, 2598–2603.
(80) Anderson, M. L.; Morris, C. A.; Stroud, R. M.; Merzbacher, C. I.; Rolison, D. R. Colloidal Gold Aerogels: Preparation, Properties, and Characterization. *Langmuir* **1999**, *15*, 674–681.
(81) Polleux, J.; Pinna, N.; Antonietti, M.; Niederberger, M. Ligand-Directed Assembly of Preformed Titania Nanocrystals Into Highly Anisotropic Nanostructures. *Adv. Mater.* **2004**, *16*, 436–439.
(82) Rechberger, F.; Heiligtag, F. J.; Süess, M. J.; Niederberger, M. Assembly of $BaTiO_3$ Nanocrystals Into Macroscopic Aerogel Monoliths with High Surface Area. *Angew. Chem. Int. Ed.* **2014**, *53*, 6823–6826.
(83) Rechberger, F.; Mercandetti, C.; Tervoort, E.; Niederberger, M. Colloidal Nanocrystal-Based BaTiO3 Xerogels as Green Bodies: Effect of Drying and Sintering at Low Temperatures on Pore Structure and Microstructures. *Langmuir* **2017**, *33*, 280–287.
(84) Rechberger, F.; Tervoort, E.; Niederberger, M. Nonaqueous Sol-Gel Synthesis of $InTaO_4$ Nanoparticles and Their Assembly Into Macroscopic Aerogels. *J. Am. Ceram. Soc.* **2017**, *100*, 4483–4490.
(85) Heiligtag, F. J.; Rossell, M. D.; Süess, M. J.; Niederberger, M. Template-Free Co-Assembly of Preformed Au and TiO_2 Nanoparticles Into Multicomponent 3D Aerogels. *J. Mater. Chem.* **2011**, *21*, 16893–16899.
(86) Heiligtag, F. J.; Kränzlin, N.; Süess, M. J.; Niederberger, M. Anatase-Silica Composite Aerogels: a Nanoparticle-Based Approach. *J. Sol-Gel Sci. Technol.* **2014**, *70*, 300–306.
(87) Heiligtag, F. J.; Cheng, W.; de Mendonça, V. R.; Süess, M. J.; Hametner, K.; Günther, D.; Ribeiro, C.; Niederberger, M. Self-Assembly of Metal and Metal Oxide Nanoparticles and Nanowires Into a Macroscopic Ternary Aerogel

Monolith with Tailored Photocatalytic Properties. *Chem. Mater.* **2014**, *26*, 5576–5584.
(88) Cheng, W.; Rechberger, F.; Niederberger, M. From 1D to 3D-Macroscopic Nanowire Aerogel Monoliths. *Nanoscale* **2016**, *8*, 14074–14077.
(89) Cheng, W.; Rechberger, F.; Niederberger, M. Three-Dimensional Assembly of Yttrium Oxide Nanosheets Into Luminescent Aerogel Monoliths with Outstanding Adsorption Properties. *ACS Nano* **2016**, *10*, 2467–2475.
(90) Bergenholtz, J.; Poon, W. C. K.; Fuchs, M. Gelation in Model Colloid−Polymer Mixtures. *Langmuir* **2003**, *19*, 4493–4503.
(91) Verhaegh, N. A. M.; Asnaghi, D.; Lekkerkerker, H. N. W.; Giglio, M.; Cipelletti, L. Transient Gelation by Spinodal Decomposition in Colloid-Polymer Mixtures. *Physica A* **1997**, *242*, 104–118.
(92) de Kruif, C. G.; Tuinier, R. Polysaccharide Protein Interactions. *Food Hydrocoll.* **2001**, *15*, 555–563.
(93) Johnston, K. P.; Maynard, J. A.; Truskett, T. M.; Borwankar, A. U.; Miller, M. A.; Wilson, B. K.; Dinin, A. K.; Khan, T. A.; Kaczorowski, K. J. Concentrated Dispersions of Equilibrium Protein Nanoclusters That Reversibly Dissociate Into Active Monomers. *ACS Nano* **2012**, *6*, 1357–1369.
(94) Kulkarni, A.; Zukoski, C. Depletion Interactions and Protein Crystallization. *J. Cryst. Growth* **2001**, *232*, 156–164.
(95) Whitelam, S. Control of Pathways and Yields of Protein Crystallization Through the Interplay of Nonspecific and Specific Attractions. *Phys. Rev. Lett.* **2010**, *105*, 088102.
(96) Jadrich, R. B.; Bollinger, J. A.; Johnston, K. P.; Truskett, T. M. Origin and Detection of Microstructural Clustering in Fluids with Spatial-Range Competitive Interactions. *Phys. Rev. E* **2015**, *91*, 1-6.
(97) Akselrod, G. M.; Weidman, M. C.; Li, Y.; Argyropoulos, C.; Tisdale, W. A.; Mikkelsen, M. H. Efficient Nanosecond Photoluminescence From Infrared PbS Quantum Dots Coupled to Plasmonic Nanoantennas. *ACS Photonics* **2016**, *3*, 1741–1746.
(98) Choi, S.-I.; Nam, K. M.; Park, B. K.; Seo, W. S.; Park, J. T. Preparation and Optical Properties of Colloidal, Monodisperse, and Highly Crystalline ITO Nanoparticles. *Chem. Mater.* **2008**, *20*, 2609–2611.
(99) Kanehara, M.; Koike, H.; Yoshinaga, T.; Teranishi, T. Indium Tin Oxide Nanoparticles with Compositionally Tunable Surface Plasmon Resonance Frequencies in the Near-IR Region. *J. Am. Chem. Soc.* **2009**, *131*, 17736–17737.
(100) Dong, A.; Ye, X.; Chen, J.; Kang, Y.; Gordon, T.; Kikkawa, J. M.; Murray, C. B. A Generalized Ligand-Exchange Strategy Enabling Sequential Surface Functionalization of Colloidal Nanocrystals. *J. Am. Chem. Soc.* **2011**, *133*, 998–1006.
(101) Hexemer, A.; Bras, W.; Glossinger, J.; Schaible, E.; Gann, E.; Kirian, R.; MacDowell, A.; Church, M.; Rude, B.; Padmore, H. A SAXS/WAXS/GISAXS

Beamline with Multilayer Monochromator. *J. Phys.: Conf. Ser.* **2010**, *247*, 1–11.
(102) Ilavsky, J. Nika: Software for Two-Dimensional Data Reduction. *J. Appl. Crystallogr.* **2012**, *45*, 324–328.
(103) Ilavsky, J.; Jemian, P. R. Irena: Tool Suite for Modeling and Analysis of Small-Angle Scattering. *J. Appl. Crystallogr.* **2009**, *42*, 347–353.
(104) Safar, M.; Bertrand, D.; Robert, P.; Devaux, M. F.; Genot, C. Characterization of Edible Oils, Butters and Margarines by Fourier Transform Infrared Spectroscopy with Attenuated Total Reflectance. *J. Am. Oil Chem. Soc.* **1994**, *71*, 371–377.
(105) Rosen, E. L.; Buonsanti, R.; Llordés, A.; Sawvel, A. M.; Milliron, D. J.; Helms, B. A. Exceptionally Mild Reactive Stripping of Native Ligands From Nanocrystal Surfaces by Using Meerwein's Salt. *Angew. Chem. Int. Ed.* **2012**, *51*, 684–689.
(106) Devanand, K.; Selser, J. C. Asymptotic Behavior and Long-Range Interactions in Aqueous Solutions of Poly(Ethylene Oxide). *Macromolecules* **1991**, *24*, 5943–5947.
(107) Liu, Y.; Porcar, L.; Chen, J.; Chen, W.-R.; Falus, P.; Faraone, A.; Fratini, E.; Hong, K.; Baglioni, P. Lysozyme Protein Solution with an Intermediate Range Order Structure. *J. Phys. Chem. B* **2011**, *115*, 7238–7247.
(108) Ong, G. K.; Williams, T. E.; Singh, A.; Schaible, E.; Helms, B. A.; Milliron, D. J. Ordering in Polymer Micelle-Directed Assemblies of Colloidal Nanocrystals. *Nano Lett.* **2015**, *15*, 8240–8244.
(109) Lu, P. J.; Zaccarelli, E.; Ciulla, F.; Schofield, A. B.; Sciortino, F.; Weitz, D. A. Gelation of Particles with Short-Range Attraction. *Nature* **2008**, *453*, 499–504.
(110) Carpineti, M.; Giglio, M. Spinodal-Type Dynamics in Fractal Aggregation of Colloidal Clusters. *Phys. Rev. Lett.* **1992**, *68*, 3327–3330.
(111) Manley, S.; Wyss, H. M.; Miyazaki, K.; Conrad, J. C.; Trappe, V.; Kaufman, L. J.; Reichman, D. R.; Weitz, D. A. Glasslike Arrest in Spinodal Decomposition as a Route to Colloidal Gelation. *Phys. Rev. Lett.* **2005**, *95*, 1-4.
(112) Beaucage, G. Approximations Leading to a Unified Exponential/Power-Law Approach to Small-Angle Scattering. *J. Appl. Crystallogr.* **1995**, *28*, 717–728.
(113) Beaucage, G. Small-Angle Scattering From Polymeric Mass Fractals of Arbitrary Mass-Fractal Dimension. *J. Appl. Crystallogr.* **1996**, *29*, 134–146.
(114) Beaucage, G. Combined Small-Angle Scattering for Characterization of Hierarchically Structured Polymer Systems Over Nano-to-Micron Meter. In *Polymer Science: A Comprehensive Reference*; Elsevier: Amsterdam, 2012; pp 399–409.
(115) Jullien, R.; Kolb, M. Hierarchical Model for Chemically Limited Cluster-Cluster Aggregation. *J. Phys. A: Math. Gen.* **1984**, *17*, L639–L643.
(116) Brown, W. D.; Ball, R. C. Computer Simulation of Chemically Limited Aggregation. *J. Phys. A: Math. Gen.* **1985**, *18*, L517–L521.

(117) Beaucage, G.; Kammler, H. K.; Pratsinis, S. E. Particle Size Distributions From Small-Angle Scattering Using Global Scattering Functions. *J. Appl. Crystallogr.* **2004**, *37*, 523–535.
(118) Zhang, J.; Huang, F.; Lin, Z. Progress of Nanocrystalline Growth Kinetics Based on Oriented Attachment. *Nanoscale* **2010**, *2*, 18–34.
(119) Niederberger, M.; Colfen, H. Oriented Attachment and Mesocrystals: Non-Classical Crystallization Mechanisms Based on Nanoparticle Assembly. *Phys. Chem. Chem. Phys.* **2006**, *8*, 3271–3287.
(120) Mathur, S.; Moudgil, B. M. Adsorption Mechanism(S) of Poly(Ethylene Oxide) on Oxide Surfaces. *J. Colloid Interface Sci.* **1997**, *196*, 92–98.
(121) Lafuma, F.; Wong, K.; Cabane, B. Bridging of Colloidal Particles Through Adsorbed Polymers. *J. Colloid Interface Sci.* **1991**, *143*, 9–21.
(122) Wong, K.; Lixon, P.; Lafuma, F.; Lindner, P.; Charriol, O. A.; Cabane, B. Intermediate Structures in Equilibrium Flocculation. *J. Colloid Interface Sci.* **1992**, *153*, 55–72.
(123) Zhao, C.; Yuan, G.; Jia, D.; Han, C. C. Macrogel Induced by Microgel: Bridging and Depletion Mechanisms. *Soft Matter* **2012**, *8*, 7036–7040.
(124) Lowen, H.; Roux, J. N.; Hansen, J. P. Mapping of Charge Polydispersity Onto Size Polydispersity in Colloidal Suspensions. *J. Phys.: Condens. Matter* **1991**, *3*, 997–1002.
(125) Gögelein, C. *Phase Behaviour of Proteins and Colloid Polymer Mixtures*; Forschungszentrum: Jülich, Germany, 2008.
(126) Jain, P. K.; Huang, W.; El-Sayed, M. A. On the Universal Scaling Behavior of the Distance Decay of Plasmon Coupling in Metal Nanoparticle Pairs: a Plasmon Ruler Equation. *Nano Lett.* **2007**, *7*, 2080–2088.
(127) Lin, S.; Li, M.; Dujardin, E.; Girard, C.; Mann, S. One-Dimensional Plasmon Coupling by Facile Self-Assembly of Gold Nanoparticles Into Branched Chain Networks. *Adv. Mater.* **2005**, *17*, 2553–2559.
(128) Barrow, S. J.; Funston, A. M.; Gómez, D. E.; Davis, T. J.; Mulvaney, P. Surface Plasmon Resonances in Strongly Coupled Gold Nanosphere Chains From Monomer to Hexamer. *Nano Lett.* **2011**, *11*, 4180–4187.
(129) Agrawal, A.; Kriegel, I.; Milliron, D. J. Shape-Dependent Field Enhancement and Plasmon Resonance of Oxide Nanocrystals. *J. Phys. Chem. C* **2015**, *119*, 6227–6238.
(130) Kim, J.; Dutta, A.; Memarzadeh, B.; Kildishev, A. V.; Mosallaei, H.; Boltasseva, A. Zinc Oxide Based Plasmonic Multilayer Resonator: Localized and Gap Surface Plasmon in the Infrared. *ACS Photonics* **2015**, *2*, 1224–1230.
(131) Willets, K. A.; Van Duyne, R. P. Localized Surface Plasmon Resonance Spectroscopy and Sensing. *Annu. Rev. Phys. Chem.* **2007**, *58*, 267–297.
(132) Bayliss, K.; van Duijneveldt, J. S.; Faers, M. A.; Vermeer, A. W. P. Comparing Colloidal Phase Separation Induced by Linear Polymer and by Microgel Particles. *Soft Matter* **2011**, *7*, 10345–10348.

(133) Buzzaccaro, S.; Piazza, R.; Colombo, J.; Parola, A. Enhancement of Depletion Forces by Electrostatic Depletant Repulsion. *J. Chem. Phys.* **2010**, *132*, 124902–124916.
(134) Buzzaccaro, S.; Colombo, J.; Parola, A.; Piazza, R. Critical Depletion. *Phys. Rev. Lett.* **2010**, *105*, 1983011–1983014.
(135) Hobbie, E. K.; Stewart, A. D. Internal Dynamics and Elasticity of Confined Entropic Gels. *Phys. Rev. E* **2000**, *61*, 5540–5544.
(136) Cheng, L.-C.; Sherman, Z. M.; Swan, J. W.; Doyle, P. S. Colloidal Gelation Through Thermally Triggered Surfactant Displacement. *Langmuir* **2019**, *35*, 9464–9473.
(137) Mason, T. G. Osmotically Driven Shape-Dependent Colloidal Separations. *Phys. Rev. E* **2002**, *66*, 493–494.
(138) Park, K.; Koerner, H.; Vaia, R. A. Depletion-Induced Shape and Size Selection of Gold Nanoparticles. *Nano Lett.* **2010**, *10*, 1433–1439.
(139) Chang, H.-Y.; Huang, C.-W.; Chen, Y.-F.; Chen, S.-Y.; Sheng, Y.-J.; Tsao, H.-K. Assembly of Lock-and-Key Colloids Mediated by Polymeric Depletant. *Langmuir* **2015**, *31*, 13085–13093.
(140) Rossi, L.; Sacanna, S.; Irvine, W. T. M.; Chaikin, P. M.; Pine, D. J.; Philipse, A. P. Cubic Crystals From Cubic Colloids. *Soft Matter* **2011**, *7*, 4139–4142.
(141) Kim, J.; Song, X.; Ji, F.; Luo, B.; Ice, N. F.; Liu, Q.; Zhang, Q.; Chen, Q. Polymorphic Assembly From Beveled Gold Triangular Nanoprisms. *Nano Lett.* **2017**, *17*, 3270–3275.
(142) Henzie, J. Self-Assembly of Uniform Polyhedral Silver Nanocrystals Into Densest Packings and Exotic Superlattices. *Nat. Mater.* **2011**, *11*, 131–137.
(143) Saez Cabezas, C. A.; Ong, G. K.; Jadrich, R. B.; Lindquist, B. A.; Agrawal, A.; Truskett, T. M.; Milliron, D. J. Gelation of Plasmonic Metal Oxide Nanocrystals by Polymer-Induced Depletion Attractions. *Proc. Natl. Acad. Sci. USA* **2018**, *115*, 8925–8930.
(144) Yu, W. W.; Falkner, J. C.; Yavuz, C. T.; Colvin, V. L. Synthesis of Monodisperse Iron Oxide Nanocrystals by Thermal Decomposition of Iron Carboxylate Salts. *Chem Comm* **2004**, *20*, 2306–2307.
(145) Jansons, A. W.; Hutchison, J. E. Continuous Growth of Metal Oxide Nanocrystals: Enhanced Control of Nanocrystal Size and Radial Dopant Distribution. *ACS Nano* **2016**, *10*, 6942–6951.
(146) Cho, S. H.; Roccapriore, K. M.; Dass, C. K.; Ghosh, S.; Choi, J.; Noh, J.; Reimnitz, L. C.; Heo, S.; Kim, K.; Xie, K.; Korgel, B. A.; Li, X.; Hendrickson, J. R.; Hachtel, J. A.; Milliron, D. J. Spectrally Tunable Infrared Plasmonic F,Sn:in_2O_3 Nanocrystal Cubes. *J. Chem. Phys.* **2020**, *152*, 0147091–01470917.
(147) Heo, S.; Kim, J.; Ong, G. K.; Milliron, D. J. Template-Free Mesoporous Electrochromic Films on Flexible Substrates From Tungsten Oxide Nanorods. *Nano Lett.* **2017**, *17*, 5756–5761.

(148) Saunders, A. E.; Korgel, B. A. Second Virial Coefficient Measurements of Dilute Gold Nanocrystal Dispersions Using Small-Angle X-Ray Scattering. *J. Phys. Chem. B* **2004**, *108*, 16732–16738.
(149) Schaefer, D. W.; Keefer, K. D. Structure of Random Porous Materials: Silica Aerogels. *Phys. Rev. Lett.* **1986**, *56*, 2199–2202.
(150) Lattuada, M.; Wu, H.; Morbidelli, M. Estimation of Fractal Dimension of Colloidal Gels in the Presence of Multiple Scattering. *Phys. Rev. E* **2001**, *64*, 2371–2377.
(151) Valadez-Pérez, N. E.; Liu, Y.; Eberle, A. P. R.; Wagner, N. J.; Castañeda-Priego, R. Dynamical Arrest in Adhesive Hard-Sphere Dispersion Driven by Rigidity Percolation. *Phys. Rev. Lett.* **1985**, *54*, 2107–2110.
(152) Kline, S. R.; Kaler, E. W. Interactions in Colloidal Mixtures: Partial Structure Factors in Mixtures of Colloidal Silica and an Anionic Oil-in-Water Microemulsion. *J. Colloid Interface Sci.* **1998**, *203*, 392–401.
(153) González García, Á.; Opdam, J.; Tuinier, R. Phase Behaviour of Colloidal Superballs Mixed with Non-Adsorbing Polymers. *Eur. Phys. J. E* **2018**, *41*, 1–15.
(154) Garcia, G.; Buonsanti, R.; Runnerstrom, E. L.; Mendelsberg, R. J.; Llordés, A.; Anders, A.; Richardson, T. J.; Milliron, D. J. Dynamically Modulating the Surface Plasmon Resonance of Doped Semiconductor Nanocrystals. *Nano Lett.* **2011**, *11*, 4415–4420.
(155) Garcia, G.; Buonsanti, R.; Llordés, A.; Runnerstrom, E. L.; Bergerud, A.; Milliron, D. J. Near-Infrared Spectrally Selective Plasmonic Electrochromic Thin Films. *Adv. Opt. Mater.* **2013**, *1*, 215–220.
(156) Granqvist, C. G. Electrochromics for Smart Windows: Oxide-Based Thin Films and Devices. *Thin Solid Films* **2014**, *564*, 1–38.
(157) Kriegel, I.; Scotognella, F.; Manna, L. Plasmonic Doped Semiconductor Nanocrystals: Properties, Fabrication, Applications and Perspectives. *Phys. Rep.* **2017**, *674*, 1–52.
(158) Wang, Z.; Wang, X.; Cong, S.; Geng, F.; Zhao, Z. Fusing Electrochromic Technology with Other Advanced Technologies: a New Roadmap for Future Development. *Mat. Sci. Eng. R* **2019**, *140*, 1–26.
(159) Maho, A.; Lamela, L. C.; Henrist, C.; Henrard, L.; Tizei, L. H. G.; Kociak, M.; Stéphan, O.; Heo, S.; Milliron, D. J.; Vertruyen, B.; Cloots, R. Solvothermally-Synthesized Tin-Doped Indium Oxide Plasmonic Nanocrystals Spray-Deposited Onto Glass as Near-Infrared Electrochromic Films. *Sol. Energy Mater. Sol. Cells* **2019**, *200*, 1–9.
(160) Zandi, O.; Agrawal, A.; Shearer, A. B.; Reimnitz, L. C.; Dahlman, C. J.; Staller, C. M.; Milliron, D. J. Impacts of Surface Depletion on the Plasmonic Properties of Doped Semiconductor Nanocrystals. *Nat. Mater.* **2019**, *17*, 710–717.

(161) Li, X.; Perera, K.; He, J.; Gumyusenge, A.; Mei, J. Solution-Processable Electrochromic Materials and Devices: Roadblocks and Strategies Towards Large-Scale Applications. *J. Mater. Chem. C* **2019**, *7*, 12761–12789.
(162) Wang, Y.; Kim, J.; Gao, Z.; Zandi, O.; Heo, S.; Banerjee, P.; Milliron, D. J. Disentangling Photochromism and Electrochromism by Blocking Hole Transfer at the Electrolyte Interface. *Chem. Mater.* **2016**, *28*, 7198–7202.
(163) Kumar, N.; Lee, H. B.; Hwang, S.; Kim, T.-W.; Kang, J.-W. Fabrication of Plasmonic Gold-Nanoparticle-Transition Metal Oxides Thin Films for Optoelectronic Applications. *J. Alloys Compd.* **2019**, *775*, 39–50.
(164) Huang, J.; Liu, W.; Dolzhnikov, D. S.; Protesescu, L.; Kovalenko, M. V.; Koo, B.; Chattopadhyay, S.; Shenchenko, E. V.; Talapin, D. V. Surface Functionalization of Semiconductor and Oxide Nanocrystals with Small Inorganic Oxoanions (PO_4^{3-}, MoO_4^{2-}) And Polyoxometalate Ligands. *ACS Nano* **2014**, *8*, 9388–9402.
(165) Llordés, A.; Hammack, A. T.; Buonsanti, R.; Tangirala, R.; Aloni, S.; Helms, B. A.; Milliron, D. J. Polyoxometalates and Colloidal Nanocrystals as Building Blocks for Metal Oxide Nanocomposite Films. *J. Mater. Chem.* **2011**, *21*, 11631–11638.
(166) Duong, J. T.; Bailey, M. J.; Pick, T. E.; McBride, P. M.; Rosen, E. L.; Buonsanti, R.; Milliron, D. J.; Helms, B. A. Efficient Polymer Passivation of Ligand-Stripped Nanocrystal Surfaces. *J. Polym. Sci. A Polym. Chem.* **2012**, *50*, 3719–3727.
(167) Mendelsberg, R. J.; McBride, P. M.; Duong, J. T.; Bailey, M. J.; Llordés, A.; Milliron, D. J.; Helms, B. A. Dispersible Plasmonic Doped Metal Oxide Nanocrystal Sensors That Optically Track Redox Reactions in Aqueous Media with Single-Electron Sensitivity. *Adv. Opt. Mater.* **2015**, *3*, 1293–1300.
(168) Guhrenz, C.; Sayevich, V.; Weigert, F.; Hollinger, E.; Reichhelm, A.; Resch-Genger, U.; Gaponik, N.; Eychmüller, A. Transfer of Inorganic-Capped Nanocrystals Into Aqueous Media. *J. Phys. Chem. Lett.* **2017**, *8*, 5573–5578.
(169) Na, H.-K.; Kim, H.; Son, J. G.; Lee, J. H.; Kim, J.-K.; Park, J.; Lee, T. G. Facile Synthesis and Direct Characterization of Surface-Charge-Controlled Magnetic Iron Oxide Nanoparticles and Their Role in Gene Transfection in Human Leukemic T Cell. *Appl. Surf. Sci.* **2019**, *483*, 1069–1080.
(170) Llordés, A.; Garcia, G.; Gazquez, J.; Milliron, D. J. Tunable Near-Infrared and Visible-Light Transmittance in Nanocrystal-in-Glass Composites. *Nature* **2013**, *500*, 323–326.
(171) Llordés, A.; Wang, Y.; Fernandez-Martinez, A.; Xiao, P.; Lee, T.; Poulain, A.; Zandi, O.; Saez Cabezas, C. A.; Henkelman, G.; Milliron, D. J. Linear Topology in Amorphous Metal Oxide Electrochromic Networks Obtained via Low-Temperature Solution Processing. *Nat. Mater.* **2016**, *15*, 1267–1273.
(172) DeLongchamp, D. M.; Hammon, P. T. Highly Ion Conductive Poly(Ethylene Oxide)-Based Solid Polymer Electrolytes From Hydrogen Bonding Layer-by-Layer Assembly. *Langmuir* **2004**, *20*, 5403–5411.

(173) An, S. Y.; Jeong, I. C.; Won, M.-S.; Jeong, E. D.; Shim, Y.-B. Effect of Additives in PEO/PAA/PMAA Composite Solid Polymer Electrolytes on the Ionic Conductivity and Li Ion Battery Performance. *J. Appl. Electrochem.* **2009**, *39*, 1573–1578.
(174) Xue, Z.; He, D.; Xie, X. Poly(Ethylene Oxide)-Based Electrolytes for Lithium-Ion Batteries. *J. Mater. Chem. A* **2015**, *3*, 19218–19253.
(175) Bailey, M. J.; van der Weegen, R.; Klemm, P. J.; Baker, S. L.; Helms, B. A. Stealth Rare Earth Oxide Nanodiscs for Magnetic Resonance Imaging. *Adv. Healthc. Mater.* **2012**, *1*, 437–442.
(176) Su, Y.-L.; Wang, J.; Liu, H.-Z. FTIR Spectroscopic Study on Effects of Temperature and Polymer Composition on the Structural Properties of PEO-PPO-PEO Block Copolymer Micelles. *Langmuir* **2002**, *18*, 5370–5374.
(177) Dong, J.; Ozaki, Y.; Nakashima, K. Infrared, Raman, and Near-Infrared Spectroscopic Evidence for the Coexistence of Various Hydrogen-Bond Forms in Poly(Acrylic Acid). *Macromolecules* **1997**, *30*, 1111–1117.
(178) Kirwan, L. J.; Fawell, P. D.; van Bronswijk, W. In Situ FTIR-ATR Examination of Poly(Acrylic Acid) Adsorbed Onto Hematite at Low pH. *Langmuir* **2003**, *19*, 5802–5807.
(179) Bronstein, L. M.; Huang, X.; Retrum, J.; Schmuker, A.; Pink, M.; Stein, B. D.; Dragnea, B. Influence of Iron Oleate Complex Structure on Iron Oxide Nanoparticle Formation. *Chem. Mater.* **2007**, *19*, 3624–3632.
(180) Pramanik, N. C.; Das, S.; Biswas, P. K. The Effect of Sn(IV) on Transformation of Co-Precipitated Hydrated in(III) and Sn(IV) Hydroxides to Indium Tin Oxide (ITO) Powder. *Mater. Lett.* **2002**, *56*, 671–679.
(181) Su, C.; Suarez, D. L. Coordination of Adsorbed Boron: a FTIR Spectroscopic Study. *Environ. Sci. Technol.* **1995**, *29*, 302–311.
(182) Jun, L.; Shuping, X.; Shiyan, G. FT-IR and Raman Spectroscopic Study of Hydrated Borates. *Spectrochim. Acta* **1994**, *51A*, 519–532.
(183) Peak, D.; Luther, G. W., III; Sparks, D. L. ATR-FTIR Spectroscopic Studies of Boric Acid Adsorption on Hydrous Ferric Oxide. *Geochim. Cosmochim. Acta* **2003**, *67*, 2551–2560.
(184) Owen, B. B. The Dissociation Constant of Boric Acid From 10 to 50°. *J. Am. Chem. Soc.* **1934**, *56*, 1695–1967.
(185) Pattathil, P.; Giannuzzi, R.; Manca, M. Self-Powered NIR-Selective Dynamic Windows Based on Broad Tuning of the Localized Surface Plasmon Resonance in Mesoporous ITO Electrodes. *Nano Energy* **2016**, *30*, 242–251.
(186) Williams, T. E.; Chang, C. M.; Rosen, E. L.; Garcia, G.; Runnerstrom, E. L.; Williams, B. L.; Koo, B.; Buonsanti, R.; Milliron, D. J.; Helms, B. A. NIR-Selective Electrochromic Heteromaterial Frameworks: a Platform to Understand Mesoscale Transport Phenomena in Solid-State Electrochemical Devices. *J. Mater. Chem. C* **2014**, *2*, 3328–3328.

(187) Thoniyot, P.; Tan, M. J.; Karim, A. A.; Young, D. J.; Loh, X. J. Nanoparticle-Hydrogel Composites: Concept, Design, and Applications of These Promising, Multi-Functional Materials. *Adv. Sci.* **2015**, *2*, 1400010–1400013.
(188) Karg, M.; Pich, A.; Hellweg, T.; Hoare, T.; Lyon, L. A.; Crassous, J. J.; Suzuki, D.; Gumerov, R. A.; Schneider, S.; Potemkin, I. I.; Richtering, W. Nanogels and Microgels: From Model Colloids to Applications, Recent Developments, and Future Trends. *Langmuir* **2019**, *35*, 6231–6255.
(189) Cheng, C.; Zhang, C.; Wang, D. Using Hydrogel to Diversify the Adaptability and Applicability of Functional Nanoparticles: From Nanotech-Flavored Jellies to Artificial Enzymes. *Langmuir* **2019**, *35*, 8612–8628.
(190) Cheng, H.; Lin, S.; Muhammad, F.; Lin, Y.-W.; Wei, H. Rationally Modulate the Oxidase-Like Activity of Nanoceria for Self-Regulated Bioassays. *ACS Sens.* **2016**, *1*, 1336–1343.
(191) Kang, T.; Kim, Y. G.; Kim, D.; Hyeon, T. Inorganic Nanoparticles with Enzyme-Mimetic Activities for Biomedical Applications. *Coord. Chem. Rev.* **2020**, *403*, 1–21.
(192) Saleh, N. B.; Milliron, D. J.; Aich, N.; Katz, L. E.; Liljestrand, H. M.; Kirisits, M. J. Importance of Doping, Dopant Distribution, and Defects on Electronic Band Structure Alteration of Metal Oxide Nanoparticles: Implications for Reactive Oxygen Species. *Sci. Total Environ.* **2016**, *568*, 926–932.
(193) Wehmas, L. C.; Anders, C.; Chess, J.; Punnoose, A.; Pereira, C. B.; Greenwood, J. A.; Tanguay, R. L. Comparative Metal Oxide Nanoparticle Toxicity Using Embryonic Zebrafish. *Toxicol. Rep.* **2015**, *2*, 702–715.
(194) Deline, A. R.; Nason, J. A. Evaluation of Labeling Methods Used for Investigating the Environmental Behavior and Toxicity of Metal Oxide Nanoparticles. *Environ. Sci.: Nano* **2019**, *6*, 1043–1066.
(195) Bhattacharya, P.; Neogi, S. Antibacterial Properties of Doped Nanoparticles. *Rev. Chem. Eng.* **2019**, *35*, 861–876.
(196) Hansen, C. M. *Hansen Solubility Parameters: a User's Handbook, Second Edition*; Taylor & Francis: Boca Raton, FL, 2007.
(197) Galin, M. Gas-Liquid Chromatography Study of Poly(Ethylene Oxide)-Solvent Interactions: Estimation of Polymer Solubility Parameter. *Polymer* **1983**, *24*, 865–870.
(198) Medvedovski, E.; Alvarez, N.; Yankov, O.; Olsson, M. K. Advanced Indium-Tin Oxide Ceramics for Sputtering Targets. *Ceram. Int.* **2008**, *34*, 1173–1182.
(199) Jackson, G.; Chapman, W. G.; Gubbins, K. E. Phase Equilibria of Associating Fluids. *Mol. Phys.* **1988**, *65*, 1–31.
(200) Chapman, W. G.; Jackson, G.; Gubbins, K. E. Phase Equilibria of Associating Fluids. *Mol. Phys.* **1988**, *65*, 1057–1079.
(201) Santos, A.; de Haro, M. L.; Fiumara, G.; Saija, F. The Effective Colloid Interaction in the Asakura–Oosawa Model. Assessment of Non-Pairwise Terms From the Virial Expansion. *J. Chem. Phys.* **2015**, *142*, 224903.

(202) Yu, S.; Chow, G. M. Carboxyl Group (–CO_2H) Functionalized Ferrimagnetic Iron Oxide Nanoparticles for Potential Bio-Applications. *J. Mater. Chem.* **2004**, *14*, 2781–2786.
(203) Chang, Y.-C.; Chen, D.-H. Preparation and Adsorption Properties of Monodisperse Chitosan-Bound Fe_3O_4 Magnetic Nanoparticles for Removal of Cu(II) Ions. *J. Colloid Interface Sci.* **2005**, *283*, 446–451.
(204) Kim, S. Y.; Zukoski, C. F. Particle Restabilization in Silica/PEG/Ethanol Suspensions: How Strongly Do Polymers Need to Adsorb to Stabilize Against Aggregation? *Langmuir* **2011**, *27*, 5211–5221.
(205) Oh, C.; Do Ki, C.; Young Chang, J.; Oh, S.-G. Preparation of PEG-Grafted Silica Particles Using Emulsion Method. *Mater. Lett.* **2005**, *59*, 929–933.
(206) Carnahan, N. F.; Starling, K. E. Equation of State for Nonattracting Rigid Spheres. *J. Chem. Phys.* **1969**, *51*, 635–636.
(207) Boublík, T.; Vega, C.; Diaz Peña, M. Equation of State of Chain Molecules. *J. Chem. Phys.* **1990**, *93*, 730–736.